# Macroporous ion-exchange membrane adsorbers: correlation between membrane structure, separation conditions and performance in bioseparation

Makroporöse Ionenaustausch-Membranadsorber: Korrelation zwischen Membranstruktur, Trennbedingungen und Trennleistung in der Bioseparation

Dissertation

Zur Erlangung des akademischen Grades
Dr. rer. nat.
des Fachbereichs Chemie
der Universität Duisburg-Essen

vorgelegt von Dipl.-Ing. Jun Wang
aus Shandong

Essen 2009

Tag der mündlichen Prüfung: 15. September 2009

Vorsitzender: Prof. Dr. E. Hasselbrink
Referent: Prof. Dr. M. Ulbricht
Korreferent: Prof. Dr. T. Schmidt

# Abstract

In the first part of this dissertation, commercial Sartobind® porous cation exchanger membranes, based on stabilized regenerated cellulose and with sulfonic acid (S) or carboxylic acid groups (C), were analyzed with respect to their pore structure in dry, slightly swollen and wet state by three microscopic methods, conventional scanning electron microscopy (SEM), environmental SEM (ESEM), and confocal laser scanning microscopy (CLSM). The dehydration behaviour of the membranes was *in situ* observed at varied vapour pressure in the chamber of the ESEM, indicating some deformations of the macropore structure (largest pore diameters up to 20 μm) and significant changes in dimension and mobility of smaller cellulose fibers within these macropores, both as function of water content of the membrane. The binding of mono-Cy5-labelled lysozyme inside fluoresceine-labelled and unlabelled Sartobind® membranes was monitored by CLSM. The characteristic fluorescence intensity distributions in areas of $(146 * 146)\ \mu m^2$ indicated that protein binding takes place predominately in a layer which is anchored to a fine cellulose fiber network and, to a lower degree, directly to thick cellulose fibers. Due to the limited thickness of this binding layer, a significant fraction of the macropores remained free of protein. Protein binding as function of concentration and incubation times was also monitored by CLSM and discussed related to the binding isotherms for the membranes Sartobind® S and C. Further, a flow-through cell for the *in situ* monitoring with CLSM of protein binding during the binding step was built, and the results obtained for binding of lysozyme in membranes Sartobind® S indicate that this experiment can give very important information on the dynamic behavior of porous membrane adsorbers during separation: The lateral microscopic resolution in the x,y plane enables the identification of different breakthrough times as function of the location (pore structure), and this information can help to explain possible reasons for axial dispersion (in z-direction) observed in breakthrough analyses of the same separation in a chromatography system. The combination of advanced microscopy with detailed investigations of static and dynamic protein binding will provide a better understanding of the coupling between mass transfer and reversible binding in membrane adsorbers onto separation performance, and it will provide valuable guide-lines for the development of improved membrane adsorbers.

Based on the knowledge of the first part, new membrane adsorbers with carboxyl groups were prepared via UV-initiated heterogeneous grafting polymerization on Hydrosart® macroporous regenerated cellulose membranes. The dynamic performance was investigated in detail with respect to the pore size and pore size distribution of the base membranes, ion-exchange

capacity, target proteins and architecture of the functional layers. Main characterization methods were pore analysis (BET and permporometry), titration, analysis of protein binding under static conditions including visualization by CLSM and chromatographic analysis of dynamic protein binding and system dispersion. The trade-off between ion-exchange capacity, permeability and static binding capacity of the functional membrane has partially been overcome by adapted architecture of the grafted functional layer achieved by the introduction of suited uncharged groups and stabilization of binding layer by chemical cross-linking. These membranes have negligible effect of flow rate. There is no considerable size exclusion effect for large proteins due to mesh size of functional cross-linked layers. Investigation of system dispersion based on breakthrough curves confirms that the adapted grafted layer architecture has drastically reduced the contribution of the membrane to total system dispersion. The optimum pore structure of base membranes in combination with the best suited architecture of functional layers was identified in this study.

In the last part, the internal flow distribution of the flat sheet membrane modules was further quantified characterized based on a novel radial zone rate model. The proposed model partitioned the total void volume of the chromatography module into zones that have approximately homogeneous velocity profiles over time. The model was mathematically represented and analytically solved as a network of continuously stirred tank reactors (CSTR). An additional plug flow reactor (PFR) was connected in series with the CSTR network in order to account for a time-lag that was not associated with system dispersion. The capability of the model to describe experimental breakthrough data was compared to the often applied standard model for extra-membrane system dispersion which consists of a single CSTR in series with a PFR. The commercial CIM® module and a custom designed Sartorius cell were studied with acetone and lysozyme as test tracers at varied flow rates and for varied membrane pore sizes under non-binding conditions. In all studied cases the proposed model fits the measured breakthrough curves better than the standard model. Moreover, the minimal number of radial flow zones that were required to accurately describe the observed breakthrough curves and the estimated flow fractions through these zones provided valuable information for the analysis and optimization of internal module designs.

This work was performed during the period from May 2006 to May 2009 at the Institute of Technical Chemistry (Lehrstuhl für Technische Chemie II), Department of Chemistry, Universität Duisburg-Essen, under the supervision of Prof. Dr. Mathias Ulbricht.

I declare that this dissertation represents my own work, except where due acknowledgement is made.

_____

Jun Wang

# Acknowledgement

First I am deeply grateful to Prof. Dr. Mathias Ulbricht, who enables me to work at the group of Technische Chemie II, Uni Duisburg-Essen (UDE), and his constructive suggestions and active discussions during my work. Additionally, I would to express my respect for his respectable personality.

I am very thankful to Prof. Dr. Torsten Schmidt, who acted as referee for this thesis.

Dr. Rene Faber and Dr. Volkmar Thom from Sartorius Stedium Biotech GmbH, Göttingen have provided me the opportunity involved in this work, and given me their technical supports, active discussion during this work.

And I would like to express my gratitude to everyone involved in my work:

Dipl.-Biol. Florian Dismer and Prof. Dr. Jügen Hubbuch, Dr. Eric von Lieres from Institut für Biotechnologie of Jülich Research Center,

Dipl.-Chem. Diana Spettmann and Prof. Hans-Curt Flemming from Biofilm Center of UDE, Dipl.-Ing. Smail Boukercha, Ms. Suhyoun Yu, Ms. Yu Feng from UDE.

for their kindly co-operation work and technical support.

The skilled technical support for the manufacture of the flow-through membrane module by Frank Matthes of UDE, is also acknowledged. I am very sorry for his suddenly young dead.

MSc. Haofei Guo has kindly corrected some part of text of this work.

I am very happy with the nice work atmosphere in the group of Technische Chemie II of UDE during the research work, special thanks go to Dipl.-Ing.Chem. Inge Danielzik, Ms. Claudia Schenk, Ms. Roswitha Nordmann-Silberg, MSc. Haofei Guo, Dr. Dongming He, Dr. Heru Sussanto, Dr. Qian Yang.

Finally, I would like to thank all of my family - my parents, parents in law, and my daughter Tiantian, for their love and moral stimulation, especially, my husband Jionglu, who gives me the harbor of happiness.

*This thesis is dedicated*

*to my family*

*for their love and moral stimulation*

献给我的家人

感谢你们给与我的爱护和激励

The main parts of this thesis have been published (submitted) in the following publications:

1. von Lieres, E., Wang, J., Ulbricht, M. *Model based quantification of internal flow distributions from breakthrough curves of coin-shaped membrane chromatography modules*, Ind. Eng. Chem. Res., 2009, submitted.
2. Wang, J., Faber, R., Ulbricht, M. *Influence of pore structure and architecture of photo-grafted functional layers on separation performance of cellulose-based macroporous membrane adsorbers*, J. Chromatogr. A, 2009, under reversion.
3. Wang, J., Dismer, F., Hubbuch, J., Ulbricht, M. *Detailed analysis of membrane adsorber pore structure and protein binding by advanced microscopy,* J. Membr. Sci., 320 (2008) 456.

# Content

# 1. Introduction

With the increasing importance of biopharmaceutical therapeutics such as recombinant proteins, monoclonal antibodies, viral vaccines and plasmid DNA, bio-manufacturing industry has been boosted in the last years. The commercial manufacture requires a reliable process with high yield and high purity, and, most important, cost efficiency. Economic modeling of processes has shown that up to 80% of the overall costs are incurred during downstream purification process (*1*). Chromatography is widely employed at all operation stages of purification ranging from capture to polishing step. Conventional ion-exchange chromatographic steps are commonly based on resin bead packed columns (particles, typically having a diameter of $\geq$50 µm) with high resolution and high binding capacity. Generally those columns have low throughput and an oversized diameter is used to enable high volumetric rates in order to meet the requirement of process throughput. With the rapid improvements in upstream production, the traditional chromatographic platform has become the bottleneck in downstream process (*2-6*). The use of chromatographic membrane adsorbers has successfully overcome this problem in lab scale (*7*) and large scale (*2, 8, 9*).

Chromatographic membrane adsorbers are based on macroporous supports from established membrane formation process technology. Subsequent chemical modification (*6, 10-12*) is performed for the attachment of functional groups acting as binding sites throughout the membrane. They were introduced as stationary phase in liquid chromatography separations since 1990s (*13-16*). Diverse research of membrane adsorbers has been performed towards more suitable and efficient base membranes (*17-19*), improved surface chemistries (*20-25*), optimized flow distribution of membrane devices in lab (*26-28*) and production scale (*8, 29, 30*) as well as mass transport phenomena (*31-34*). Membrane adsorber has been reported as a technology potentially suited for large-scale application due to its ability to integrate capture and purification steps for processing large amounts of product in relatively short times (*35*). Ion-exchange membrane chromatography has become the most successful application type of this technique (*36-38*).

Membrane adsorbers combine the selectivity of chromatography resins with the high productivity of filtration membranes (*4, 9, 10, 36*). The key advantages of membrane adsorbers in comparison with conventional resin based porous adsorbers result from the pore structure of the membrane which allows a directional convective flow through the majority of the pores. The continuous character of membrane layer enables a simple scale-up and also

operation in a low range of trans-membrane pressure due to a relatively short effective thickness of the membrane layers. This membrane process allows high throughput with significant reduction in buffer consumption. Furthermore, the development of disposable membrane adsorber unit facilities the integration of these materials in bioprocesses, by saving cleaning and validation costs. They have been successfully applied for removing of trace impurities and potential contaminants in flow-through mode and for separation of sensitive bio-molecules such as blood factors, monoclonal antibodies, or technical enzymes where a rapid operation decreases the probability of their degradation (*7, 9, 30*). They are very useful for separation of large solutes such as DNA, RNA and viruses with molecular weight of over 250 kDa in bind-and-elute mode (*39-41*). In large-scale recombinant monoclonal antibody production, flow-through anion exchange chromatography has been implemented for removing of a variety of viruses, DNA and endotoxin in capture and polish steps (*42-44*). However, lower surface-to-bed volume ratios generated lower binding capacity of membrane adsorber and inefficient flow distributions of membrane modules remain a challenge for wide routine application in process-scale productions (*30, 45*).

Photo-initiated heterogeneous polymerization has been successfully applied as an easy and robust approach for the preparation of high capacity ion-exchange membrane adsorbers based on polypropylene and regenerated cellulose membranes (*20, 22, 46, 47*). Regenerated cellulose membrane is widely used in biotechnology due to its abundant availability, less binding capacity with protein and compatibility with biological systems. A systematic investigation of ion-exchange membrane adsorbers, prepared via photo-initiated heterogeneous polymerization, in terms of the correlations among properties of base membrane, functional layer via chemical functionalization as well as separation conditions (i.e. properties of liquid phase, flow rate, membrane module) should be prerequisite for better understanding of mass transfer and binding kinetic of membrane chromatography process.

# 2. Background

## 2.1. Principles of bioseparation

Bioseparation refers to the extraction and purification segment of a bioprocess. It is also termed as downstream purification process in fermentation technology (*48*). With the growing importance of biopharmaceutical therapeutics in treating human disease such as cancer, bioseparation is getting attractive in the manufacture of e.g. recombinant monoclonal antibodies, viral vaccines, and plasmid DNA (*9, 39*). Most important, it represents a major manufacturing cost for a wide variety of products.

In a typical process train for the manufacture of monoclonal antoibodies (*3*) illustrated in **Figure 2-1,** this usually involves a native or recombinant protein A capture step combined with a cation exchange column for intermediate purification and an anion exchange column operating in flow through mode to remove negatively charged impurities such as DNA, host cell protein, endotoxins, and endogenous virus**.**

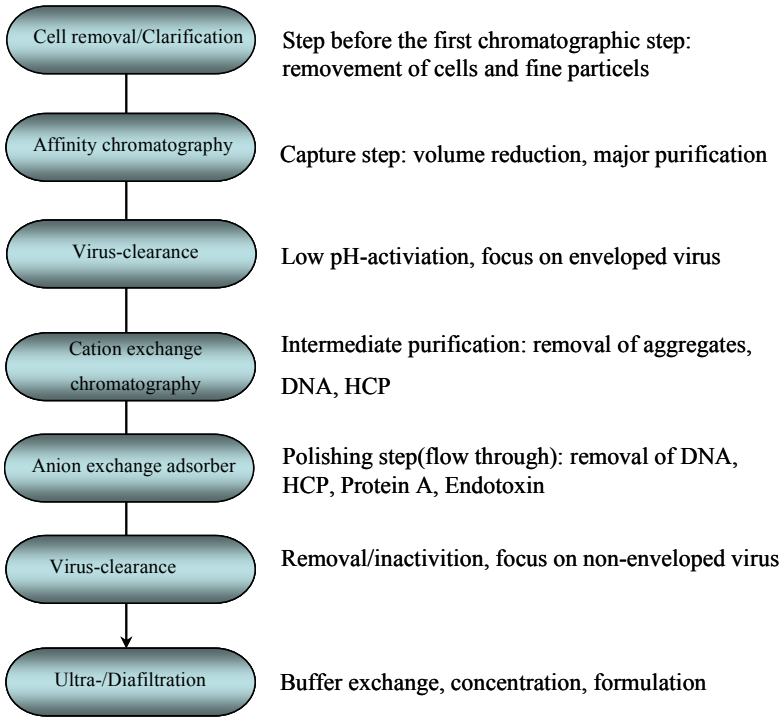


**Figure 2-1.** Typical process train for the manufacture of monoclonal antibodies

The biological activity of a protein is determined by its unique 3D-dimensional structure and surface functionality. Proteins are biopolymers formed by a linear sequence of the 20 natural occurring amino acids. The conformation is stabilized primarily by hydrophobic interactions due to the unfavourable free energy associated with solvation of non-polar groups in water. The net result is that the non-polar side chains tend to collapse together to form the hydrophobic core of protein. Hydrogen bonds between donor groups such a N-H and acceptor groups such as C=O with lone pair electrons stabilize the protein's secondary structure including α-helices and β-sheets. Positively charged amino groups and negatively charged carboxylic groups are typically located alone the protein exterior. The net protein charge is determined by the number and pKa of these acidic and basic amino acids. The isoelectric point (pI) is the pH value at which the protein has no net electrical charge, typically determined by the equilibrium position in an isoelectric focusing gel or the lack of motion in an applied electric field (*49*).

Bioseparation is largely based on chemical separation process. Some of the attributes of bioseparation distinguish it from chemical separation. For instance, biological products are commonly present in very low concentration in the being purified solution. The concentration of monoclonal antibodies is typically 0.1 mg/ml in the mammalian cell culture supernatants. Large volumes of dilute product streams have to be processed for gaining possible modest amounts of pure products. Hence a high throughput is required. Many impurities such as viruses, DNA and endotoxin and by-products exist in cell culture supernatant, and these impurities or by-products have similar chemical and physical properties to those of the target product. Biological products are thermolabile and susceptible to denaturation. Frequently, bioseparation is based on multi-technique separation based on one or more of the following factors (*50*):

- Molecular size using filtration, membrane separation, centrifugation, chromatography
- Density using centrifugation, sedimentation, flotation
- Diffusivity using centrifugation, filtration, sedimentation
- Polarity using extraction, chromatography, adsorption
- Solubility using extraction, precipitation, crystallization
- Electrostatic charge using adsorption, membrane separation, electrophoresis
- Volatility using distillation, membrane distillation, pervaporation

## 2.2. Modes of preparative chromatography

The binding of a dissolved protein to an immobilized ligand is due to one or several of the following interactions (*51*):

1. ion-ion or ion-dipole bonds
2. Hydrogen bonding
3. Hydrophobic interactions
4. Dispersion or van der Waals forces
5. Aromatic or $\Pi-\Pi$ interactions

Depending on the types of interactions involved, separation mechanism of chromatography can be classified into affinity chromatography, ion-exchange chromatography, hydrophobic interaction chromatography, reverse-phase chromatography, immobilized metal affinity chromatography and other types of chromatography such as size exclusion chromatography (*52, 53*).

- **Affinity chromatography (AFC)**

ACF takes advantage of biological interactions to effect binding of specific solutes. Antibodies, antigens, or dyes are conjugated to polymer resins or membranes for purpose of binding specific solutes from a mixture. In particular, it deals with bio-specific affinity chromatography. The high affinities of protein for specific metals are used. Diversities of affinity chromatography have been used in bioprocess. For instance, the most widely utilized Protein A affinity chromatography for large-scale antibody separation, or the dye ligand chromatography such as Cibacron blue, which is through to mimic the nucleotide binding sites of enzyme. Immunoaffinity chromatography utilizes the high specificity and strength with antibodies bind to their antigens. Biomimetic ligands mimic the interactions of biomolecules with their natural ligands. For the immobilized metal ion affinity chromatography, the binding is to residues that are distributed over the protein surface (*37, 51*).

- **Ion-exchange chromatography (IEC)**

IEC is one of the most often used modes of chromatography for protein separation. This is due to the high dynamic capacities, high resolution and low relative costs of the IEC materials, and simple buffer used in large scale protein purification process (*54*). Another advantage of this technique is that the elution takes place under mild conditions so that the proteins maintain their native configuration during the chromatographic processing.

Ion exchangers exploit surface charges on the protein under a given pH and salt ion concentration and interact with the protein predominately by electrostatic interactions (*55*). Elution is performed with increasing of salt concentration resulting in weakening of the ionic forces. Ion exchangers can be positively charged (strong, weak anion exchanger) or negatively charged (strong, weak cation exchanger) depending on the permanence of charge over a broad pH range. Commonly, strong exchanger can maintain their charge over a broader pH range than weak ion exchanger. A number of different functional groups are used. Most common are amines in the anion exchangers and the carboxylic acids in the cation exchangers. Strong anion exchangers have quaternary amines where strong cation exchangers have sulfonates (*51*).

- **Hydrophobic interaction chromatography (HIC) and reverse phase chromatography (RPC)**

HIC and RPC are separations based on the attraction between hydrophobic groups on the protein and a hydrophobic matrix. In reverse phase chromatography, the sample is applied in an aqueous buffer and eluted in an organic buffer. The retention of protein on a reversed phase chromatography matrix is dependent on the relative hydrophobicity of the protein compared to the polarity of the fluid and solid phase. Elution occurs when the relative hydrophobicity of the protein is decreased by either decreasing the polarity of the fluid phase or increasing the polarity of the protein through the addition of an ion-pairing agent.

In hydrophobic interaction chromatography the sample is applied under conditions of high salt concentration and eluted under conditions of low salt concentration. The mechanisms of partitioning of hydrophobic interaction chromatography can be explained in the same way as the interaction between non-polar solutes in water. Dissolving a non-polar substance in water is thermodynamically unfavorable. A non-polar solute forces the water to form a cavity in which the solute fits leading to a negative change in entropy. As the concentration of salts increases, the protein aggregate on the surface of adsorbents. HIC is sensible to used salt, pH,

buffer type and temperature.

- **Size exclusion chromatography (SEC)**

SEC is also called gel filtration. It separates solutes on the basis of their size. Molecules larger than the largest pores in the gel can not enter the gel and are eluted first. Smaller molecules enter the gel to varying extents, depending on their size and shape, and thus are retarded on their passage through the bed. In general, SEC resins (or matrixes) are hydrophilic polymer gels with a broad distribution of pore size. SEC is especially suitable for changing buffers, or for removing small molecules from protein solutions.

## 2.3. Membrane separation in bioprocesses

Membranes are used extensively throughout the production, purification, and formulation of biotechnology products. The membrane can remove large impurities and pass the product, or retain the product and pass solvent and salts. The greatest interests have been in the application of pressure-driven processes of ultrafiltration, microfiltration, and virus filtration (*36, 56*). Microfiltration membranes are capable for removing particles larger than 0.1 μm. Ultrafiltration membranes are used for concentrating and diafiltering soluble macromolecules that have a size in solution of less than 0.1 μm. Membrane adsorber has been used as a technology potentially suitable for large-scale applications due to its ability to integrate capture and purification steps for processing large amounts of products in relatively short time.

Current application of membrane adsorber is focusing on the aspects of two areas: flow-through application aimed at removing trace impurities, such as virus, bind-elute purification of extremely large molecules essentially excluded from the internal pore structure of commercially available bead-based resins such as large molecule bind-elute purification include viral vectors, plasmids as well as extremely large protein molecules (MW >250 kDa) (*40*). The flow velocity independency of membrane adsorber makes it ideally suitable for the purification of very large molecules such as plasmids or rotavirus like particles for gene therapy applications (*39-41, 57*).

Membrane adsorbers are commercially available in variety of chemistries ranging from standard strong and weak anion and cation exchangers to hydrophobic interaction, reverse phase and affinity chemistries (*4, 5*). Membrane adsorber devices are available as stacked flat sheet in flow through or radial flow type, pleated as well as hollow fibers devices (*4*).

Currently commercially available membrane adsorbers are Sartorius's Sartobind® family with a nominal pore size of 3 μm cellulosic membrane (*58*) and Pall's Mustang® family with a nominal pore size of 0.8 μm polyethersulfone membrane (*59*). Polymeric monoliths made by a different manufacturing technology but having similar pore morphology compete with macroporous membrane adsorber, especially for ultrafast high resolution separation (*60, 61*).

## 2.4. Binding and mass transport phenomena of membrane adsorbers

Chromatography is a solute fractionation technique which relies on the dynamic distribution of molecules to be separated between a stationary phase and a mobile phase. The stationary phase can be packed particles in column or (stacked flat sheet) membranes in device. The mobile phase is passed through the device, typically at a fixed velocity. A pulse of sample containing the molecules to be separated is injected into the device along with the mobile phase. The moving velocity of molecules through the device depends on their respective interactions with the stationary phase (*50*). A chromatogram is influenced by several factors, such as the fluid dynamics inside the packed bed, mass transfer phenomena, and most importantly, the equilibrium of the adsorption. The elution profile of an ideal chromatogram depends only on the thermodynamic behavior of the chromatographic system. Real chromatograms take into account the additional kinetic of mass transfer and flow distribution.

### 2.4.1. Equilibrium thermodynamics

The adsorption equilibrium is determined by the isotherm, which gives the correlation between the loading of the solutes on the adsorbent at different fluid phase concentration. Langmuir adsorption isotherm is the most common type of isotherm used in preparative chromatography. It describes quantitatively the build up of a layer of molecules on an adsorbent surface as a function of the concentration of the solute in the liquid in which it is in contact. For Langmuir isotherm, it is assumed that for a homogeneous surface, solute is bound in single layer and there are no lateral interferences between the adsorbed molecules. Assuming that the membrane has a fixed number of adsorption sites, *S*, to which the sample protein molecules, *P*, can bind reversibly in a monolayer pattern

$$P + S \underset{\text{kd}}{\overset{\text{ka}}{\Leftrightarrow}} PS \tag{2-1}$$

Where PS represents protein-adsorbent. Equation (2-1) is associated to a reversible second-order rate expression that can be written as:

$$\frac{\partial q}{\partial t} = k_a * c * (q_{\max} - q) - k_d * q \qquad (2\text{-}2)$$

at equilibrium, equation (2-2) reduces to Langmuir isotherm for single component:

$$q = \frac{q_{\max} * K * c}{1 + K * c} \qquad (2\text{-}3)$$

with $K = \frac{k_d}{k_a}$ Langmuir constant

Where $k_a$ and $k_d$ are respective association and dissociation rate constant. $q$ is adsorbed amount on the membrane, $c$ *is* protein concentration in bulk solution and $q_{max}$ maximal binding capacity of membrane.

In the simplest case the adsorption isotherm is of the Langmuir type with a steep slope at the initial part and reaching a saturation value at higher amounts of adsorbed solute. The slope of the isotherm corresponds to the distribution (equilibrium) coefficient K, discriminating two parts of the isotherm: the linear and nonlinear parts. In the linear range K is equal to the Henry constant. **Figure 2-2** Indicates the relationship of two different components and the related selectivity, which is devoted by Henry coefficient of the respective component in diluted solution. The j-component has higher affinity than i-component. For the nonlinear part K becomes smaller and reaches a limiting value at high solute concentrations. The subsequent part of the isotherm is called the overload regime whereas the linear part corresponds to the non-overloaded regime. Good resolution in the nonlinear range of the adsorption isotherm has to be achieved in terms of loading. In the preparative chromatography, column is operated under the overload conditions to achieve a high productivity, however purity of the product is thus limited. In addition, pressure drop should be as low as possible to allow operation at maximum linear velocity (*62*).

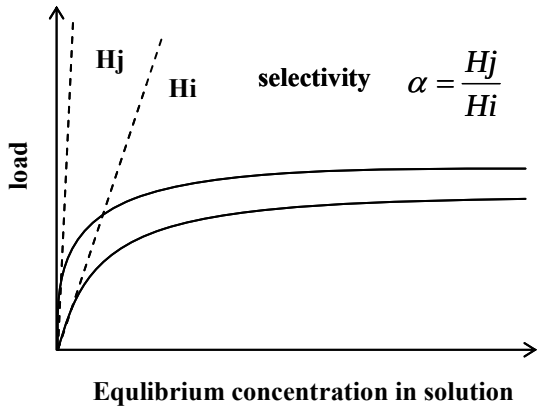


**Figure 2-2.** Related selectivity of two different components is presented by Henry coefficient.

### 2.4.2. Principles of mass transport, fluid dynamics

In conventional chromatography systems, transport of the solute from the bulk liquid phase towards the boundary layer of particle by convection is the first step of the separation process. The second step is diffusive transport of the solute through the film layer which is called film diffusion. The transport of the solute to the binding sites in pore system of adsorbent particle proceeds by pore diffusion or surface diffusion. Once a solute molecule reaches a free adsorption site on the functional layer, actual adsorption takes place. External mass transfer and kinetic of adsorption are normally very fast in the fluid phase. The rate limiting processes are the film diffusion and transport inside the pore system. For particle diameter larger than 5 μm, transport resistance in the pore is the dominant contribution to the total mass transfer resistance for most preparative chromatography (*63*).

In every chromatographic system, the effects of fluid non idealities such as mixing, channeling and dead volumes, a term that comprises the membrane void volume, the volume of flow distributors, of the detector flow cell and of the pump head, should be considered since their occurrence results in broadening of the residence time distribution of the solute. This is particularly encountered in the case of small scale membrane modules in which the volume of stacked membranes is far smaller than the total volume of circuit, pump and detector (*64*). The rest of the band broadening results from mass transfer resistance (*62*). The main factors that influence axial dispersion are extra column effects, i.e. system hold-up

volume or devoted as dead volume involving connection tubes, detector, etc. All those have strong influence of breakthrough curves. The most critical points for axial distribution in column chromatography are the fluid distribution at the inlet and fluid collection at the outlet. This effect will be enhanced with increasing column diameter. Besides, packing non-idealities also strong contributes to the particle resin packed column. All hydrodynamic effects that contribute to the total band broadening are summarized in the term axial dispersion.

A chromatographic column can be assumed to be made up of a large number of theoretical plates which are analogous to those in a distillation column. The greater the number of these plates in a column, the better is the separation. The dependence of linear flow rate is often described using the well known van Deemter equation:

$$HETP = A + B/u + C*u \tag{2-4}$$

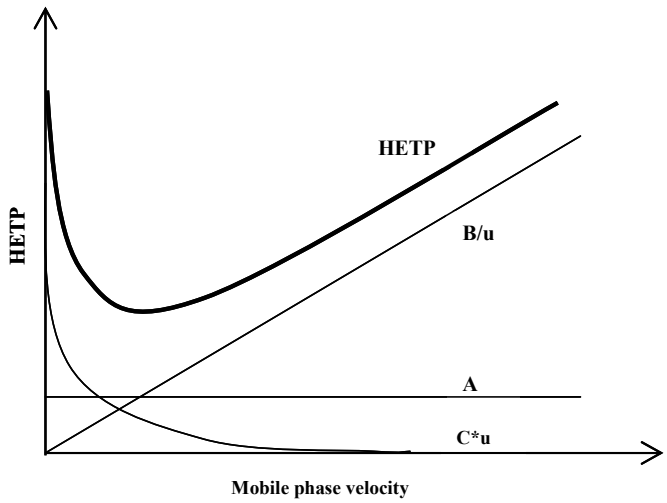


**Figure 2-3.** Relationship between HETP and flow rate.

**Figure 2-3** represents the von Deemter equation. It shows the dependence of plate height of column on the mobile phase velocity. It is widely used to characterize band broadening in a chromatography column. A, B, and C are constants that describe different physical contributions to peak-broadening. The A term is mainly governed by eddy-diffusion depending the nature of column packing, particularly the particle diameter and size distribution. The linear increase of the plate height at high velocities is summarized in the second term. The second term describes the diffusion in axial direction, and decreases with an increasing of internal flow rates. The hyperbolic third term includes contributions from the

binding kinetics (adsorption/desorption) as well as mass transfer between mobile phase and stationary phase. It dominates at high flow velocities (*62, 65*).

## 2.5. Advantages and limitations of membrane adsorbers

In conventional chromatography systems (**Figure 2-4**), solute should first diffuse into porous bead to access available the binding sites, but contaminants in bioprocess are normally large molecules as virus, or DNA with hydrodynamic diameter of 20~300 nm. The limited diffusion in mass transport and concomitant higher resistant leads to long residence time, and even generates blocking of pores. The separation process is controlled by the rate of pore diffusion. Moreover, good packing quality and low band-broadening due to axial dispersion and mass transfer resistance are necessary to obtain suitable system efficiency. Consequently, optimization of chromatographic process often involves a compromise between efficiency and column pressure drop.

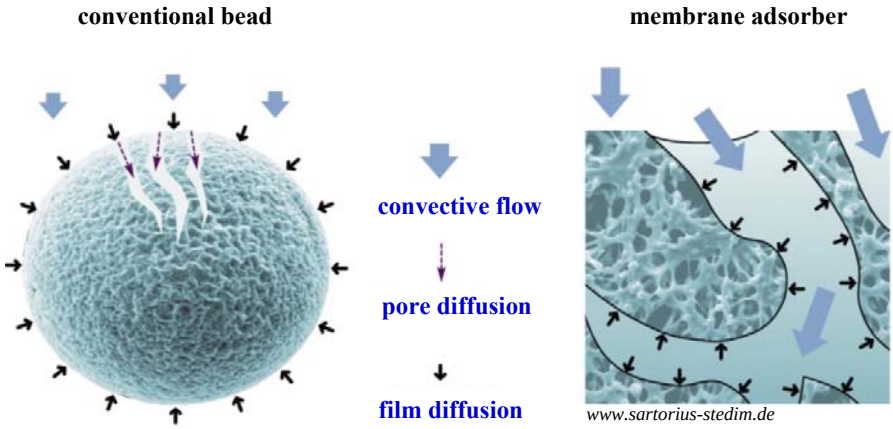


**Figure 2-4.** Mass transport phenomena during adsorption of molecules for chromatography process.

Chromatographic membrane adsorbers are based on macroporous supports from established membrane formation process technology and subsequent chemical modification for the attachment of functional groups acting as binding sites throughout membrane. A membrane stack has no extra void volume (as in a packed bed of resin), and the pore structure of the membrane allows a convective flow through the majority of the pores with high through-put, thus, the characteristic distances (i.e. times) for pore diffusion will be drastically reduced. The

mass transport of solute to binding sites occurs thus mainly by convectional flow, film diffusion (film transport through the boundary layer to the porous pore wall, and for diffusion into the pores which are not accessible by convection) (*4, 10, 45*). For membrane adsorbers with three-dimensional polymer layers ("tentacles" or "brushes") grafted to the internal pore structure, the overall mass transfer coefficient for adsorbing solute is also influenced by diffusion to the binding sites in this layer. This effect may become significant when the binding is fast and the thickness of this layer is relatively large, e.g. several hundreds nanometers, as it is the case for previously analyzed porous membrane adsorbers, e.g. membranes with photo-grafted polyacrylate layers (*20, 46*). Mass transfer rates of membrane adsorber media may be an order of magnitude greater than that of standard resin-based chromatography media, allowing for high efficiency and high flux separations (*35*). Properly designed membrane adsorbers have chromatographic efficiencies that are 10 to 100x better than stationary resin column (*56*). The breakthrough capacities of ion-exchange membranes operated at low loads are often comparable to those of commonly used resins (*9, 18, 30, 66*). Similar values of resolution have also been achieved (*18, 33*).

The convective flow dominated membrane adsorber has lower pressure drop and permits high flowrate and thus high productivity with significant reduction in buffer consumption. It is already integral to many bioprocess as other membrane processes because they are easy to scale-up/down, more important, they can be used as disposable modules and they save on cleaning and validation costs (*3, 30*). Nevertheless, for wide routine application in process-scale productions, membrane adsorber has some limitations that need to overcome. The major limitations are: (1) non-identical membrane pore size distribution, (2) uneven membrane thickness, (3) distorted inlet flow distribution and poor collection at the outlet, (4) low binding capacity (*45, 67*).

Commonly, the pores in membrane present mono-modal or bi-modal distribution. For the case with a wide pore size distribution, the flow of feed will preferentially take place through large pores, where the transport resistance is smaller and thus very little target solute can be carried through the smaller pores. The resulted accessibility to binding sites leads to low utilization of binding capacity of membrane adsorber and large dispersion effect. The similar problem is with the uneven membrane thickness. Most available commercial membranes present uniform thickness. Flow of feed is encouraged where the thickness is smaller due to the lower transmembrane pressure drop. These effects can be minimized by use of membrane with narrow pore size distribution and membrane stack of sheet membranes.

Membrane modules hold membrane stacks in place, and distribute, collect the flow at the inlet and outlet. The inlet of conventional membrane module for flat sheet membranes is generally in the form of a circular channel entering a larger circular cross-section. The feed flow is usually distributed radically over the entire leading membrane surface using a suitable distributor. The feed flow should ideally hit all points of the membrane simultaneously (**Figure 2-5a**). Although the traditional filter configuration was fine for polishing applications, the flow distribution and hold-up volumes were not properly designed to make membrane adsorbers competitive in the bind-elute purification. Conventional flat sheet membrane devices usually have far greater radial compared to axial dimension for lower transmembrane pressure. The inlet is in the form of a small circular cross-section with tapering as shown in **Figure 2-5b**. Ghosh and Wong (*28*) have discussed the vital role of flow distribution and collection within membrane modules in membrane chromatography process. They experimentally compared the conventional membrane module with tapering at the inlet and outlet as distributor (**Figure 2-5b**) and newly designed module with cut distribution channels within modules (**Figure 2-5c**). The new design of membrane module improved the utilization in the peripheral region of membrane. The binding capacity enhancements with the design as shown in **Figure 2-5c** were in the range of 110~112% in the breakthrough mode and around 135% in the pulse chromatographic mode.

The low binding capacity as consequence of low surface-to-bed volume ratio and poor flow distribution of membrane module limit the application in binding-elute mode, where target of interest is bound while impurities are eluted. However, in flow-through mode, where buffer condition is set to enable binding of impurities while allowing product to flow through, the adsorptive binding capacity is not anymore limitation, particularly when it is used as polishing step for antibody purification to remove impurities having less than 1% concentration. Many works have been implemented for improvement of binding capacity of membrane adsorber. A comparison of membrane adsorbers via photo-grafting polymerization with other membrane systems will be given in **Table 6-1.** of **Section 6.2.5.**.

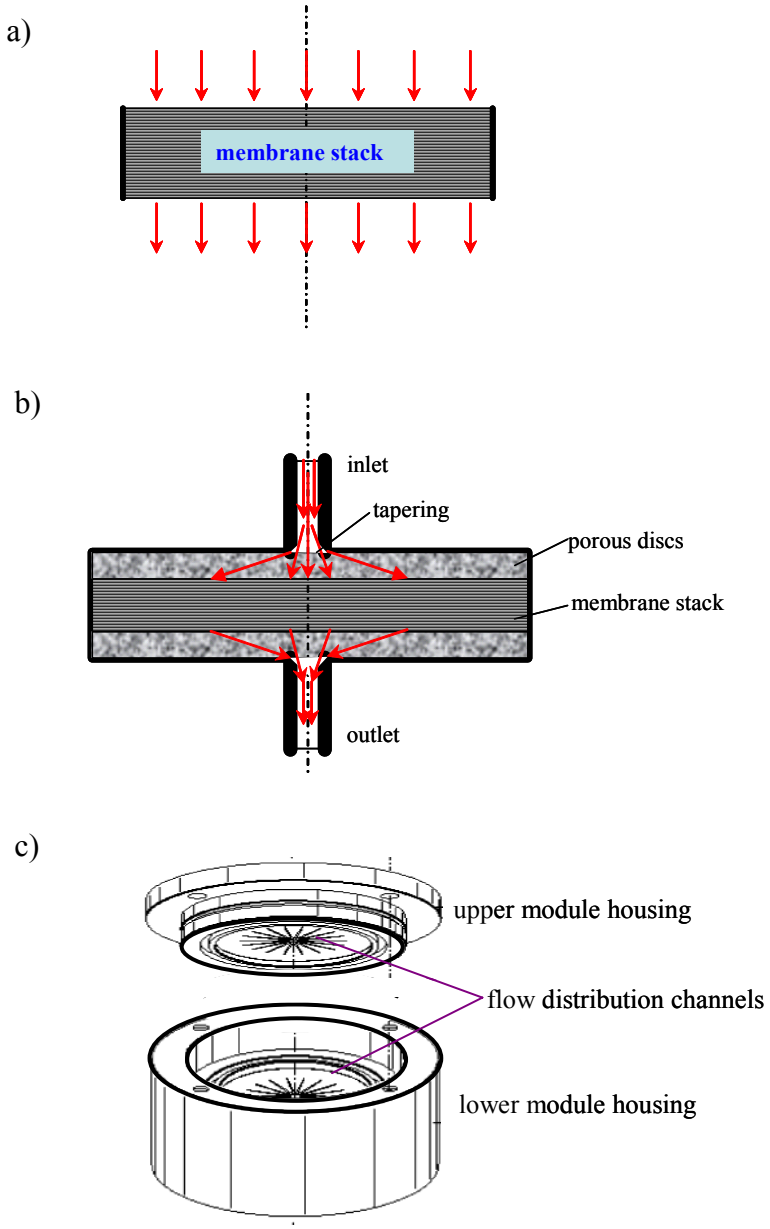


*Ghosh and Wong, J. Membr. Sci. 281(2006)532*

**Figure 2-5.** a) Efficient flow distribution; b) conventional membrane module with tapering; c) membrane module with flow distribution channels.

## 2.6. Surface grafting techniques for polymeric membranes

Basically, polymer surface modification can be performed by using chemical and physical processes. Physical processes take advantage of e.g., surface segregation, or radiation of electromagnetic waves, while chemical modifications uses wet–treatment, blending, coating or metallization. A membrane surface modification is aimed either to minimize undesired secondary interactions such as adsorption or adhesion, which results to membrane fouling, and thus reduce their performance or to introduce additional affinity, responsive interactions for improving the selectivity or creating an entirely novel separation function. Depending on pore structure and separation function either on the outer or the entire surface, improvement of membrane performance via membrane surface modification leads to effective solutions for problems or to novel principles. Controlling "primary" interactions for separation can be used to tailor the separation function of a membrane or to 'integrate' them with other processes (*10*).

In the chemical modification, the chemistry of polymeric membrane surface is modified either by direct chemical reaction or by the covalent bonding of suitable macromolecular chains onto the membrane surface (grafting) with physical activation. Heterogeneous reactions of the membrane polymer can be performed either by derivatization of or grafting onto the membrane polymer via reaction of intrinsic functional groups without polymer chain scission or change in bulk morphology (*6, 12*), or controlled degradation of the membrane material for the activation of derivatization or grafting reactions at minimized polymer chain scission or change of bulk morphology (*68*). The former reactions have been used extensively for the surface fuctionalization of membranes (*12*).

In order to achieve the ultimate aim of a membrane surface modification, the most used approaches for chemical modification are "grafting–to" and "grafting–from" reaction methods have been proposed. "Grafting–to" reaction is performed by coupling polymer molecules to surface (*10*). Introducing macromolecular functional layers to the surface of membranes could be done for MF or UF membrane with hydrophilic macromolecules (*69*). During "grafting–from" reaction, monomers are polymerized using an initiation at the surface (*70, 71*). "Grafting-to" method can well control the structure of polymer, however, with limited grafting densities on the surface. In contrast, the synthesis of surface-anchored polymers via "grafting-from" can obtain a very variation of grafting densities and chain lengths under relatively convenient reaction conditions (*10*). The following section will focus on the "Photo -Grafting-from" method, i.e., heterogeneous graft copolymerization.

### 2.6.1. Photo-grafting functionalization on polymeric membranes via heterogeneous graft copolymerization for membrane adsorbers

To meet the requirements in bioseparation processes, membrane adsorbers should present the respective properties, such as macroporous structure to enable unhindered interaction of large biomolecules or bionanoparticles with the binding sites, adapted amount and density of binding sites (in either 2D-layer on the pore surface or 3D-layer extending into the pore space), hydrophilic or neutral surface to prevent non-specific interactions with the membrane material itself as well as chemical stability to withstand harsh conditions during separation and regeneration, and, when application, they are allowed to be sterilized by autoclaving. Physically they should be stable to withstand trans-membrane pressure. Meanwhile, low material and manufacturing cost are also very essential to facilitate applications in large-scale industrial applications. The most relevant commercial membrane adsorbers are indeed based on macroporous supports from established membrane formation process technology and subsequent chemical modification for the attachment of functional groups acting as binding sites. Chemical modification (*72, 73*) and radiation-induced grafting method (*11, 23, 24, 74, 75*) are the most popular strategies for functionalization of membrane adsorbers.

In the "grafting–from" method, physical activation is usually needed to create free radicals (*70*). Heterogeneous radial graft copolymerization of functional monomers on membrane polymers can be initiated (formation of starter radicals) via:

(a) Degradation of the membrane polymer (main chain scission or cleavage of side groups), via physical excitation with radiation or plasma (**Figure 2-6a)**. It is possible to functionalize UV–sensitive membrane polymers, such as PES, also under 'simultaneous' conditions, i.e. in direct contact with the monomer.

(b) Decomposition of an initiator in solution and radial transfer (here hydrogen abstraction); radicals in solution may initiate a homopolymerization as a side reaction or leading to grafting via radial recombination (**Figure 2-6b)**.

(c) Adsorption of a type II photoiniator (e.g. benzophenone derivate) on the surface and selective UV excitation (the reactivity of the benzopinakol radiacal is too low to start a polymerization in solution)-surface-selective "grafting-from" (**Figure 2-6c)**.

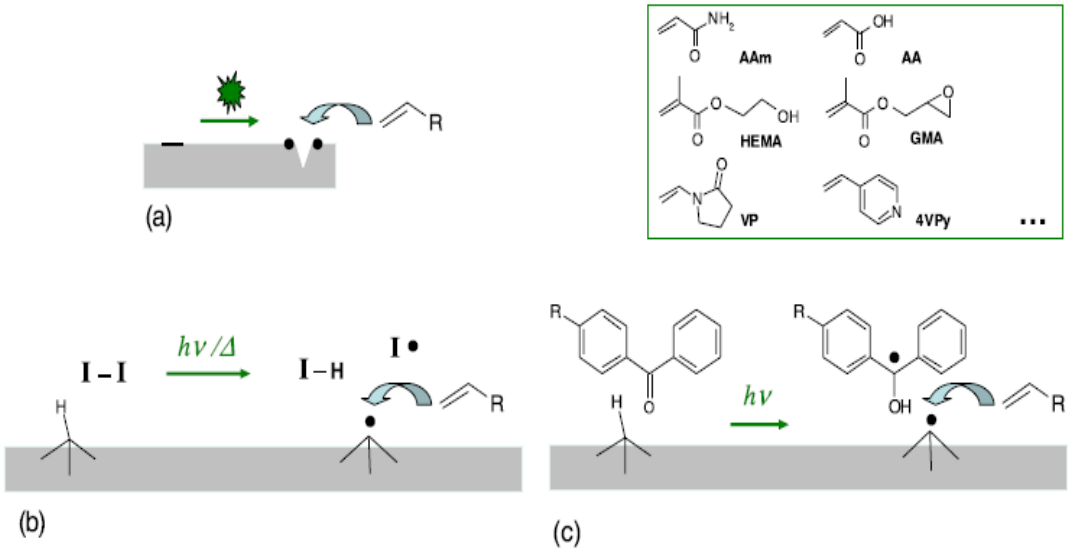


**Figure 2-6.** Heterogeneous radial graft copolymerization of functional monomers on membrane polymers can be initiated (formation of starter radicals) via: (a) degration of the membrane polymer via physical excitation with radiation or plasma; (b) decomposition of an initiator in solution and radial transfer (here hydrogen abstraction); (c) adsorption of a type II photoiniator on the surface and selective UV excitation surface-selective "grafting-from" (*10*).

The use of UV–assisted methods for a heterogeneous graft copolymerization, mainly with the intention to improve the 'decoupling' effects of the activation and the grafting reactions had been developed by Ulbricht *et al*. (*23, 68, 76, 77*). Additional photoinitiators, which can be selectively excited by certain UV energies, were used. An especially easy and effective two–step coating approach is based on (i) the adsorption of a 'type II' photoinitiator (e.g., benzophenone, BP) on the membrane surface and (ii) the subsequent UV initiated hydrogen abstraction reaction to yield polymer radicals on the surface of the membrane in the presence of monomer (*23, 78*) (cf. **Figure 2-6c**). Recently, new approaches to improve the surface selectivity by confining the initiator had been demonstrated by entrapped method (*23*), and synergist method (*79, 80*). The photoinitiator BP had been 'entrapped' in the surface layer of polypropylene (PP) by using a solvent, which can swell the PP in the coating step. By selecting suited BP concentration and time the uptake in the surface layer of the PP can be adjusted, and after change to a more polar solvent such as water or alcohol a fraction of the BP is immobilized but can still initiate a graft copolymerization (*23, 46*). Synergist immobilization photo-graft polymerization method had been developed for polymerization in

polar organic solutions for 0.2 µm commercial hydrophilized PP membranes. Tertiary amino groups as synergist (co-initiator) of BP were immobilized on the whole membrane surface. Grafting density and polymer chain length can be well controlled by adjusting the main functionalization parameters such as synergist surface concentration, BP concentration, UV irradiation time and monomer concentration (*20, 79, 80*).

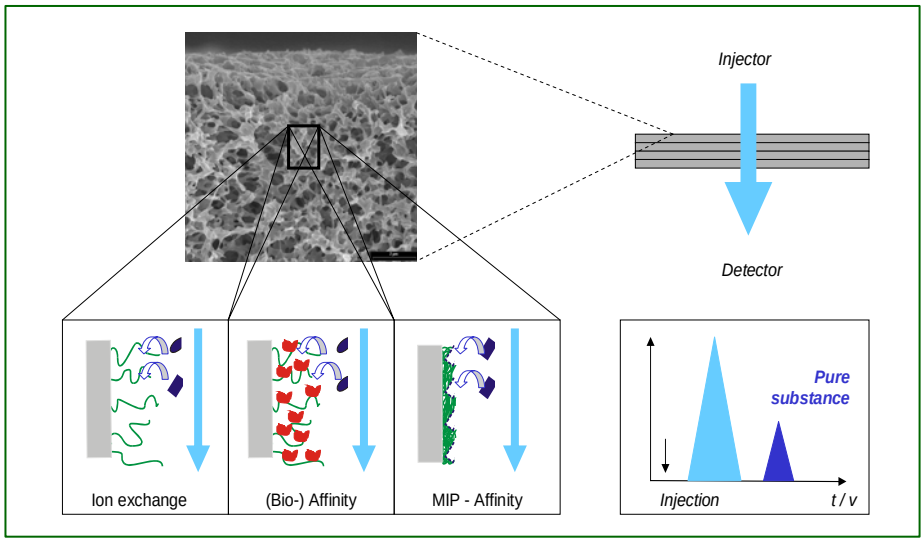


**Figure 2-7.** Different types of membrane adsorbers- the affinity and dynamic binding binding capacity for certain substances can be „tailored“by surface functionalization of a suited porous base membrane (*10*).

In general, there are three main composite membrane types, which could meet various demands in different fields: thin-film-, pore surface-functionalized and pore-filled membranes (*10*). Most composite membranes prepared via “photo-grafting-from” are pore surface-functionalized. Depending on initial pore size (micro/meso pores vs. macropores), grafted layer thickness and its distribution over the membrane cross-section (outer surface vs. entire internal surface) largely different membrane functionalities can be achieved. **Figure 2-7** illustrates an overview on different surface functionalization with 3D ion-exchange groups (*23*), immobilized bimolecular for affinity binding (*81*), and thin-layer MIP (*82, 83*) . All the types are obtained by selective photo initiation based on an even surface coverage of the entire pore surface of stable macroporous membranes. The design of membrane adsorber can be implemented by systematic and rational variation of components (such as base membrane, monomers), compositions (monomer, solvents, ec.) and conditions (photoinitiator, UV times,

etc.). And such developing work must be supported by detailed characterization of the properties of the membrane adsorber, investigation of the correlation between membrane structure, separation conditions and separation performance of proteins in bioprocess.

## 2.7. Characterization methods for membrane adsorbers

Membranes are typically described by their pore size or nominal molecular weight cut-off (MWCO), with the latter typically defined as the molecular weight of a solute that has retention coefficient of 90%. However, the key characteristics in the design of a membrane adsorber are really the selectivity, volumetric flux (permeability), and the system capacity (*36, 65*).

The intrinsic selectivity of the membrane adsorber is determined by the chemistry of membrane surface, i.e. the thermodynamic binding isotherm. The volumetric filtrate flux is related to the membrane hydraulic permeability in terms of trans-membrane pressure drop, especially at high flow rates. The filtrate flux evaluated using the actual feedstock of interest is typically smaller than the value predicted form the clean membrane due to membrane fouling and concentration polarization. This is less relevant for membrane adsorber. The system capacity is defined as the volume of feed that can be processed per unit of membrane area (volume).

As illustrated in **Figure 2-8,** the separation performance of membrane adsorber process, in terms of dynamic binding capacity, is influenced by the interplay of matrix pore structure (e.g. pore size, pore size distribution), architecture of the functional layer for reversible binding and mobile phase properties (e.g. structure of binding site, thickness and density of the 3D-functional layers as well as their mesh size), as well as properties of target solutes (e.g. PI value and molecule weight) and flow rate of mobile phase (*4, 10*). And most important, the used membrane module, or pressure drop at high flow rates could dramatically limit the dynamic binding capacity. In combination with advanced microscopy methods and other methods such as chromatography, nitrogen adsorption technique, the membrane structure (pore size and pore size distribution, porosity and specific surface area, buffer permeability, etc.) can be characterized. Mathematic based modelling has been also adopted for quantitative characterization of membrane chromatographic system (cf. **Section 2.8.).**

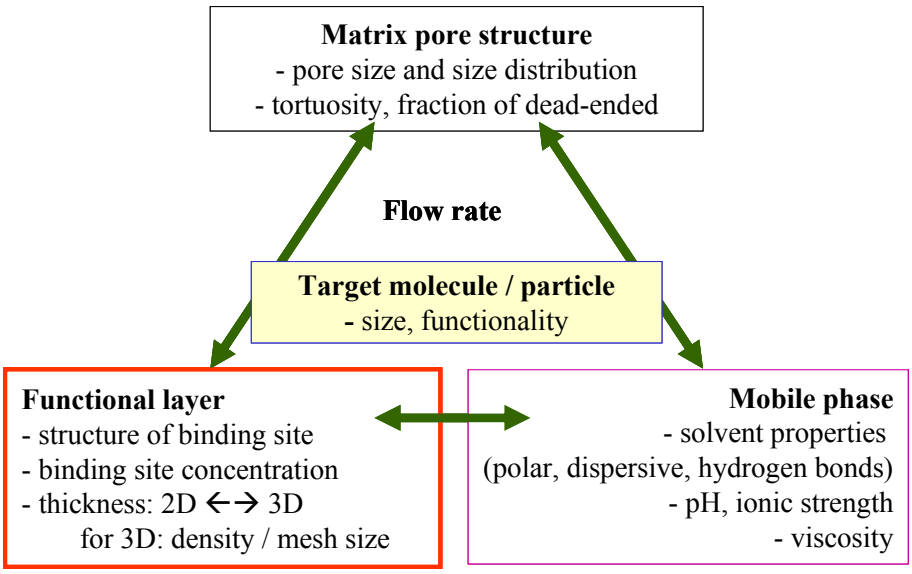


**Figure 2-8.** Performance of membrane adsorber in terms of the correlation among matrix pore structure, architecture of functional layer and properties of mobile phase.

- Advanced microscopy methods

Advanced microscopy methods have been widely applied for the investigation of membrane structure and related transport phenomena. Light microscopy and fluorescence microscopy have been employed for investigation of protein adsorption (*84, 85*). Scanning electronic microscopy (SEM) was used to visualize membrane morphology under dry state. The environmental scanning electron microscope (ESEM) is a direct descendant of the conventional SEM. In addition to conventional images in high vacuum, ESEM allows high-resolution microscopy at higher pressures or even investigation of wet and insulating samples without prior specimen preparation. This technique provides the opportunity to examine the nature and distribution of water in heterogeneous system in both static and dynamic experiments (*86*). ESEM has been used to study the swelling behaviour of cellulose fibres *in situ* (*87*) and the wetting properties of macroporous polymer membrane (*88*). By controlling sample temperature and the pressure of water vapour surrounding it, the water content of the sample can be adjusted *in situ* (*89*).

Confocal laser scanning microscopy (CLSM) has been used long in medical research and microbiology for the identification of structures within cells and other tissues (*90*). It provides

the possibility of measuring the fluorescence emission of tracer fluorophores within 3-D objects with high local resolution and depth discrimination. This technique is now powerful analytical tool (*91-94*) and had also been proposed for the characterization of adsorbent particles (*95, 96*) or porous membrane adsorbers in static state (*97-99*). The use of two different fluorescence dyes for labelled membrane and protein which can be detected independently enables simultaneous visualization of membrane pore structure and protein binding to the membrane functional layer by CLSM. Charcosset *et al*. (*97*) investigated the membrane morphology by using of CLSM in reflect mode. Reichert *et al*. (*98*) first visualized the protein binding performance of Sartobind® ion-exchange membrane adsorber. Wickramasinghe et. al. (*99*) illustrated the different binding patterns of thyroglobulin, BSA and lysozyme.

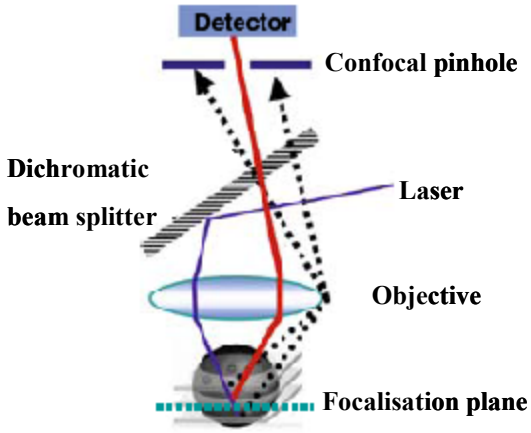


**Figure 2-9.** Schematic drawing of CLSM (*100*)

CLSM is based on the excitation of fluorescent molecules by an appropriate laser beam. This beam is focused at a certain scanning depth. The image of the source pinhole is focused through the objective lens into the specimen (**Figure 2-9**). The light which is backscattered or reflected by microstructures which lie above or below the exact focalisation plane is weakly transmitted through the detector pinhole. The detected signal comes mainly from the exact focalisation plane. The incident light can be moved over the specimen in a rectangular raster pattern. The sample can thus be scanned at different depths without destroying of sample (*90*). However, diverse influence parameters such as fluorescent labelling technique, its sensitivity on experimental parameters and the change of protein characteristics upon binding, disturb the analyse result using this technique. The review from Hubbuch and Kula (*100*) elucidates the

related problems for resin based adsorbent in details. The comparison of the above advanced microscopy techniques and their limitation will be discussed in **Section 6.1.3.**

- Other methods for characterization of matrix structure

The characteristic structure parameters of membrane adsorber mainly involve pore size and pore size distribution, internal specific area, as well as buffer permeability of membrane. Diverse methods have been adopted for determination of pore size and pores size distribution, for instance, by using of capillary flow porometry, also called as extrusion flow porometry, the throat diameter of pores and their pore size distribution can be measured through displacement of a wetting liquid from pores (*20*). It is especially suitable for isotropic membrane such as PET membrane (*68, 101*). Mercury intrusion porosimetry works through intrusion of a non-wetting liquid into pores. It has the drawback that the high pressure needed to intrude the mercury may either distort the skeletal porous structure of the sample, especially when compressible materials such as cellulose or binders/latex are present, or lead to a reduction in the measured number of large pores due to the shielding by smaller pores (*102, 103*).

Size-exclusion chromatography has been used for determination of pore dimensions of chromatography media (*104*). Inverse size-exclusion chromatography has been adopted for characterization of cation-exchange adsorbents (*105*) and polymer packing materials (*106*). The pore structure of a strong anion-exchange membrane adsorber has been investigated using inverse size-exclusion chromatography under different buffer and salt concentration conditions (*38*). Beside, gel filtration is applied for the quantitative characterization of solutes and solute interactions for UF (*107*). Some work has tried to use batch size-exclusion to characterize the pore size distribution, use liquid impregnation method to determine the total specific volume of pores of macroporous membrane adsorber (*38*). Besides, NMR and NMR-based cryoporometry have been used for characterization of such as porous solid, imbibition saturated structure (*102, 103*). DSC-based thermoporosimetry is a relatively new candidate in this field to yield both pore size distribution and pore volume, especially for pigmented coatings (*103*).

The specific surface area of porous material can be determined by using of nitrogen adsorption technique, the BET method (*108*). However, a minimum sample mass is required corresponding to the respective specific area. For conventional macropous membrane (pore

size ≥ 2 µm), which has normally low specific area, a great amount of material is required for more detailed determination.

Buffer permeability $J_p$ of membrane is hydraulic measured using solution with different ionic strength or pH values, and evaluated after Hagen-Poiseuille's law (equation 2-5). It is resulted from dividing the flux by the trans-membrane pressure and the used membrane area, and the pore size of the membranes (*65*).

$$J_p = \frac{V}{\Delta t * \Delta p * A} = \frac{k * r^2}{\eta * L_c} \qquad (2\text{-}5)$$

Where V is the volume of the permeate relating to a single cylindrical membrane pore, $\Delta t$ the required time, $\Delta P$ trans-membrane pressure, A the effective surface area, r pore radius, $k_0$ specific form factor, $\eta$ viscosity of the fluid, $L_c$ characteristic capillary length (i.e. the membrane thickness).

This equation is valid assuming a cylindrical geometry of the membrane pores and equal sizes of all of the pores. The thickness of the grafted layer on the pore wall can be calculated, assuming an even functionalization, as the difference between the pore radius of the unmodified and the pore radius of the functionalized membrane (*68*).

- Capacity of functional groups and protein binding capacity

The separation of substances is based on their reversible binding on the functional layers on membrane pore walls. The structural properties and separation conditions of membrane adsorber determine the mass transfer rates to the binding sites and their accessibility for target substances. Typical characterization methods for membrane adsorber are focussed on their functionality, i.e. the binding performance for various target solutes or nanoparticles, especially under flow-through conditions to optimize process productivity (*109*). This includes the total capacity of functional groups of the membrane (total ion-exchange capacity) and the available binding capacity for target solutes under static and dynamic conditions (static and dynamic binding capacity).

The total ion-exchange capacity of weak cation exchange membranes can be determined via a static indirect titration (*23, 110, 111*) or by frontal analysis and elemental analysis (*110, 112*). The accessible functional binding capacity can be *in situ* determined under flow-through

conditions via the inadvertent pH transient method (*46, 112, 113*).

The static binding capacity of membrane adsorber is determined through mass balance after batch incubation or converted from the elution values of protein by UV spectro-photometry at 280 nm. The protein binding isotherm can be measured in the same way and subsequent curve fitting for evaluation of parameters. A more exact determination of parameters can be implemented by process simulation (e.g. chromatogram) (*41, 114*). The dynamic capacity of membrane adsorbers is defined by the appearance of an unacceptable level of a key component in the flow-through stream, referred as breakthrough. Breakthrough is determined by both the equilibrium binding properties of the adsorbents (resin or membrane) in combination with any mass transfer limitation in the device (*36*). From the breakthrough curve (BTC) one can also retrieve information about the dynamics of solute binding in the adsorber as function of mass transfer and binding kinetics. System dispersion curve (SDC), measured with an inert tracer, represents the behavior of system non-ideality caused by back-mixing or channeling as well as effects of the volume of different components. This is especially important when the volume of the adsorber (the membrane stack used in this work) is smaller than the volume of the capillaries, flow distributors etc. in the system. From the complete BTC additional information about the maximum DBC ("max.DBC") and DBC value at 10% breakthrough (10% DBC) can be regained. For industry application, 10% DBC is more favorable because the feed is usually applied only until the concentration of the target solute in the flow-through reached up to 10% of its initial concentration. While the static binding capacity is dependent on the membrane structure, target molecule and buffer conditions, the dynamic value could be additional affected by the flow rates induced pressure drop and the design of membrane module. All those correlations will be detailed elucidated in **Section 5.2.**

## 2.8. Insights into the mathematical modeling of membrane adsorbers

In the chemical process, detailed mathematic modeling has been state-of-the-art for scale-up, process analysis and optimization of operation units in terms of mass transfer, heat transfer and mass transfer kinetics. In contrast, purification strategies of complex bioparticles are as yet rather empirical due to their complicates (*41*).

Mathematical models of chromatographic processes usually consist of the equation of mass conservation and transport for the individual components. It should consider all significant transport phenomena (**Section 2.4.)** occurring in the chromatographic column. Depending on

process conditions and the nature of the involved solutes, one or more of the following effects will dominate process performance:

- Adsorption isotherm
- Axial dispersion
- Mass transfer resistances that determines the rate at which equilibrium is established
- Diffusion (film diffusion, pore diffusion)

The general approach used to model membrane chromatography separation is derived from frontal analysis of chromatographic column. It is a combination of the continuity equation coupled with a kinetic equation that describes the protein adsorption mechanism, and different models have been developed. Briefs and Kula has developed mathematical models of membrane adsorption for a flat membrane system. They specified the continuity equation for a single cylindrical pore and extended the solution for the whole membrane stack (*33*). Roper *et al*. set up a model with two separate stirred tanks and plug flow regions before and behind the membrane stack. They successfully analyze pulse experiments by moment analysis on the basis of an analytical solution which is however only valid for non-binding conditions (*34*). A more general approach has been developed by Etzel and co-workers by incorporating nonlinear sorption isotherms and mass transfer coefficients based on either the overall or local solid-phase or liquid-phase driving forces, and extended their model to multicomponets (*16, 31, 32, 115*). Their simulated curves did broaden as membranes approached saturation. Those conventional models for system dispersion and dynamic adsorption will be elucidated in **Sections 2.8.1.** and **2.8.3.**

It must be mentioned that all such models use only average parameters (such as binding constant, binding capacity per membrane volume, flow rate and pore diameter) for the porous membrane with their functional pore surface. In these approaches, dead volumes in membrane chromatography systems are traditionally modeled by one plug flow reactor (PFR) and one continuous stirred tank reactor (CSTR) in series (*31, 32*), or by lumping the overall peak broadening and tailing effects into a volume of a mixing cell (*41*). However, this setup could systematically not explain specific features of our measured chromatograms with different porous membrane adsorbers (*20, 25, 46*). Similar findings are also reported in the literatures (*116, 117*). Von Lieres *et al*. developed a novel radial multi-zone flow model for stacked membrane chromatography (**cf. Section 2.8.2.**). This model accounts for inhomogeneous radial flow distribution. Several zones with different residence times can be formed in the

distributors of the chromatography module and cause inhomogeneous loading of the membrane stack over time. It can be used for quantification of system dispersion generated by membrane modules (*118*). Combining with continuity equation and different kinetic mechanisms (**cf. Section 2.8.3.**), it can be also implemented for various zone geometries and different kinetic and isotherm models for adsorption and desorption in the membrane stack (*119*).

### 2.8.1. Conventional dispersion model

System dispersion can be presented by the breakthrough curve of a non-binding solute. It characterizes the dispersion flow behavior of the system independently of the binding mechanism between binding ligand and solute. System dispersion can be accurately described by a combination of CSTR and PFR illustrated in **Figure 2-10**. The CSTR takes into account the effect of flow mixing and non-idealities, while the PFR considers the effects of time shifts and dead volumes (*115*). The overall system volume can be expressed as the sum of them:

$$V_{sys} = V_{CSTR} + V_{PFR} \tag{2-6}$$

The CSTR dynamics is given by

$$\frac{dc_{out}^{CSTR}}{dt} = \frac{Q}{V_{CSTR}}(c_{in}^{CSTR} - c_{out}^{CSTR}) \tag{2-9}$$

where

$c_{in}^{CSTR}$, $c_{out}^{CSTR}$ denote the respective inlet and outlet concentrations, and Q denotes volumetric flow rate.

The initial condition is:

$c_{out}^{CSTR} = 0$, at t=0

The response of the breakthrough curve was used as the influence concentration for CSTR model (*120*). Comparison of experimental and simulated dispersion curves for different systems by Etzel and co-workers shows good agreement (*121*, *122*).

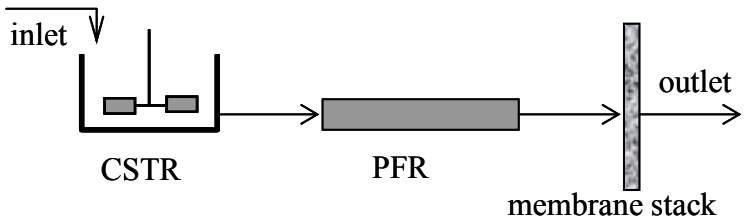


**Figure 2-10.** Conventional system dispersion model represents as a combination of CSTR and PFR.

### 2.8.2. Radial multi-zone flow model for system dispersion[1]

***Physical modeling***: Non-binding conditions were chosen for analyzing properties of the chromatography module. Moreover, dispersion in the membrane stack is neglected. The latter is justified because the void volume of the pores in the membrane stack is much smaller than the total void volume of the system. The flow time through the membrane is also includes time-lags in the feed line and in the detector line.

Previous experimental studies by us (*20, 46*) and other groups (*26, 28*) strongly indicate that flow is not uniquely distributed over the radius of membrane chromatography modules, as schematically illustrated by **Figure 2-11a**. The path length clearly increases from streamline $v_1$ to streamline $v_3$, and the same is true for the passed system volume. The average residence time of solute molecules in the system does hence depend on their transport path. Molecules that flow through outer regions of the module are stronger retained than molecules that flow through the center of the module.

[1] This section is based on the paper by von Lieres, E., Wang, J., and Ulbricht, M., Model based quantification of internal flow distributions from breakthrough curves of coin-shaped membrane chromatography modules, Ind. Eng. Chem. Res., 2009, submitted.

a)

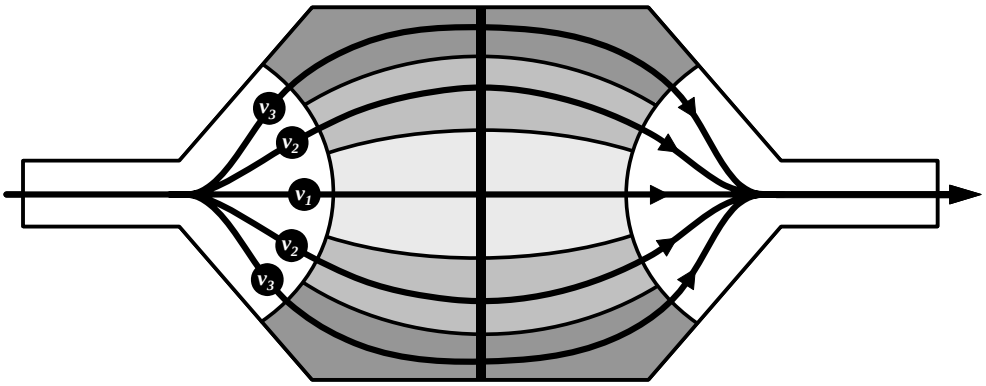


b)

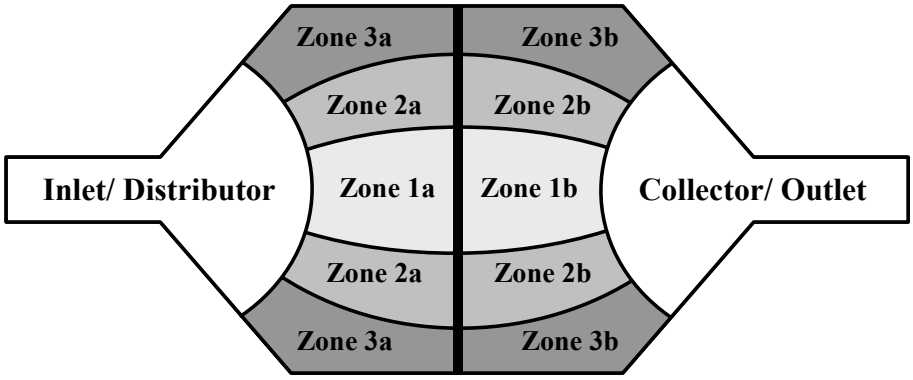


**Figure 2-11.** a) Typical flow paths through radial zones within flat sheet membrane stack modules; b) Geometric representation of the proposed model with three radial zones.

The model partitions the module into zones with different residence times. **Figure 2-11b** illustrates the basic principle for three radial zones. The feed line is pooled with the inlet and parts of the distributor that retain all solute molecules equally. An analogous zone is defined at the outlet. The remaining void volume of the module is axially divided by the membrane stack. The axial division might or might not be symmetric, but radial symmetry is always assumed (see **Figure 2-11b**). The radial zone boundaries are less sharply defined. The module is however fully characterized by the number of radial zones and by the fractions of volumetric flow through these zones as will be explained in the next section.

The physical model is equivalent to a network of continuously stirred tank reactors (CSTR) as shown in **Figure 2-12a**. An additional plug flow reactor (PFR) is connected in series with the CSTR network in order to account for time lags that are not associated with system dispersion.

The residence times increase from $\tau_{1a}$ to $\tau_{na}$ and also from $\tau_{1b}$ to $\tau_{nb}$ where $n$ denotes the number of radial zones. In axially symmetric modules the residence times $\tau_{ia}$ and $\tau_{ib}$ are pairwise equal for $1 \le i \le n$ . The volumetric flow fractions $f_i = v_i / v$ with $v = \sum_{i=1}^{n} v_i$ determine how many solute molecules are transported through the individual zones. **Figure 2-12b** shows the special case of the proposed model with one zone ( $n = 1$ ) and **Figure 2-10** the traditional model with one CSTR in series with a PFR. The latter will be used for comparing results and referred to by $n = 0$ in the following.

a)

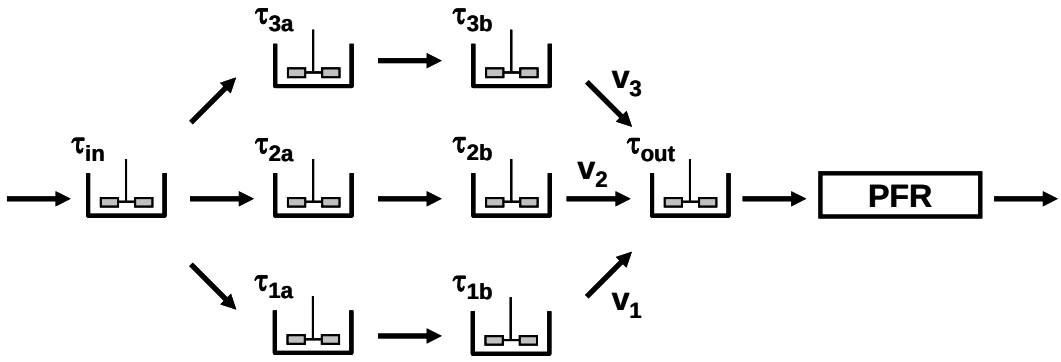


b)

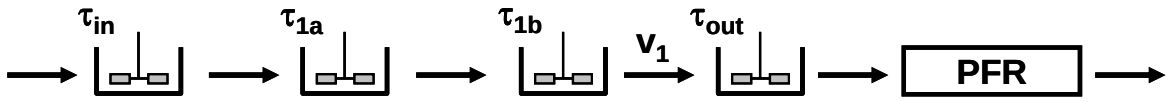


**Figure 2-12.** CSTR network representation of the radial zone model. a) general case with more than two zones; b) special case with one zone. A PFR is always connected in series with the CSTR network.

***Mathematical modeling***: The CSTR network model is now translated into mathematical equations. Each tank with one inflow is described by an instance of rate equation 2-8, where $c(t)$ denotes the concentration in the tank, $c_{in}(t)$ the concentration at the inlet, and $\tau$ the average residence time of solute molecules. The number of outflows is not relevant.

$$\frac{\partial c}{\partial t} = \frac{c_{in} - c}{\tau} \tag{2-8}$$

The tank that represents the collector has as many inflows as radial zones are present in the model and is described by rate equation (2-9).

$$\frac{\partial c}{\partial t} = \sum_{i=1}^{n} \frac{c_{in,i}}{\tau_i} - \frac{c}{\tau} \quad \text{with} \quad \frac{1}{\tau} = \sum_{i=1}^{n} \frac{1}{\tau_i} \tag{2-9}$$

Here $\tau$ denotes the total residence time of the tank in which the flows join. The fraction of volumetric flow through zone $i$ with $1 \le i \le n$ is given by $f_i = v_i / v = \tau / \tau_i$.

The model equations are all linear and allow a mathematical matrix representation of the CSTR network (equation 2-10), $m$ denotes the number of tanks):

$$\frac{\partial \mathbf{c}}{\partial t} = \mathbf{A} \cdot \mathbf{c} + \mathbf{b} \cdot c_{in} \quad \text{with} \quad \mathbf{c} = \left(c_1, ..., c_m\right)^T \tag{2-10}$$

The Jacobian matrix **A** and the inhomogeneity vector **b** define the topology of the CSTR network. Equation (2-11) gives an example with three radial zones.

$$\mathbf{A} = \begin{pmatrix} -\tau_{in}^{-1} & \cdot & \cdot & \cdot & \cdot & \cdot & \cdot & \cdot \\ \tau_{1a}^{-1} & -\tau_{1a}^{-1} & \cdot & \cdot & \cdot & \cdot & \cdot & \cdot \\ \cdot & \tau_{1b}^{-1} & -\tau_{1b}^{-1} & \cdot & \cdot & \cdot & \cdot & \cdot \\ \tau_{2a}^{-1} & \cdot & \cdot & -\tau_{2a}^{-1} & \cdot & \cdot & \cdot & \cdot \\ \cdot & \cdot & \cdot & \tau_{2b}^{-1} & -\tau_{2b}^{-1} & \cdot & \cdot & \cdot \\ \tau_{3a}^{-1} & \cdot & \cdot & \cdot & \cdot & -\tau_{3a}^{-1} & \cdot & \cdot \\ \cdot & \cdot & \cdot & \cdot & \cdot & \tau_{3b}^{-1} & -\tau_{3b}^{-1} & \cdot \\ \cdot & \cdot & f_1 \cdot \tau_{out}^{-1} & \cdot & f_2 \cdot \tau_{out}^{-1} & \cdot & f_3 \cdot \tau_{out}^{-1} & -\tau_{out}^{-1} \end{pmatrix} \quad \text{and} \quad \mathbf{b} = \begin{pmatrix} \tau_{in}^{-1} \\ \cdot \\ \cdot \\ \cdot \\ \cdot \\ \cdot \\ \cdot \\ \cdot \end{pmatrix} \tag{2-11}$$

The linear system has an analytical solution (equation 2-12) which can be easily computed, for instance, using the matrix exponential function *expm* in MATLAB.

$$\mathbf{c}(t) = \mathbf{A}^{-1} \cdot \left(e^{\mathbf{A} \cdot (t - t_0)} - I\right) \cdot \mathbf{b} \cdot c_{in} \tag{2-12}$$

Here $t_0$ denotes the time-lag of the entire system which is in the physical model described by a PFR in series with the CSTR network. More precisely several plug-flow regions are present in the feed and detector lines and in the membrane stack. However these regions can be lumped into one since the time-lags are additive.

***Parameter estimation*:** The total time-lag $t_0$, the residence times $\boldsymbol{\tau} = \left(\tau_1, ..., \tau_m\right)$ and the volumetric flow fractions $\mathbf{f} = \left(f_1, ..., f_{n-1}\right)$ are $n + m$ unknown model parameters. The fraction $f_n$ is determined from $\sum_{i=1}^{n} f_i = 1$. Geometrical symmetry assumptions can reduce the

number of residence times in the model. The unknown parameters are estimated from breakthrough concentrations $\overline{c}$ that are measured at $k$ points in time. The measurement times $t_j$ with $1 \le j \le k$ are usually but not necessarily equally distributed. The simulated detector concentrations are given by $c_m\left(t_j\right)$ and compared with the corresponding measured values $\overline{c}\left(t_j\right)$. The sum of squares of these deviations is taken as residual $r_{LS}\left(t_0, \boldsymbol{\tau}, \mathbf{f}\right)$ for parameter estimation (equation 2-13).

$$r_{LS}\left(t_0, \boldsymbol{\tau}, \mathbf{f}\right) = \sum_{j=1}^{m}\left(c_m\left(t_j\right) - \overline{c}\left(t_j\right)\right)^2 \tag{2-13}$$

The inlet concentration $c_{in}\left(t\right)$ can be set to one if the measurement data are correspondingly scaled. The MATLAB implementation *lsqnonlin* of the Levenberg-Marquardt algorithm is used for minimizing the residual. The whole parameter optimization takes few seconds for each breakthrough curve. Fitting qualities of the traditional model ($n = 0$) and of the radial zone model ($n \ge 1$), zones are compared by the least squares residual $r_{LS}$ and additionally by the maximum absolute deviation $r_{\max}$ which is scaled to percent of the maximal measurement value (equation 2-14).

$$r_{\max}\left(t_0, \boldsymbol{\tau}, \mathbf{f}\right) = \frac{100}{\max\limits_{1 \le j \le m}\left|c_m\left(t_j\right)\right|} \cdot \max_{1 \le j \le m}\left|c_m\left(t_j\right) - \overline{c}\left(t_j\right)\right| \tag{2-14}$$

Note, however, that the best fit is always calculated in the sense of least squares but only evaluated by means of the maximal absolute deviation because the latter is more strongly affected by individual experimental outliers. One of the most interesting characteristics of the studied system is the minimal number of zones that are required in order to achieve a satisfactory match between model simulations and measurement data. The flow distribution in a chromatography module is quantitatively characterized by the parameters of the least complex radial zone model that sufficiently well describes the data, whereas models with more zones than required are subject to over-fitting and prone to yield physically unrealistic results.

### 2.8.3. Modeling dynamic adsorption

The assumptions of cylindrical membrane pores, of uniform radial concentrations profile and uniform velocity profile are used in the modelling of chromatographic process in order to schematise the problem with a mass balance equation coupled with a kinetic equation that describes the protein-ligand interactions.

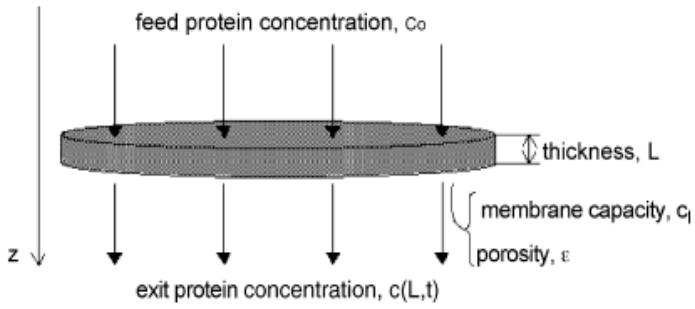


**Figure 2-13.** Schematic drawing of a membrane for modelling (*31*).

In the more general, Protein mass balance equation was written over the membrane stack as illustrated in **Figure 2-13** (*31, 35, 123*):

$$\varepsilon\frac{\partial c}{\partial t}+\varepsilon\nu\frac{\partial c}{\partial z}=\varepsilon D\frac{\partial^2 c}{\partial z^2}+(1-\varepsilon)\frac{\partial q_s}{\partial t} \qquad (2\text{-}15)$$

where $c$ is protein concentration, $c_s$ concentration of binding sites, $D$ diffusion coefficient, $\nu$ flow velocity, $\varepsilon$ membrane porosity. In the absence of pore diffusion as in membrane chromatography, the diffusion term can be substituted by introducing a term for axial dispersion.

Different kinetic expression for adsorption mechanisms have been reported in literatures. Very often Langmuir isotherm (equation 2-3) was explored for the modeling of chromatography process (*31, 33, 124*). The Langmuir, steric hinderance, and spreading model were evaluated by Yang and Etzel (*125*) in a mathematical model of protein purification using ion-exchange membranes. Their results showed that the steric hindrance model gives a substantial improvement with respect to the Langmuir model. However, only with the spreading model they had obtained a point by point fit of the experimental data even at later stages of breakthrough. More recently, these models have been further developed and applied to porous affinity membrane adsorbers by introduction of a bi-isotherm model in order to

account for specific and unspecific binding to an affinity membrane and also achieve good agreement between model simulations and measurement data (*116, 126*). However, there are still some controversial issues about this model.

Steric mass-action model (SMA) takes the effect of bound ions into account, describes adsorption in ion-exchange systems as a stoichmetric exchange reaction of each solute with a certain number of adsorbed counterions. At higher protein concentrations, the finite capacity of the stationary phase and steric shielding of stationary phase sites by the adsorbed molecules play important roles in equilibrium adsorption (*127*). Van Reis and co-workers used SMA model to guide process development and optimization in anion exchange bead column. Their results indicated that this model was able to accurately predict experimental results under high loadings with minimal parameter estimation (*128*). Vicento *et al.* implemented SMC model for the prediction of elution profile of anion exchange Sartobind D membrane adsorber during the purification of rotavirus like particles. Experimental data fitting gave good model validation (*41*). Frerick at al. had used a generic process model for the simulation of various downstream processes for purification of the mixing of BSA and IgG, based on SMA model and mass transfer resistance at the boundary layer as described by Sarfert and Etzel (*32*). The simulation results show that the replacement of an anion-exchange chromatography column by an anion-exchange membrane adsorber leads to a significant reduction in overall process time at constant yield and purity (*129*).

The usual initial conditions indicate that the beginning of the process, the membrane is free of adsorbed protein:

$c$ =0, at z ≥ 0, t=0 (2-16)

$q$ =0, at z ≥ 0, t=0 (2-17)

Dankwerts' boundary conditions for frontal analysis were used to include axial diffusion at the inlet of the membrane and the mixing at the exit of the membrane.

$$\varepsilon v c - \varepsilon D \frac{\partial c}{\partial z} = \varepsilon v c_0 \text{, at z=0, t>0} \quad (2\text{-}18)$$

$$\frac{\partial c}{\partial z} = 0 \text{, at z=L, t>0} \quad (2\text{-}19)$$

# 3. Problems and objectives

Typical specific surface areas of base macroporous membranes are only moderate. This is typically compensated by three-dimensional ligand layers grafted to the internal pore structure via chemical functionalization. For instance, conventional Sartobind® ion-exchange membrane adsorber is formed by cross-linked cellulose support and a hydrogel layer on its pore surface. In a real membrane adsorber, the pore structure can be quite heterogeneous (including pore shape and size distribution, tortuosity and dead-ended pores), binding can occur in relatively thick functional hydrogel layers extending into the pore space, and this structure may be dynamic due to swelling/shrinking of the base-material and/or the functional layer under separation conditions, or deformation by mobile phase flow. Many works have been done for characterization of different properties for membrane adsorbers, commonly via either microscopic method under static condition (*98, 99*) or dynamic chromatographic method (*9*). A microscopic study about the dynamic (protein binding) performance of membranes adsorber in microscale, especially under real operation conditions, has not been done yet.

The separation performance in membrane adsorber process is influenced by the interplay of matrix pore structure, architecture of the functional layer for reversible binding and separation conditions such as mobile phase and target solutes properties. Moreover, the critical role of the design of membrane module on the performance of chromatographic membrane separation has been recognized and experimentally investigated (*26, 28, 34*). Quantitative characterization of membrane modules such as flow distribution, fluid paths, void volumes, etc. under non-binding condition should be a prerequisite for further developing of mathematic modeling in chromatographic membrane process. Conventional flat sheet membrane devices usually have far greater radial compared to axial dimension. These high aspect ratios cause problems with inadequate flow distributions within modules leading to a drastic decrease in the utilization of binding capacity. This problem is also encountered with small scale fleet sheet modules, in which the flow is commonly distributed by using porous discs at both ends, but perfectly uniform radial flow distribution is usually not achieved. This can cause early breakthrough and strong tailing at the same time. In many studies attempts have been made to quantitatively model different chromatographic processes using traditional PFR-CSTR approach (*31-33*), however, these models could systematically not explain specific features of the measured chromatograms with different porous membrane adsorbers

(*20, 46, 116*).

The development of high-performance membrane adsorbers should proceed via an independent optimization of pore structure and architecture of functional layers providing useful binding site density with optimum accessibility (*10*). A more detailed microscopic characterization of the pore structure and solute binding including the related dynamics under near real operation conditions could provide valuable information for a better understanding of membrane adsorber performance and its further optimization. On the other hand, it is also very important issue to understand the correlation between pore structure of membrane and separation performance in terms of mass transport and binding kinetics.

**Objectives**

Based on the above issues, analytical tools and quantitative approaches to characterize the performance of membrane adsorber have been developed. Following objectives have been implemented in this dissertation:

In the first part of this dissertation, pore structure including morphology and dynamics in pore structure, as well as protein binding of commercial Sartobind® cation exchanger membranes were investigated by using conventional SEM and ESEM as well as CLSM. Further, the static binding patterns of protein in the membranes after various incubation conditions were investigated. As model protein, Cy5-labelled lysozyme was separated from unlabelled native protein to eliminate artefacts of non-specific interactions and ensure that all proteins are visible under the CLSM (*94, 130*). *In situ* monitoring with CLSM of protein binding in the membranes was done with help of a special flow cell. In combination with the static and dynamic protein binding data, this work provides a better understanding of the coupling between mass transfer and reversible binding in membrane adsorbers onto separation performance.

Based on the knowledge of protein binding patterns obtained via CLSM visualization for commercial Sartobind® membranes, novel weak cation-exchange membrane adsorbers were prepared in the second part using UV-initiated heterogeneous grafting polymerization method (cf. (*23*)). The base membranes were stabilized cellulose Hydrosart® membranes having average pore size of 0.45 µm, 1~2 µm and 3~5 µm. The polymeric binding site structure on the entire membrane pore surface had been achieved by using of acrylic acid (AA) as functional monomer. The layer architecture was varied by co-grafting of the “cross-linker” monomer methylene bisacrylamide (MBAA) and the “diluent” monomer acrylamide (AAm).

The dynamic performance was investigated in detail with respect to the pore size and pore size distribution of the base membranes, ion-exchange capacity, architecture of the functional layers and target proteins. Main characterization methods were pore analysis (BET and permporometry), back titration and *in situ* pH transient, analysis of protein binding under static conditions including visualization by confocal laser scanning microscopy and chromatographic analysis of dynamic protein binding and system dispersion. The influences of matrix pore structure and of architecture of functional layers were elucidated with respect to improvement of utilization in binding capacity for different target proteins under dynamic conditions, reduction of axial dispersion and the effect of flow rate. At last, an optimum pore structure of base membranes with suitable architecture of functional layers was suggested for high performance membrane adsorber. In parallel, the separation performance of the new membranes was compared by using of two small scale membrane modules with different internal structure design. The critical influence of membrane design in chromatographic bioseparation was elucidated.

In the last part of the dissertation, in cooperation with Dr. von Lieres from Research center Jülich, the flow distribution within small scale membrane modules with different internal structure was quantified by using of a novel radial multi-zone flow model (*118*). Two small scale flat sheet membrane modules, commercial CIM® module and a custom designed Sartorius cell, were characterized with acetone and lysozyme as test tracers at varied flow rates and for varied membrane pore sizes under non-binding conditions. This model divides the total void volume of the chromatography module into zones that have approximately homogeneous velocity profiles over time. The capability of the model to describe experimental breakthrough data was compared to the often applied standard model for extra-membrane system dispersion. The flow distribution, fluid paths, and void volumes within the membrane module were analyzed in terms of the influences of membrane pore sizes, flow rates as well as test tracers.

# 4. Experiments

## 4.1. Materials

For the characterization of commercial membrane adsorber in **Section 5.1.**, the used membrane adsorbers were flat sheet Sartobind ion-exchange membranes made from regenerated cellulose (kindly provided by Sartorius Stedim Biotech, Göttingen, Germany), a strong cation-exchanger (Sartobind S; batch #2229) with sulfonic acid groups and a weak cation-exchanger (Sartobind C; batch #2231) with carboxylic acid groups as well as unmodified Hydrosart membrane. The rated pore size of all membranes was 3~5 μm. Hydrosart are unmodified regenerated cellulose membrane. It is base membrane for Sartobind. The membranes were washed with Milli-Q water (from a system of Millipak®-40; Millipore) and buffer before the characterizations.

For preparation of novel membrane adsorber in **Section 5.2.**, Hydrosart flat sheet membranes with nominal pore size of 0.45, 1~2 and 3~5 μm (kindly provided by Sartorius-Stedim Biotech, Göttingen, Germany) were used. Membrane thickness was in the range of 200 to 250 μm. For the calculation of binding capacity per membrane unit, average thickness of 0.023 cm was employed. The thickness of individual samples was measured using digimatic micrometer (Mitutoyo Corporation, Japan). The membranes were washed with ethanol for 1h, and dried at 45°C.

Sodium chloride (99.9%) was purchased from VWR International. Acrylic acid (AA; >99%), benzophenone (BP; GC purity) and sodium acetate (>98.5%) were from Fluka. Acrylamide (AAm; >99%), and methylene bisacrylamide (MBAA; >99%) were from Aldrich. Heptane (>99%), methanol (>95%), ammonium sulphate (99.5%), 10 mM sodium hydroxide, potassium dihydrogen phosphate (98.0-100.5%) and dipotassium hydrogen phosphate were obtained from Applichem. Acetic acid (99.88%) was from Fischer Scientific. 1 mM Hydrochloric acid was from Waldeck. GalwickTM (1,1,2,3,3,3-hexafluoropropene) was from Porous Materials Inc. (PMI), Ithaca, NY, USA. Model proteins were lysozyme (Lys) from hen egg (crystalline, powder, 85,400 units / mg, from Fluka, and ~95% protein, ~50,000 units/mg", from Sigma), and γ-globulin (IgG) from bovine blood (≥ 97%, agarose gel electrophoresis, from Sigma).

The fluorescence dyes were 5-(4,6-dichlorotriazinyl) aminofluorescein (5-DTAF isoform; excitation/emission wavelengths of 492/516 nm) from Invitrogen and Cy5 mono-reactive NHS ester (excitation/emission wavelengths of 633/654 nm) from GE Healthcare.

Buffers were prepared using Milli-Q water. 10 mM potassium phosphate buffer, pH 7.0 (buffer A) and 10 mM potassium phosphate buffer with 1 M sodium chloride, pH 7.0 were used for the measurements of binding isotherm, membrane permeability and breakthrough curves of lysozyme. 20 mM sodium acetate, pH 5.0 (buffer B), was used for the measurements of IgG binding and dispersion. Sodium carbonate buffer (100 mM, pH 9.3) was used for protein labeling. Sodium phosphate buffer (variable ionic strength, pH 7.0) was used in the separation of labeled protein from native protein, and also in CLSM experiments.

## 4.2. Characterization of membranes

### 4.2.1. Microscopic methods

#### 4.2.1.1. Methods for SEM and measuring of wet samples using ESEM

Standard SEM image was performed at high vacuum using an environmental scanning electron microscope (QUANTA FEG 400, FEI, Eindhoven, The Netherlands). The samples were pre-coated with silver DAG 1415 (Plano GmbH, Wettlar, Germany) for 1 min. The samples for ESEM images were equilibrated in 10 mM phosphate buffer for 24 h, after slightly drying with fine paper sample were directly put into the ESEM chamber pre-set at a vapor pressure of 3.4 Torr, representing a relative humidity of 60%.

#### 4.2.1.2. Membrane dehydration / hydration investigations

***In situ study with ESEM***: The study was performed using the same ESEM with modest humidity in chamber. Variation of relative humidity was realized by variation of the pressure in the chamber at 2°C with help of a Peltier chip-controlled cooling stage (**Table 4-1**). Original Sartobind and gold coated Sartobind membranes were used. The gold coating on the membrane resulted from step-wise current-less metallization using the solutions PD 11, SLOTONIP 61 and SLOTOGOLD 10 (Schlötter Galvanotechnik, Geislingen, Germany), respectively, for surface activation by deposition of catalytic amounts of palladium, nickel deposition and nickel exchange to gold, respectively, under conditions where an incomplete surface coverage with metal can be achieved.

**Table 4-1.** ESEM relative humidity isobar chart at 2°C (*30*)

| vapor pressure [Torr] | 4.2 | 4.0 | 3.7 | 3.4 | 3.2 | 2.9 | 2.6 | 2.4 | 2.1 | 1.8 | 1.6 | 1.3 |
|---|---|---|---|---|---|---|---|---|---|---|---|---|
| rel. humidity [%] | 80 | 75 | 70 | 65 | 60 | 55 | 50 | 45 | 40 | 35 | 30 | 25 |

The preliminary experiment indicated that the regenerated cellulose is sensible to the variation of vapor pressure in the chamber and local heating by exposure of the beam resulting to bubbles or joining of fibers. Water drops were formed at a vapor pressure larger than 4.0 Torr, asespecially for Sartobind S membranes. As indicated by the relationship of saturated vapor pressure of water and temperature in the ESEM chamber, to attain saturation of the sample, it is desirable to drop the sample temperature just above freezing, and then only a modest gas pressure was needed to vary the saturation of sample. The membrane sample was pre-equilibrated to relative humidity of approx. 80% in a desiccator (containing a potassium chloride solution) at room temperature. At the beginning, a similar pump down sequence as described by Cameron and Donald (*131*) was carried out to ensure that air in the chamber was replaced with water and there was no premature evaporation of water. The sample was quickly put into the ESEM chamber pre-set at a vapor pressure of 2.9 Torr, representing a relative humidity of 55%. The time reaching this pressure again after inserting the sample into the chamber was ca. 10 min. By following this procedure, condensation of water on the membrane surface was prevented. It must be noticed, the pressure in chamber in this way consists of water vapour and the rest of air. Depending on membrane type and image magnification, the beam voltage was set at 10 or 15 keV and a working distance ≤ 6 mm. A variation of water vapor pressure followed, and the time to equilibrium for each condition was set to 5 min for the original membranes, and to 10 min for the gold coated membranes. The measurement was evaluated by using of image analysis software " Scandium 3.2, soft imaging system.

***Study by gravimetry:*** Moisture release and uptake rate of the original membranes was also measured independently by gravimetry. For measuring the water release, samples were pre-equilibrated in desiccator (~80% relative humidity, at 22°C) for over one week, and then the weight loss until equilibrium at 42% relative humidity at 22°C was measured using an analytical balance (Sartorius Genius, Göttingen). For measuring the water uptake, samples were dried in oven (at 50°C) for 24 h, shortly equilibrated under ambient conditions and

subsequently put into a desiccator with a humidity of 80%. The mass was quickly measured on the analytic balance after different time periods. The absolute moisture uptake/release data were normalized to the weight of the sample after drying in oven at 50°C for 24 h.

#### 4.2.1.3. Visualization of membrane morphology and protein binding by means of CLSM

***Staining of the membrane***: The membranes were stained with the hydroxyl-reactive fluorescence dye 5-DTAF. The incubation with dye solution and the following washing steps were performed using a filter holder (Swinnex, Millipore) with three membrane samples (diameter 13 mm) under continuous circulation at a flow rate of 1 mL/min. In each case, 20 ml DTAF solution in 100 mM sodium carbonate, pH 9.3, with an adapted concentration (15 µg/mL plus 100 mM NaCl for Sartobind S and 10 µg/ml for Sartobind C, 50 µg/ml plus 200 mM NaCl for new prepared crAAAm, 60 µg/ml plus 400 mM NaCl for new prepared crAAAm and AA membrane, respectively) was used. After circulation for approx. 18 h, the membranes were washed successively with 20% ethanol, 1 M NaCl and 200 mM sodium phosphate buffer, pH 7.0.

***Protein labeling and purification***: Lysozyme (from Sigma, cf. above) was labeled using a procedure described by Dismer and Hubbuch (*132*), with the amino-reactive fluorescence dye Cy5 mono-reactive NHS ester. 10 mg lysozyme (Sigma) was dissolved in 1 ml of 100 mM sodium carbonate buffer, pH 9.3, then added to an aliquot of Cy5-NHS ester (0.2 mg of Cy5 dissolved in 20 µl DMSO). After 1 h of reaction in a shaker at 800 rpm, the solution was centrifuged for 5 min and followed by purification and buffer-changing (20 mM sodium phosphate buffer, pH 7.0) with gel filtration (PD10 column, GE healthcare). For the static investigation of commercial membranes, the protein was then purified with gel filtration and then with HP ion-exchange chromatography. Only mono-labeled lysozyme fractions were pooled and subsequently concentrated using ultrafiltration to the concentration required for binding experiments. The concentration of the labelled lysozyme was measured by using of UV-Vis spectroscopy (Cary 50, Varian) and calculated after the equations (4-1) and (4-2) (*100*):

$$C_P = \frac{A_{280} - CF_D * A^D_{\lambda\max}}{\varepsilon^P_{\lambda\max} * d} \tag{4-1}$$

Where $CF_D$ is correction factor of respective dye at 280 nm, $A^D_{\lambda\max}$ is maximum extinction of

dye ( $A^{D}_{\lambda max}$ = 650 nm for Cy5), $\varepsilon^{D}_{\lambda max}$ is specific extinction coefficient of respective dye ( $\varepsilon^{D}_{\lambda max}$ = 25,000 $M^{-1}cm^{-1}$ for Cy5).

$$C_D = \frac{A^{D}_{\lambda max}}{\varepsilon^{D}_{\lambda max} * d} \tag{4-2}$$

Where $\varepsilon^{P}_{\lambda max}$ is specific extinction coefficient of respective protein ( $\varepsilon^{P}_{\lambda max}$ = 30,160 $M^{-1}cm^{-1}$ for lysozyme), $d$ is curveted distance (1 cm here).

***Membrane incubation with protein***: Membrane samples (diameter 5 mm) were incubated with labeled lysozyme for 15 min, 4 h and over night. The used concentrations were 0.03, 0.12 and 0.57 mg/ml (in 200 mM sodium phosphate buffer, pH 7.0, plus 50 mM NaCl) with a defined volume leading to a 2 fold excess of protein relative to the respective membrane static binding capacity according to the manufacturer, to minimize both the used amount of labeled protein and the depletion of protein solution. The samples were subsequently washed with 20 mM sodium phosphate buffer, pH 7.0, for 15 min. For investigation of protein binding pattern of new prepared membrane adsorber, a small piece of stained sample with a diameter of 5 mm was incubated in 900 µl Cy5 labeled Lys solution (0.4 mg/ml) for 2 h.

***CLSM analysis of commercial ion exchange membrane adsorber***: The analysis was carried out using the CLSM system Zeiss LSM510 equipped with a water immersion 63x/NA1.2 C-Apochromat objective lens. The system is provided with laser excitation sources at 488, 533 and 633 nm. Followed the identification of the beginning of the membrane (scanning depth z = 0) and characteristic membrane pore morphology at different z positions, detailed x-y scans were performed for both emission wavelengths at gain settings where non-specific fluorescence (i.e., by auto-fluorescence of the membrane material, or due to non-specific interaction of Cy5 with unstained membranes) could not be detected. The obtained images were stored as 8-bit scans and 4 scans were always averaged to reduce noise. Data reported have a dimension of 512×512 pixel representing an area of 146.2 × 146.2 $\mu m^2$.

***CLSM analysis of new prepared cation exchange membrane adsorber***: The visualization of protein binding was performed using laser module LSM 510 coupled with an inverted CLSM 100M BP from Zeiss, Germany. An immersion oil objective lens (Plan-Neofluar 100x/1.3oil

with total magnification of 1000 fold) was used. Membrane sample (immersed in phosphate buffer) was clipped between cover slips. CLSM images were generated in multi-track mode which allows separately recording of different signals corresponding to the respective laser wave-length. As the used 5-DTAF shows high susceptibility towards photobleaching, the image of membrane (488 nm) was scanned as first, followed by imaging of Cy5-labelled Lys (633 nm). The obtained images were stored as 8-bit scans and 4 scans were always averaged to reduce noise, data reported have a dimension of 512 × 512 pixel representing an area of 92.1 × 92.1 $\mu m^2$.

***Experimental setup for in situ monitoring of protein binding with CLSM:*** A self-designed membrane module was used for the *in situ* monitoring of protein binding using the inverse microscope (**Figure 4-1**). Main considerations for module design were a homogeneous flow distribution into the membrane and a small back pressure. The latter aspect was crucial because the distance between the objective of the microscope and the z-position in the membrane could not be larger than 0.07 mm, and the thickness of the glass should provide sufficient mechanical strength to withstand the pressure built up by the flow through the thin channel into the liquid outlet. The membrane module was directly connected to a HPLC pump (LC-10ADVP Shimadzu) in order to minimize dead volumes of the system. The module was equipped with an additional outlet connected to an elevated buffer reservoir together with a syringe for driving air bubbles out of the system before the start of an experiment.

A dye-stained Sartobind S membrane sample (diameter 12 mm) was installed in the module with the "bottom" side toward the observation glass. A droplet of Milli-Q water was used between the observation glass and objective. The flow rate was set to 0.3 ml/min, and the system was first equilibrated with buffer for 10 membrane volumes. A solution of a mixture of labeled and native lysozyme was used (protein concentration 1.7 mg/ml, 30% labeled protein). The protein solution was given in a 1 mL loop and injected to the module with a seven-port injection valve (7725i, Rheodyne). Simultaneously with the injection, image acquisition was started at the pre-chosen position of interest (at a distance of ~10 µm from the outer surface of the membrane), selected using an excitation wavelength of 488 nm, corresponding to the membrane bound dye. The x-y intensity profile for both emission wavelengths (488 and 633 nm) was measured with a time resolution of every 2 seconds and saved as an 8-bit single scan.

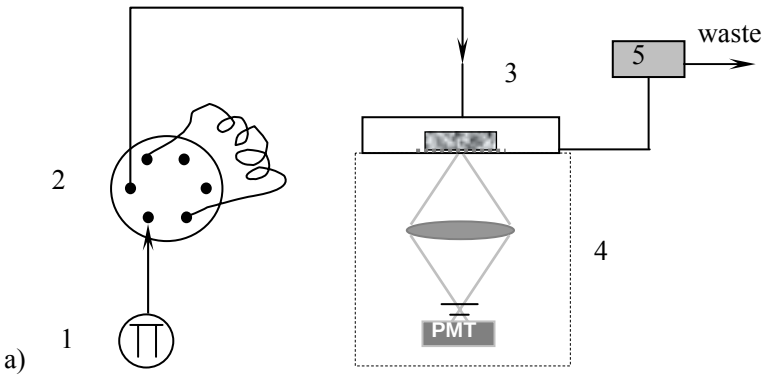


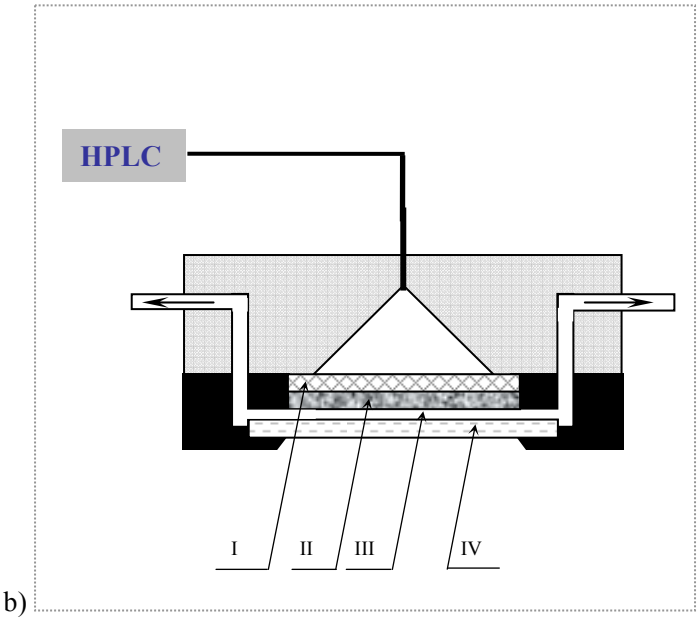


**Figure 4-1.** a) Setup for *in situ* monitoring of protein binding: 1. pump of HPLC, 2. seven-port injection valve, 3. membrane module, 4. Confocal Laser Scanning Microscope, 5. high position reservoir; b) construction of membrane module: I. distributor, II. membrane, III. channel for outlet liquid, IV. observation glass.

### 4.2.2. Characterization of membrane structure

#### 4.2.2.1. Membrane pore size distribution

Trans-membrane pore size distribution was determined by liquid displacement (*132, 133*), using the capillary flow porometer CFP-34RTG8A-X-6-L4 (PMI Inc., Ithaca, NY, USA). The instrument records the gas flow as a function of applied pressure during displacement of a wetting fluid from an initially saturated membrane, and this data set is related to the gas flow through the dry membrane. Samples with a diameter of 18 mm were characterized via the "dry up / wet up" method. For the "wet up" part, the membranes were wetted with Galwick$^{TM}$ with a surface tension of 16 $dyn \cdot cm^{-1}$. After wetting, the pore size distribution was evaluated automatically by taking the ratios of wet to dry gas flow for a given pressure range, 2 bar in this work. All measurements were done in duplicate.

#### 4.2.2.2. Membrane specific surface area

The specific surface area was determined by using the surface area analyzer SA 3100 (Beckmann-Coulter GmbH, Krefeld, Germany) and evaluating the nitrogen adsorption isotherm according to Brunnauer, Emmet und Teller (BET).

#### 4.2.2.3. Buffer permeability of membranes

Buffer flux measurements were performed to study the effects of functionalization. The circular membrane sample with 47 mm diameter was loaded into a flow-through cell (Sartorius, Goettingen). The cell was filled with 100 ml of Buffer A or Buffer A+1M NaCl, and connected to a nitrogen tank via pressure tubing. The feed pressure was set at 1 bar for the 3~5 µm and 1~2 µm membranes, at 3 bar for the 0.45 µm membranes. The permeate was collected in a beaker, and the permeate mass was measured by a balance. The respective permeability was calculated using the mass of permeate collected during a measured time at defined trans-membrane pressure. All measurements were done in triplicate.

### 4.2.3. Determination of ion-exchange capacity

#### 4.2.3.1. Total ion-exchange capacity by titration method

A membrane sample (diameter 50 mm) was cut into small pieces of about 0.5 × 0.5 $cm^2$. 25 ml 1 N HCl were added to the membrane sample and stirred 2 hours for complete protonation of carboxylic groups. Sample was than washed with Milli-Q water until the washing water was neutral. A known volume (depending on sample type between 65 and 90 ml) of 4 mM NaOH was added to the sample in an Erlenmeyer flask and kept closed for 24 h in order to reach equilibrium. A drop of the indicator phenolphthalein was added to the solution to control the excess of NaOH. A blank NaOH sample without membrane was always run in parallel. Aliquots of 15 ml were taken from the NaOH solution and titrated against 1 mM HCl while the change of pH value during the titration was measured using a pH electrode (pH/Cond-340i, WTW, Weilheim, Germany). All titrations were done in triplicate. The cation-exchange capacity was calculated from the average values, including the results of titer determinations for the NaOH and the HCl solutions as well as the respective blank values. The cation-exchange capacity was normalized by the respective mass of the grafted copolymer and expressed as μmol cation-exchange groups per mg grafted polymer.

#### 4.2.3.2. Dynamic ion-exchange capacity of membrane adsorber via pH transition

The pH transient method proposed by Strancar and coworkers (*112*, *113*) for porous monoliths, and already proofed to be feasible for polypropylene-based membrane adsorbers (*46*), was adopted to determine *in situ* the ion-exchange capacity of a membrane stack. Experiments were performed using an Äkta Purifier 900 (GE Healthcare Life Sciences) with a UV detector set at 210 nm. Five pieces of membrane with a diameter of 12 mm were stacked in a CIM® membrane module (BIA Separations, Ljubljana, Slovenia). Experiments were done at a flow rate of 5 ml/min. The membrane stack was first equilibrated with 0.5 M ammonium sulphate solution, pH 5.3, until pressure, UV absorbance, conductivity and pH were stable. Then the composition of the mobile phase was instantaneously switched to 20 mM ammonium sulphate solution, pH 5.3. The experiment ended when the pH of the effluent had reached a constant value, identical to the pH of the solution at the column inlet.

### 4.2.4. Static and dynamic protein capacity

#### 4.2.4.1. Static binding capacity and protein binding isotherms

Membrane samples (diameter 13 mm) were first equilibrated with Buffer A and then incubated in 5 ml of protein solution on a shaker for approximately 16 h in Petri dishes (diameter 60 mm). Initial lysozyme concentrations used to construct binding isotherms were 0, 0.01, 0.02, 0.05, 0.1, 0.5, 1, 2, 5 mg/ml in Buffer A. After rinsing with Buffer A, samples were eluted with Buffer A + 1 M NaCl for 1 h. Concentrations of the eluted and initial protein solutions were measured by UV spectrophotometry at 280 nm using a Cary 50 probe spectrophotometer. The bound amounts and equilibrium concentrations were calculated from the data for the initial and eluted protein solution. Langmuir adsorption isotherm was fitted to the experimental data using non-linear least-square regression. The determination of (maximum) static binding capacity was performed in the same way using an initial lysozyme concentration of 2 mg/ml. All measurements were done in duplicate and average values are reported.

#### 4.2.4.2. Breakthrough curves and dynamic binding capacity

Dynamic binding experiments were performed using an Äkta Purifier system (GE Amersham Pharmacia Biotech), the UV detector was set at 280 nm. All buffers were simultaneously degassed and prefiltered through a 0.2 μm cellulose acetate membrane (Sartorius Stedim Biotech) using a vacuum pump. The measurement was performed using two flat sheet membrane modules, a custom designed Sartorius membrane holder from Sartorius Stedim Biotech (SCell module) and the commercial CIM® module. The dead volume of Scell module and CIM® module was 1.2 ml and 0.3 ml, respectively, determined using 2% acetone as a tracer. For the determination using Scell® module, three membrane layers (diameter 30 mm) were stacked into a membrane holder (Sartorius Stedim Biotech) resulting in a membrane bed of 0.35 $cm^3$ active membrane area. For the CIM® module, three layers of the 0.45 μm and 1~2 μm membranes or 5 layers of the 3~5 μm membranes (diameter 11 mm) were stacked into the module with an effective volume of 0.02 $cm^3$ per layer of membrane. After equilibration with buffer A, 100 ml solution containing 1 mg/ml Lys in buffer A or 1 mg/ml IgG in buffer B were loaded using a 150 ml Superloop (GE Healthcare Life Sciences) at a flow rate of 1 and 10 ml/min, respectively.

The area between the curves for acetone tracer (system dispersion curve) and modified membranes with the different copolymers (breakthrough curve, BTC) corresponds to the

maximal dynamic binding capacity (max DBC) of the respective membrane type for the respective protein. The dynamic binding capacity at 10% break-through (10% DBC) was calculated from the respective breakthrough curves, i.e. the loading volume for $c/c_0 = 0.1$ and injected concentration of protein.

## 4.3. Synthesis of cation-exchange membrane adsorbers via UV-initiated graft copolymerization

Surface functionalization via UV-initiated grafting was implemented as described previously using a high intensity UV lamp (UV-A Print, Hoenle AG, Gräfelfing, Germany) with glass filter ($\lambda$ >300 nm) (*23*). First, membranes (diameter 50 mm) were coated with a solution of 10 g/l benzophenone in heptane. The non-polar solvent was used for the polar base membrane in order to minimize uptake of photo-initiator in the bulk of the cellulose. Afterwards, the membranes were immersed in a monomer solution in a Petri dish and fixed between two sheets of filter paper (no. 593, Whatman, U.K.). The overall monomer concentration of 60 g/l was kept constant in all experiments, and the content of cross-linker in the monomer mixture was 10 wt%. The composition of the monomer solutions was selected as described in **Table 4-2**. The UV irradiation time at an effective intensity of about 40 mW/cm$^2$ was varied as described below. Subsequently, step-wise extraction with water and 50% aqueous ethanol solution was carried out to remove un-reacted monomer, residual initiator and homo-polymer. After immersion in ethanol for 15 min, the membranes were dried at 45°C.

The degree of grafting (DG) per membrane area ($A_{mem}$) was determined gravimetrically from the weight of each sample before ($m_0$) and after grafting ($m_1$) according to equation (4-3):

$$DG = \frac{m_1 - m_0}{A_{mem}} \tag{4-3}$$

Two batches of membrane (Batch I and batch II) were prepared. For dynamic characterization, CIM module was used for batch I membranes and Sartorius cell was used for batch II membranes.

**Table 4-2.** Concentration of monomers in aqueous reaction mixtures used for membrane surface functionalization with different grafted architectures

| grafted copolymer | abbreviation for grafting type | monomer concentration [g/l] | | |
|---|---|---|---|---|
| | | AA | AAm | MBAA |
| poly(AA) | PAA | 60 | 0 | 0 |
| poly(AA-co-MBAA) | crAA | 54 | 0 | 6 |
| poly(AA-co-AAm-co-MBAA) | crAAAm | 27 | 27 | 6 |

## 4.4. Quantification of internal flow distribution of membrane modules based on zone rate modeling

Unmodified Hydrosart® stabilized regenerated cellulose membranes with pore size of 0.45, 1~2 and 3~5 μm from Sartorius-Stedim Biotech were used. Two modules for stacked flat sheet materials were used: a commercial CIM® module for discs (BIA Separations, Ljubljana, Slovenia) and a custom supplied membrane cell (SCell module) from Sartorius-Stedim Biotech. The CIM module has porous discs made of polymeric monoliths at the inlet and outlet of the module for flow distribution and collection. The inner diameter of the module (including the porous discs) is 11 mm.

The SCell module has an effective diameter of 25 mm with open flow channels at both the inlet and the outlet of the membrane module. (**Figure 4-2**) Breakthrough curves were measured using the Äkta Purifier (GE Healthcare Life Sciences) with the UV detector set at 280 nm. Three layers of membranes (effective diameter 11 mm for CIM®, 25 mm for SCell module) were stacked into the module and equilibrated with Buffer A. Thereafter 10 ml solution containing either 2 mg/ml of lysozyme or 2 wt% acetone, both in Buffer A, were injected using a 50 ml Superloop (GE Healthcare Life Sciences) at flow rates of 1, 5 and 10 ml/min.

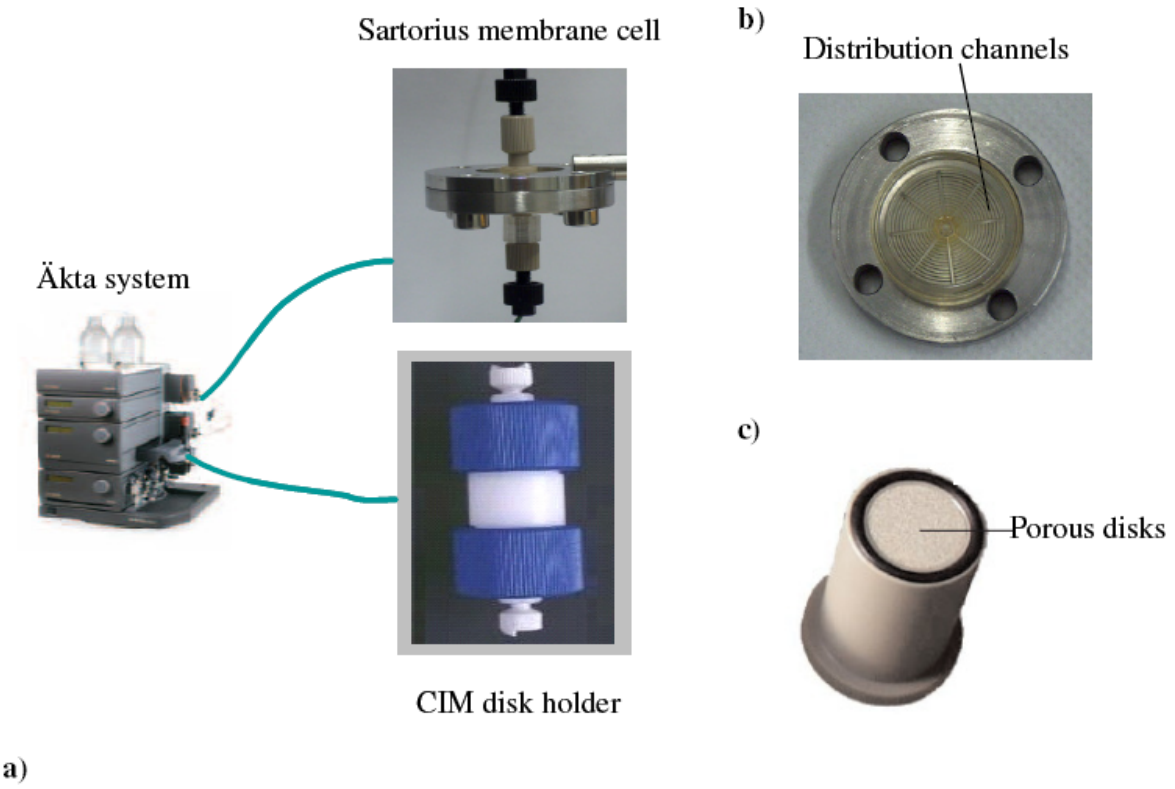


**Figure 4-2.** a) Breakthrough curves were measured using membrane modules: Scell and CIM membrane modules connected with Äkta system; b) distribution channels of SCell module. c) porous disk of CIM disk holder

# 5. Results

## 5.1. Characterization of commercial membrane adsorbers

### 5.1.1. Protein binding equilibrium of commercial membrane adsorbers

Binding isotherms for native lysozyme were measured to characterize the interactions of the model protein with the adsorbers (**Figure 5-1**), however only for the native lysozyme due to cost of the dye-labeled derivative. With membrane thickness of 230 µm, the $q_{max}$ for Sartobind S is 48 mg/ml, and the $K$ is 76 ml/mg (or $1.08*10^6$ L/mol), while the $q_{max}$ for Sartobind C is 23 mg/ml and the respective $K$ is 62 ml/mg (or $8.86*10^5$ L/mol). As the $q_{max}$ is measured under the same conditions as static binding capacity (SBC), the value of $q_{max}$ is equal to the SBC of the membranes. The measured maximal binding capacity of the Sartobind S membrane for Lys is much larger than the data given from the manufacturer for BSA (Static binding capacity is 0.8 mg/cm$^2$ (29 mg/ml) for Sartobind S and 0.6 mg/cm$^2$ (22 mg/ml) for Sartobind C (*58*).

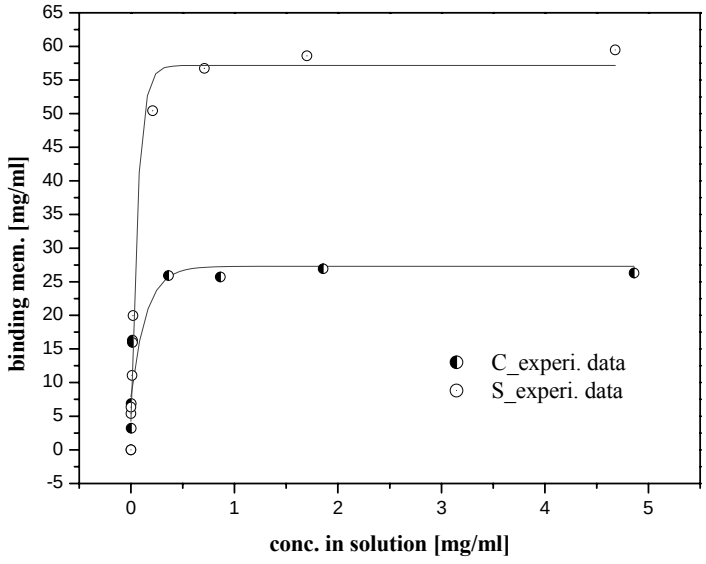


**Figure 5-1.** Binding isotherm for lysozyme on Sartobind S and C membranes measured by batch incubation; The fit to the data was calculated using nonlinear least square regression.

From the complete breakthrough curve one can also retrieve information about the dynamics of solute binding in the adsorber as function of mass transfer and binding kinetics. System dispersion curve (SDC), measured with an inert tracer, represents the behavior of system non-ideality caused by back-mixing or channeling as well as effects of the volume of different components. This is especially important when the volume of the adsorber (here the membrane stack) is smaller than the volume of the capillaries, flow distributors etc. in the system. For instance, the breakthrough curves for Sartobind S and C membrane for Lys measured in Sartorius cell module as illustrated in **Figure 5-2**. Acetone was used for the measurement of system dispersion without binding. At 1 ml/min, the max.DBC for Lys was 24.2 mg/ml and 44.9 mg/ml for Sartobind C and S, respectively (see **Table 5-4** and Section **5.2.6.).** The static and dynamic protein binding patterns of commercial Sartobind S and C membrane will be followed by microscopic methods.

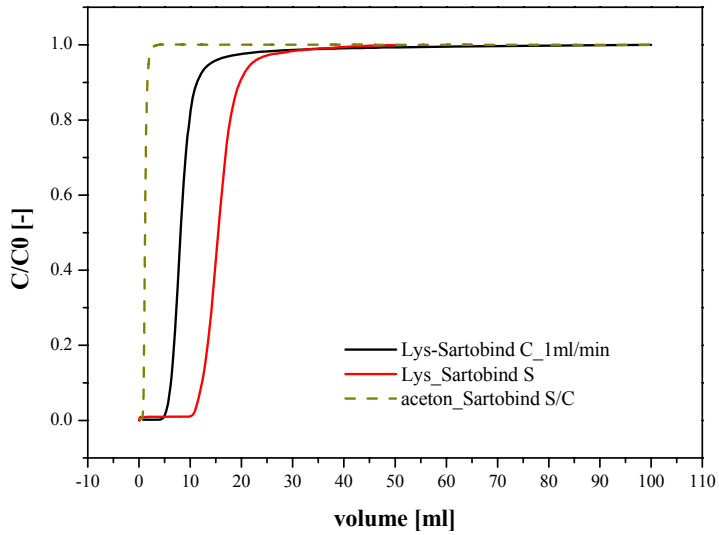


**Figure 5-2.** Breakthrough curves binding with 1 mg/ml Lys for Sartobind® S and C membranes at 1 ml/min. 3 membranes were stacked in the Scell module. System dispersion was measured using 1% acetone.

### 5.1.2. Detailed analysis of membrane adsorber pore structure and protein binding by advanced microscopy

#### 5.1.2.1. Membrane morphology

The SEM cross-section image (**Figure 5-3**) illustrates that the Sartobind membranes have an anisotropic macroporous structure. The mechanical stability of the membrane is mainly connected to thick fibers with a diameter of about 10 µm. The occurrence of these fibers is concentrated to the middle section of the membrane. However, few fibers are also seen directly beneath the outer surface. Therefore, the pore morphology in the regions close to outer surface is slightly different from the rest of the membrane. In general, the morphology of Sartobind membranes is very diverse, irregular and complex when compared to typical microfiltration membranes.

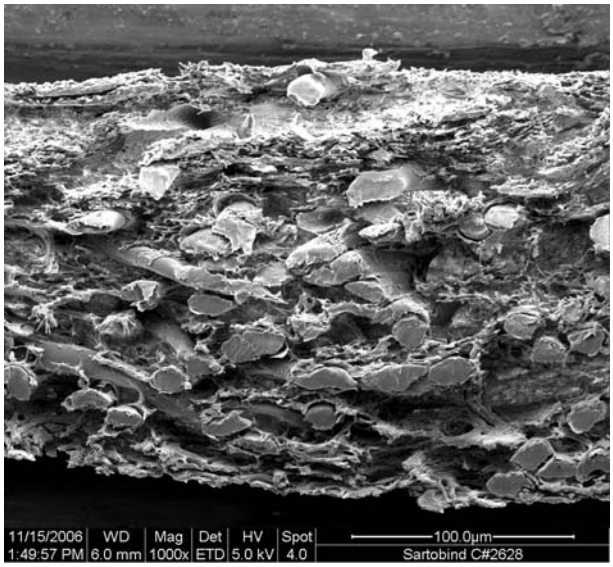


**Figure 5-3.** SEM image of a cross section of membrane Sartobind C. The sample was embedded in paraffin, cut with a microtome, washed with ether and ethanol, and dried.

The typical morphology for the bottom side of Sartobind S and C membrane in dry (**Figure 5-4a**) and wet state (**Figure 5-4c**) is a very coarse structure, consisting of relatively thick cellulose-based fibers connected to a network of fine fibers and clustered membrane material, together forming the macropores on the outer surface. The CLSM image in buffer of a fluorescence-stained membrane, ~10 µm from the outer surface, reveals that the very coarse structure containing the macroporous cellulose fiber network is characteristic also for the inner structure of the membranes (**Figure 5-4b**). The diameter of the larger pores is larger than 15 µm. It had been found that membrane morphology in buffer can be visualized using CLSM to ~20 µm depth, i.e. a complete profile can not be obtained under those conditions.

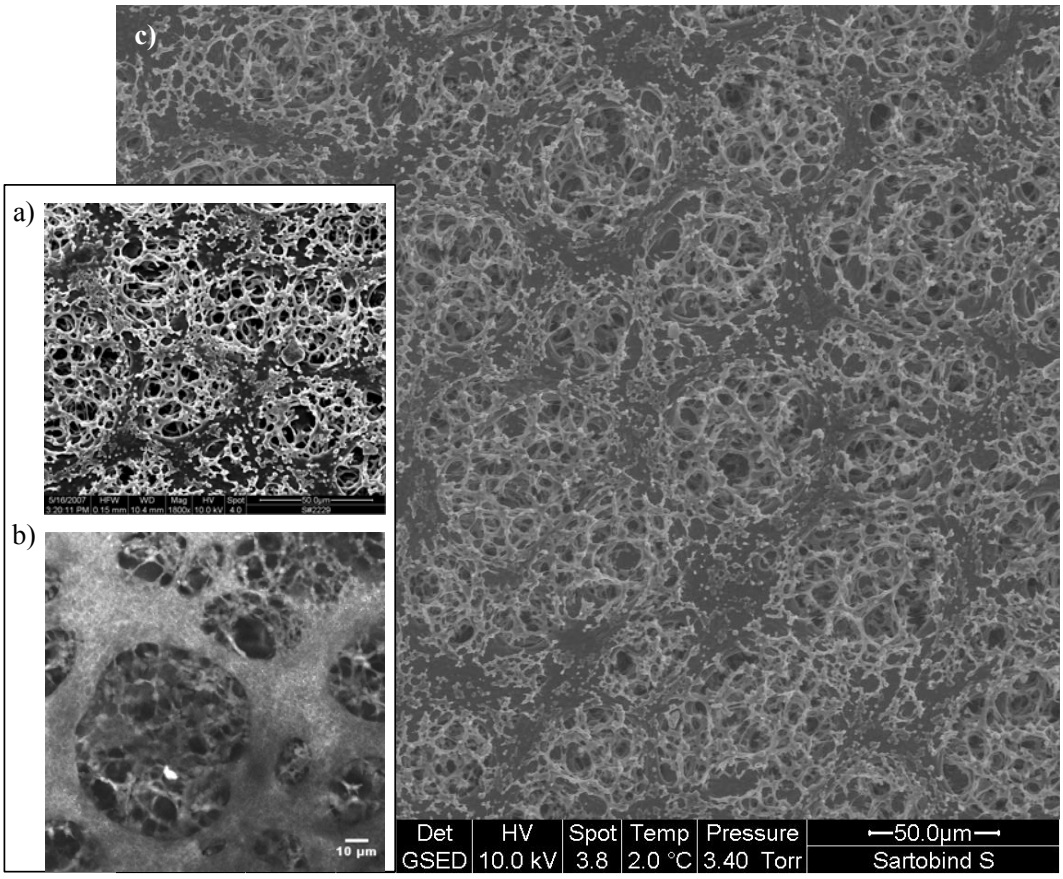


**Figure 5-4.** Morphology of membrane Sartobind S, bottom side: a) SEM image of outer surface in dry state; b) CLSM image in a depth of 10 µm in 50 mM phosphate buffer; c) ESEM image of outer surface at 2°C and 3.4 Torr after equilibration in 10 mM phosphate buffer for 24 h.

**Figure 5-5** illustrates the CLSM images gallery of membrane in different depths for Hydrosart membrane (**Figure 5-5a**) and Sartobind C after bound with Cy5-labelled Lys (**Figure 5-5b**). The membrane was stained with 10 µg/ml DTAF prior to visualization. Only a little part of matrix structure was visible at earlier depth. The optimal image was obtained in the depth ~ 10 µm (depending on the definition of start point). The scanning proceeded into the matrix structure, the brightness of the images attenuated, and this reduction was significant from the depth of ~16 µm. The degree of faintness of images was enhanced with the increasing of scanning depth. The images were so dark that the morphology of membrane was difficult to identify. It was found that depending on the property of the membranes, and subsequently the efficiency of labeling technique, the effective visible depth for membrane or bound protein could be different, however not larger than ~20 µm.

When scanning the"top" side of the membrane, significant differences in the pore morphology have been observed, the consistency between the three methods however remained. The typical morphology of the "top" side region is a more narrow network of the thick cellulose-based fibers connected to the fine fibers and clusters forming the macropores, i.e. the apparent porosity is lower than for the "bottom" side (**Appendix Figures 8-1~4**).

a)

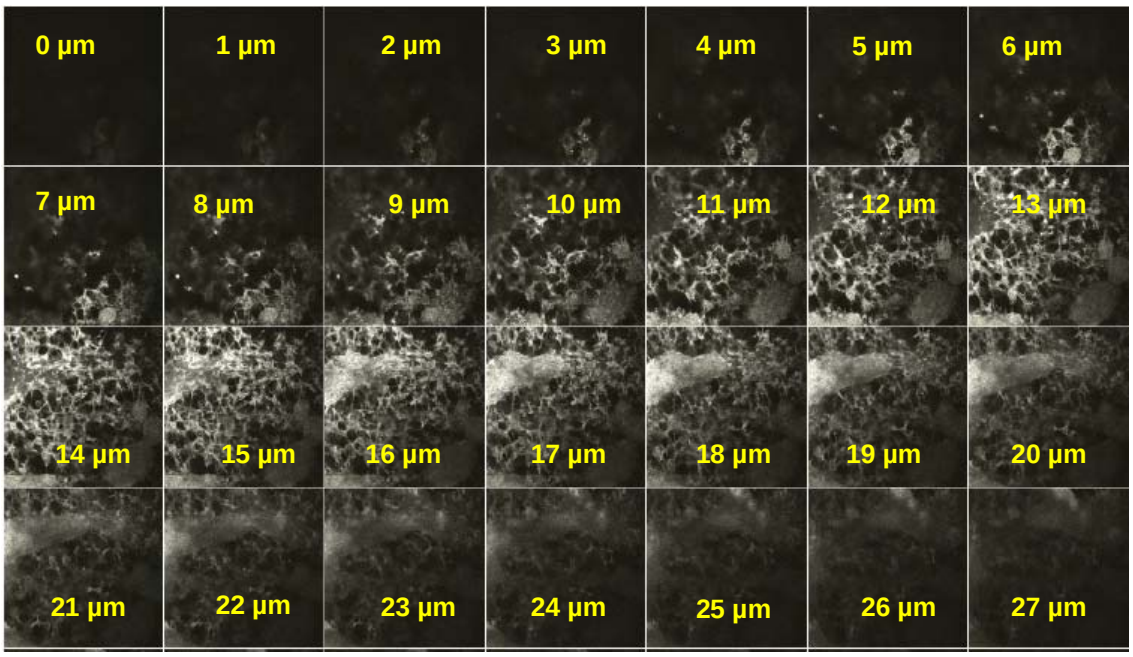


b)

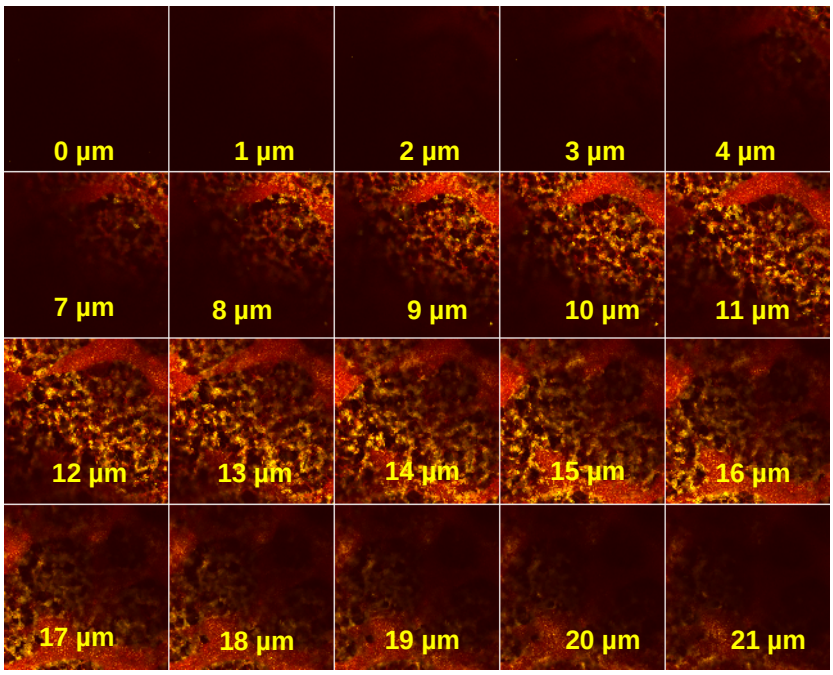


**Figure 5-5.** CLSM images of a) 3~5 µm membrane Hydrosart membrane (488 nm); b) 0.43 mg/ml Cy5-labelled Lys (633 nm) bound to Sartobind C (488 nm), bottom side. From upper-left side, the distance between scannings was 1 µm in z-direction.

### 5.1.2.2. Membrane hydration/dehydration

Data for *in situ* dehydration of water vapour saturated Sartobind C membrane is shown in **Figure 5-6**. After reducing relative humidity from 55% (**Figure 5-6a**) to 40% (**Figure 5-6b**), the small cellulose fibres became thinner than in the saturated state. Overall, the apparent porosity increased slightly with decreasing vapour pressure in the chamber (**Figure 5-6b-d**), but the most pronounced changes (exemplary regions indicated by arrows in the images) occurred at the pressure of 2.1 Torr. The shape of the macro-pore network defined by the strongest fibres did not change much.

Because of the sensitivity to the electron beam and the non-conductivity of the material itself, the untreated Sartobind membrane did not allow larger magnification in ESEM (**cf. 4.2.1.2.**). A Sartobind membrane, coated with gold from solution (**cf. 4.2.1.2.),** was therefore used for visualization of thick and thin fibers forming the macropores at a magnification of 20,000 fold (**Figure 5-7**). The few particular agglomerates in the images are gold particles as proven by EDX analysis. Coating conditions do not achieve compact layer.

With decreasing vapour pressure, significant dehydration of fibres with diameters in the sub-µm range was observed. The reduction in area was maximal 30% (**Figure 5-7a, 7d**). The distance between the fibres and largest gold agglomerate, which seems to be sticking to fibres, increased about 3 fold (**Figure 5-7a, 7d**). The maximum enlargement of the large pore (left side in **Figure 5-7**) was 34%. Similar to the data for the original membrane (cf. **Figure 5-6**), the most pronounced changes occurred at a relative humidity of 40%. If the pressure reduced from 2.9 to 2.1 Torr, the area of the large pore increased by about 25%. The increase of pore diameter might be caused by a deformation of pore shape through the dehydration. The partial gold coating increased the image resolution while the swelling/shrinking properties of the cellulose fibres remained essentially unchanged.

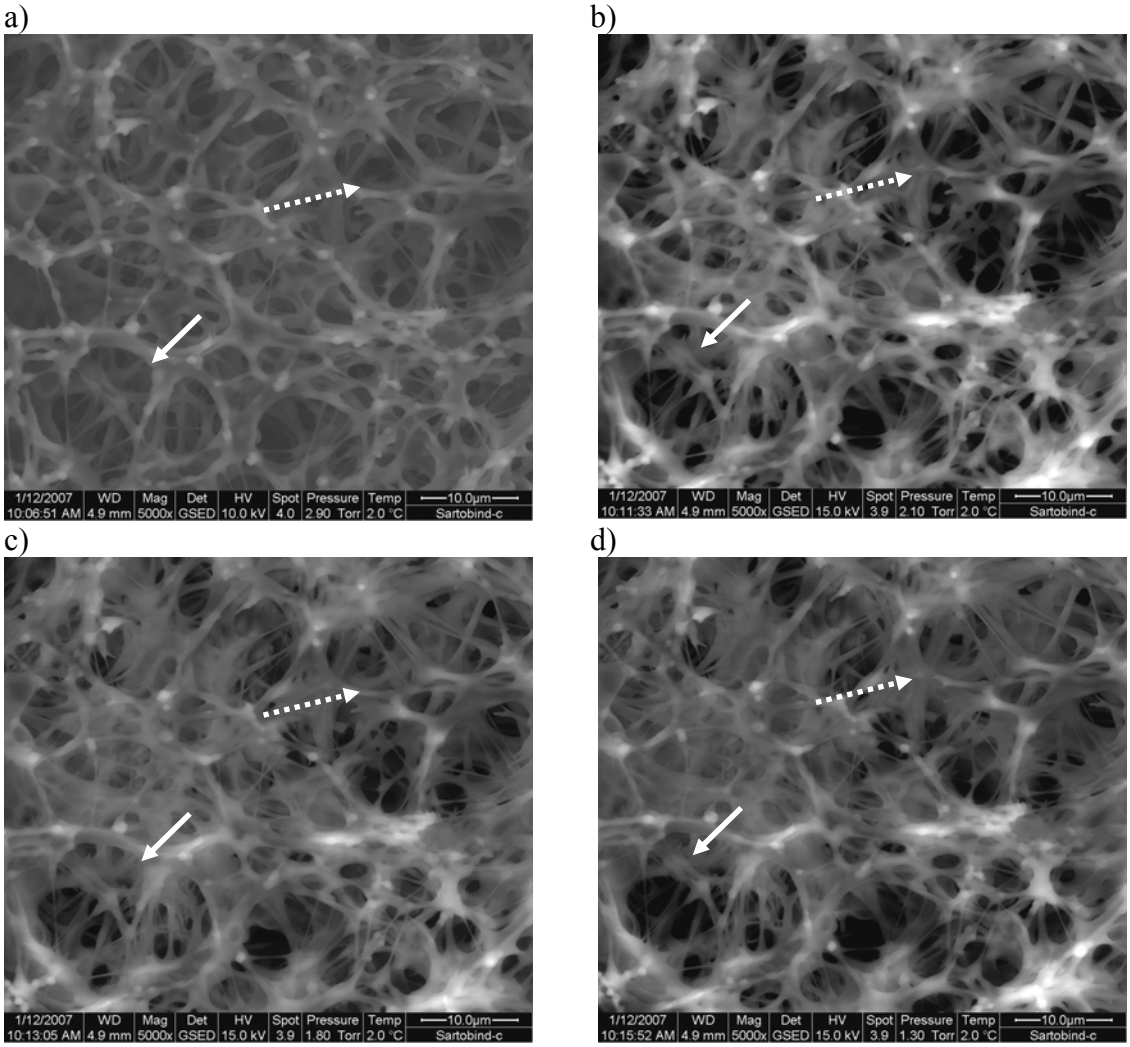


**Figure 5-6.** Dehydration of Sartobind® C membrane , bottom side, in ESEM chamber at 2°C (magnification 5,000). The vapor pressure was a) 2.9 Torr (~55% rel. humidity); b) 2.1 Torr (~40% rel. humidity); c) 1.8 Torr (~35% rel. humidity); d) 1.3 Torr (~25% rel. humidity). The scale bar of images is 10 µm.

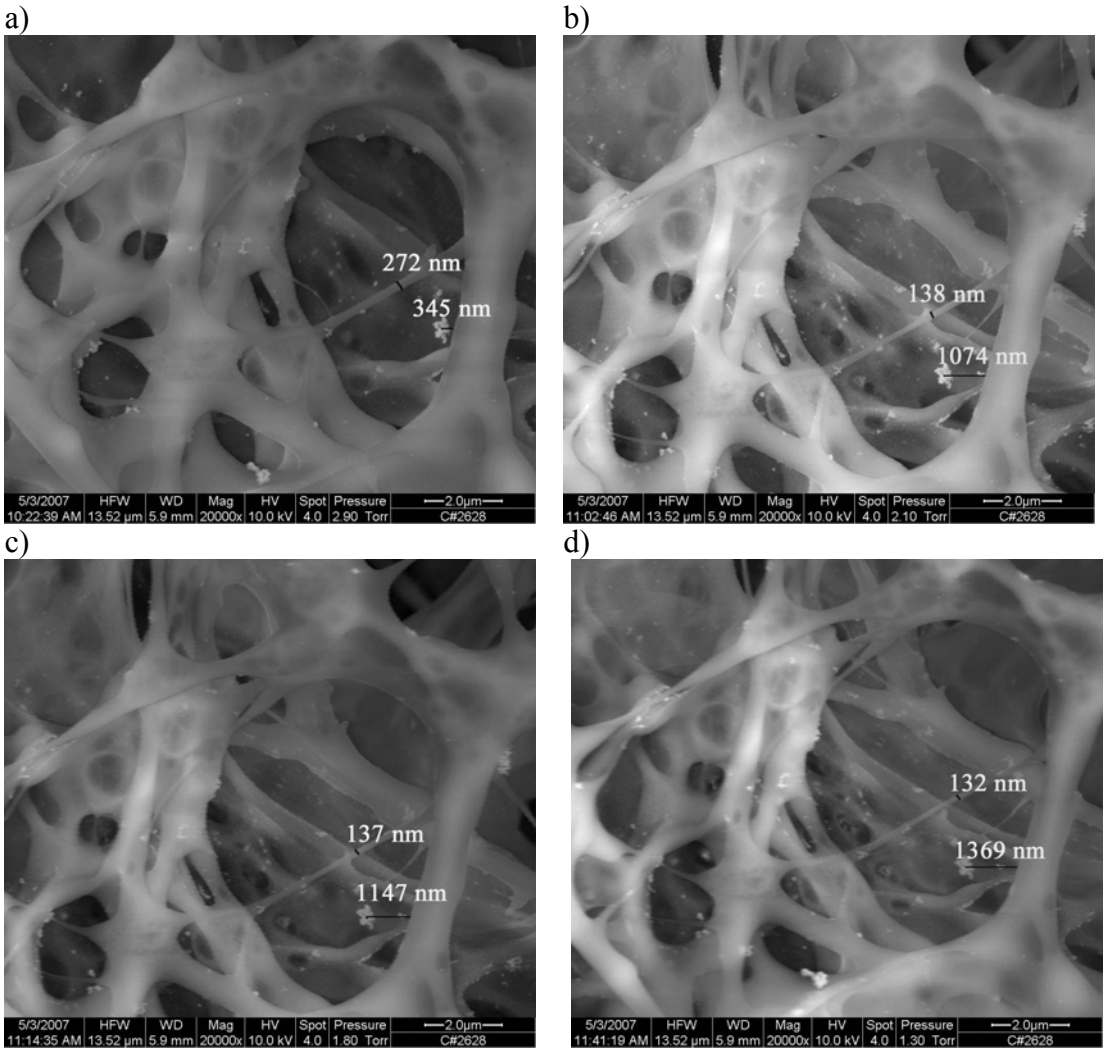


**Figure 5-7.** Dehydration of gold-coated membrane Sartobind® C, bottom side, in ESEM chamber at 2°C (magnification 20,000): The vapor pressure was a) 2.9 Torr (~55% rel. humidity), b) 2.1 Torr (~40% rel. humidity), c) 1.8 Torr (~35% rel. humidity), d) 1.3 Torr (~25% rel. humidity); the data were measured using "Scandium 3.2, soft imaging system" and the image was produced using "Photoshop element 3.0".

Similar morphology changes upon reducing the water vapour pressure had been observed for Sartobind S membranes. The difference between the S and C membranes can be related to the ability of water release and uptake presented in **Table 5-1**. Cellulose-water interactions occur either in inter-crystalline regions or on the surfaces of the crystallites and the gross structure. The bound water is thought to consist of water adsorbed by hydrogen bonds to free hydroxyl groups in the accessible regions of cellulose and water held in layers above the first adsorbed layer (*134*). The moisture uptake of Sartobind S membranes was faster than that of Sartobind

C membrane, while the release rates for both membrane was identical within the first 20 min. Either water uptake or release reached relative stable values within 16 h, somewhat higher values were observed for Sartobind S.

**Table 5-1.** Moisture uptake/release of Sartobind membranes

| mass of water vs. mass of membrane [%] | time | | |
|---|---|---|---|
| | 0 min | 20 min | 16 h |
| Sartobind C_uptake | 1 | 4 | 9 |
| Sartobind S_uptake | 4 | 6 | 10 |
| Sartobind C_release | 9 | 4 | 1 |
| Sartobind S_release | 10 | 5 | 1 |

#### 5.1.2.3. Batch protein binding and static visualization of protein binding by CLSM

**Figure 5-8** and **Figure 5-9** show results of simultaneous visualization of pore morphology and protein binding pattern for Sartobind S and C membranes, obtained after binding of Cy5-labeled protein from a concentration of 0.43 mg/ml for 4 h to fluorescence-stained membranes. The control experiments with unmodified cellulose membranes had proven that the fluorescence-labeling of the membrane did not increase lysozyme binding capacity. **Figure 5-8a** and **Figure 5-9a** show the bound protein detected at 633 nm, **Figure 5-8b** and **Figure 5-9b** show the stained matrix detected at 488 nm, and the overlap of images at both wavelengths is given in **Figure 5-8c** and **Figure 5-9c**. For the Sartobind S membranes, the protein binding pattern was similar to the pore morphology, and the protein filled in a relatively thick and homogeneous layer significant fraction of the macropores leaving the interior of the pore empty, while the bound protein density was much lower in the region of the thick cellulose fibers (**Figure 5-9a**). For the Sartobind C membranes, a more clustered protein pattern in the macropore space was observed, again with very little detectable protein on the thick cellulose fibers (**Figure 5-8a**). The overlap of the bound protein to stained membrane indicated that for both membranes the protein binding proceeds mainly in a layer which is anchored to the cellulose fiber network, and to a lower degree directly on the cellulose. Because of the limited thickness of this functional layer containing the ion-exchange groups, significant fractions of the pore volume remained dark.

The protein binding patterns within the pore structure of Sartobind membranes were also visualized after batch incubation with Cy5-labelled lysozyme for different times and at varied concentrations. In control experiments with an unmodified cellulose-based membrane of the same pore structure either stained or unstained membrane did not exhibit significant nonspecific binding of the labeled protein at the used gain of the CLSM system.

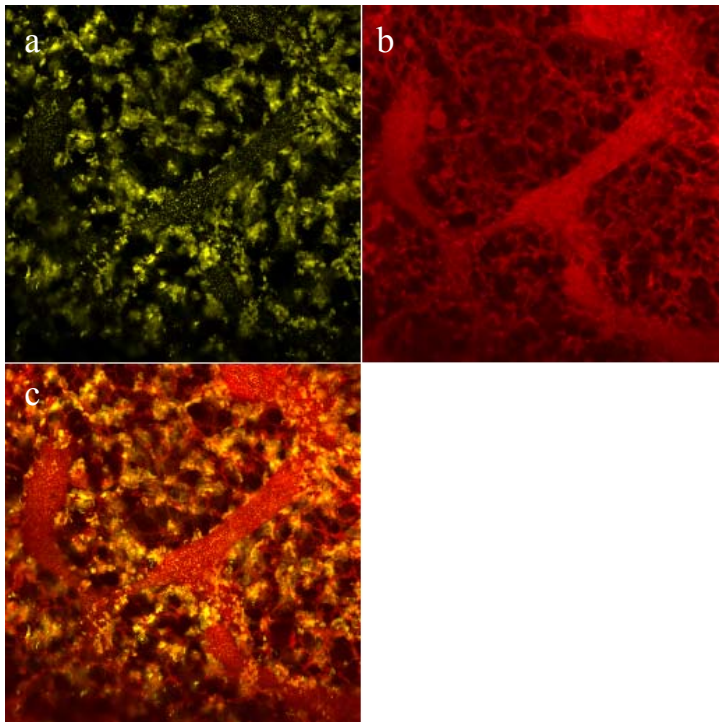


**Figure 5-8.** CLSM images of Sartobind® C membrane, bottom side, 7 µm from the outer surface: a) bound Lys from 0.43 mg/ml (633 nm); b) stained membrane (488 nm); c) overlap of labelled protein binding to stained membrane.

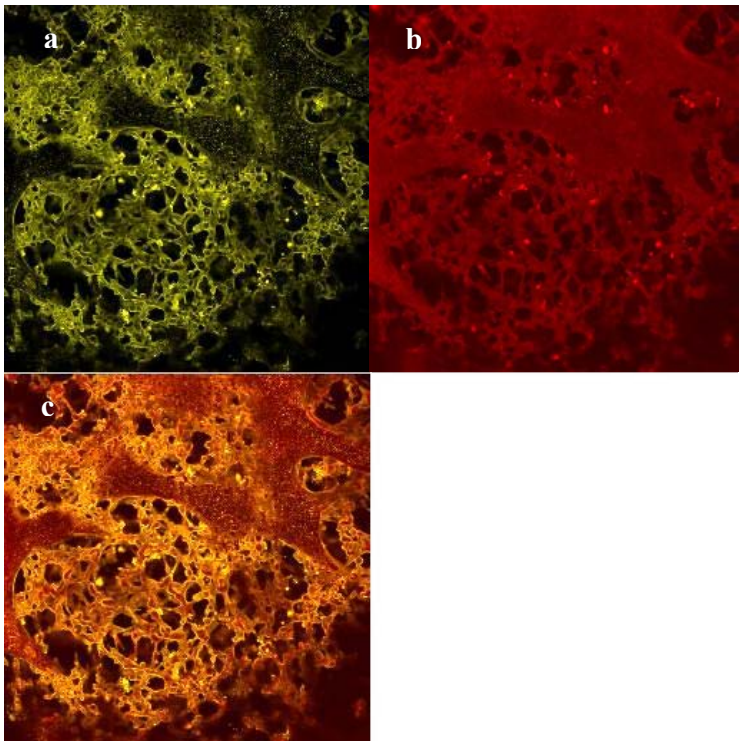


**Figure 5-9.** CLSM images of Sartobind® S membrane, bottom side, 7 µm from the outer surface: a) bound Lys from 0.43 mg/ml (633 nm); b) stained membrane (488 nm); c) overlap of labelled protein binding to stained membrane.

The concentrations of Cy5-labeled lysozyme in the CLSM experiments were 0.03, 0.12 and 0.57 mg/ml, corresponding to the linear and near plateau region of the binding isotherms for Sartobind S and C (cf. **Figure 5-1**), under the assumption that the interaction of unlabeled protein to the membrane is similar to that of the labeled protein isoform. As the used amount of protein was calculated according to the data of manufacturer, but measured values were larger than that (cf. **Section 5.1.1.**), the initial concentration of 0.57 mg/ml for Sartobind S was shifted to the left, the beginning of the plateau region (**Figure 5-1**). **Figure 5-10** presents data obtained by CLSM for the bottom side of the Sartobind S membranes after contact with different concentration and incubation time. While the protein binding patterns were similar to that in **Figure 5-8** and **Figure 5-9**, the intensity distribution was significantly different. The coverage of all fine pores with protein was laterally quite homogeneous after binding from 0.03 mg/ml for 15 min (**Figure 5-10a**). However, an increase in time and concentration yielded a more clustered protein binding pattern (cf. **Figure 5-10b** and **5-10c)**. Such apparent differences became even smaller with increasing protein concentration and for the results with a protein concentration of 0.57 mg/ml no significant difference as function of incubation time

could be identified (cf. **Figure 5-10e** and 5-**10f**). Also, the binding patterns did not exhibit differences after incubation over night for all concentrations (cf. **Figure 5-10a**, **5-10d**, and **5-10f**). It was found that the protein binding capacity had been saturated after 4 hours.

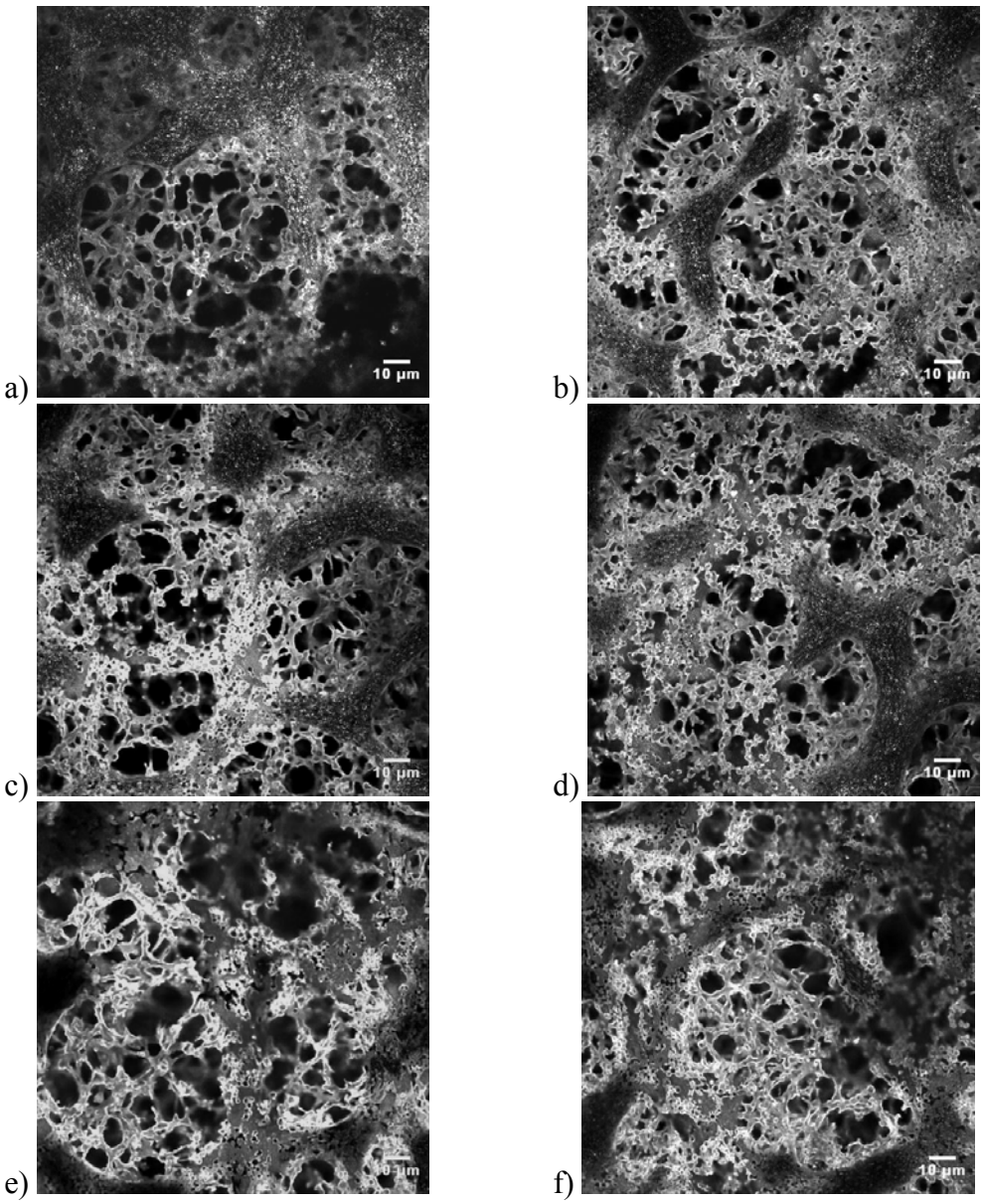


**Figure 5-10.** CLSM image (633 nm) of unstained Sartobind® S membrane, bottom side, 6 µm from the outer surface, after binding of Cy5-labelled lysozyme isoform: a) from 0.03 mg/ml for 15 min; b) from 0.03 mg/ml overnight; c) from 0.12 mg/ml for 15 min; d) from 0.12 mg/ml overnight; e) from 0.57 mg/ml for 15 min; f) from 0.57 mg/ml overnight in phosphate buffer.

#### 5.1.2.4. *In situ* monitoring of protein binding under flow through by CLSM

The protein binding in the porous membrane adsorber was *in situ* monitored using a special flow-though membrane module (cf. **Figure 4-1**). An excess of a mixture of labeled and native lysozyme was injected as step function. Exemplary results for the Sartobind S membrane, in a distance of ~10 µm from the bottom surface, are shown in **Figure 5-11**. In the right panel, the morphology of the stained membrane has been observed at 488 nm. In the left panel labelled lysozyme has been monitored at 633 nm. The gain to acquire the membrane images was set higher than in the previous experiments (cf. **Figure 5-4b** and **5-9b**), in order to identify eventual changes of pore structure. After a time delay of 60 s following the injection of the protein solution, the first trace of protein appeared as small spot on the left panel. The area of protein binding increased within the subsequent ~20 s and trended to become stable after 80 s. The image for bound lysozyme distribution at 84 s (**Figure 5-11**) was essentially identical to data obtained for the same membrane after batch adsorption for at least 15 min (cf. **Figure 5-10**). Protein was preferentially bound in a layer on the fine distributed cellulose fibers forming the macropores. Also, it should be noted that the protein in solution and in the pore volume was not visible. This can be well explained by a significant increase of local protein concentration upon binding to the adsorber surface.

However, the images of the membrane in the right panels changed notably during the process. Consistently between 72 and 80 s after protein injection, the membrane moved out of the previous z focus of the CLSM objective. This might have been caused by the applied flow and the slightly altered viscosity of the protein solution compared to pure buffer, or, most probably, by a morphology change imparted by the protein binding to the functional layers (cf. (*135*)) occurring exactly in this time interval.

The elution of bound protein using a high salt concentration was also monitored. It was clearly observed that the protein signal disappeared within few seconds to about 1 minute depending on the concentration of salt. However, images for labeled protein showed very high intensity fluctuations, which can be explained by high local concentrations of protein in the elution peak, but also additional influences of refraction index change or change of membrane swelling, both due to change of salt concentration. Therefore, these images are not shown and further discussed in this work.

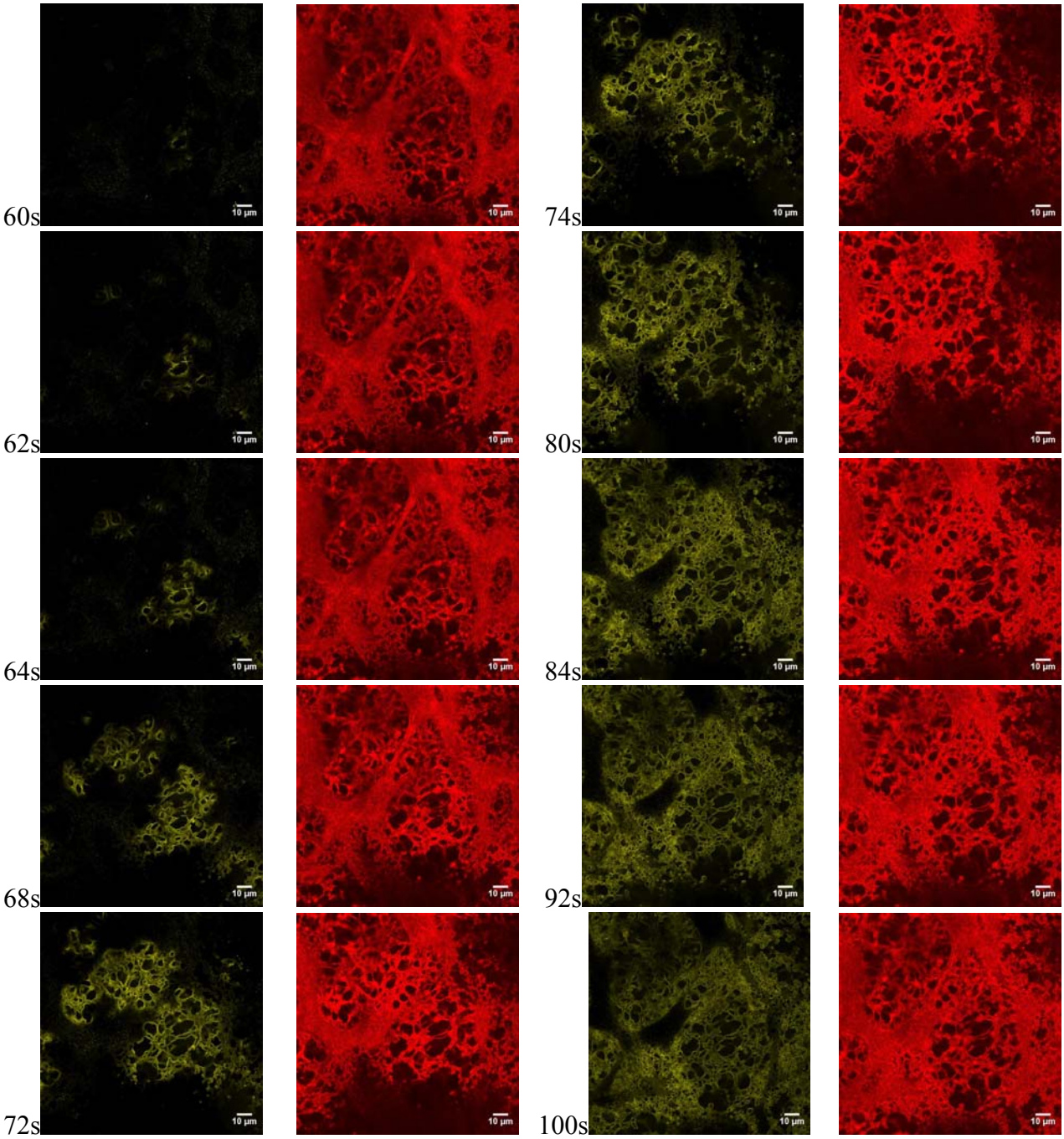


**Figure 5-11.** Time resolved images for lysozyme binding from a 1.7 mg/ml (30% labelled isoform) solution in Sartobind® S membrane, ~10 µm from the outer surface. Left: Cy5 labelled lysozyme (633 nm); right: stained membrane (488 nm).

## 5.2. Preparation and characterization of novel membrane adsorbers

### 5.2.1. Membrane pore structure and permeability

Hydrosart membrane is made from regenerated cellulose. Cellulose is a naturally occurring polysaccharide. The glucose segment contains three hydroxyl groups which are very susceptible towards chemical reaction forming esters and ethers. It is not well soluble even in polar solvents due to crystallinity and intermolecular hydrogen bonding between the hydroxyl groups. The glucose repeating units in cellulose are connected by 1,4-glucosidic linkages (**Figure 5-12**) (*133*). Cellulose is converted via chemical esterification and subsequent precipitation. Regenerated cellulose is obtained by cleavage of ester. Their hydrophilicity is greatly improved due to reduced crystallinity of structure (*136*). Cellulose-based materials are widely used in the biopharmaceutical processing industry due to its abundant availability, less binding capacity with protein, biodegradability, and compatibility with biological systems.

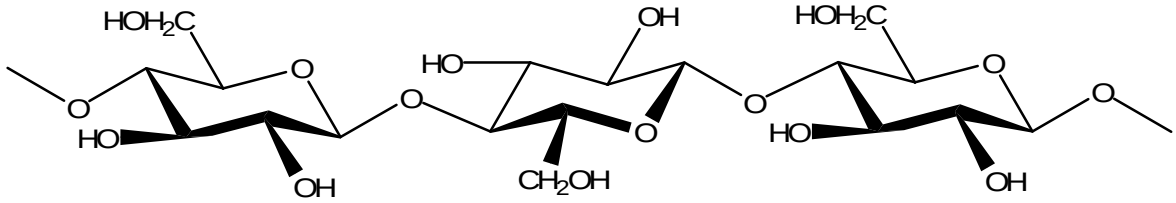


**Figure 5-12.** Chemical structure of cellulose

The SEM images of used base membranes with pore size of 0.45 μm, 1~2 μm and 3~5 mm, are shown in **Figure 5-13** for both sides. They present very coarse structure containing the macroporous cellulose fiber network on the both surface. The cross section of membrane as illustrated in **Figure 5-3** shows that the membrane structure is anisotropic. The mechanical property is enhanced by a kind of thick polymer fibres which should not bind protein. Generally, the morphology of Hydrosart membrane is very irregular, diverse and complex.

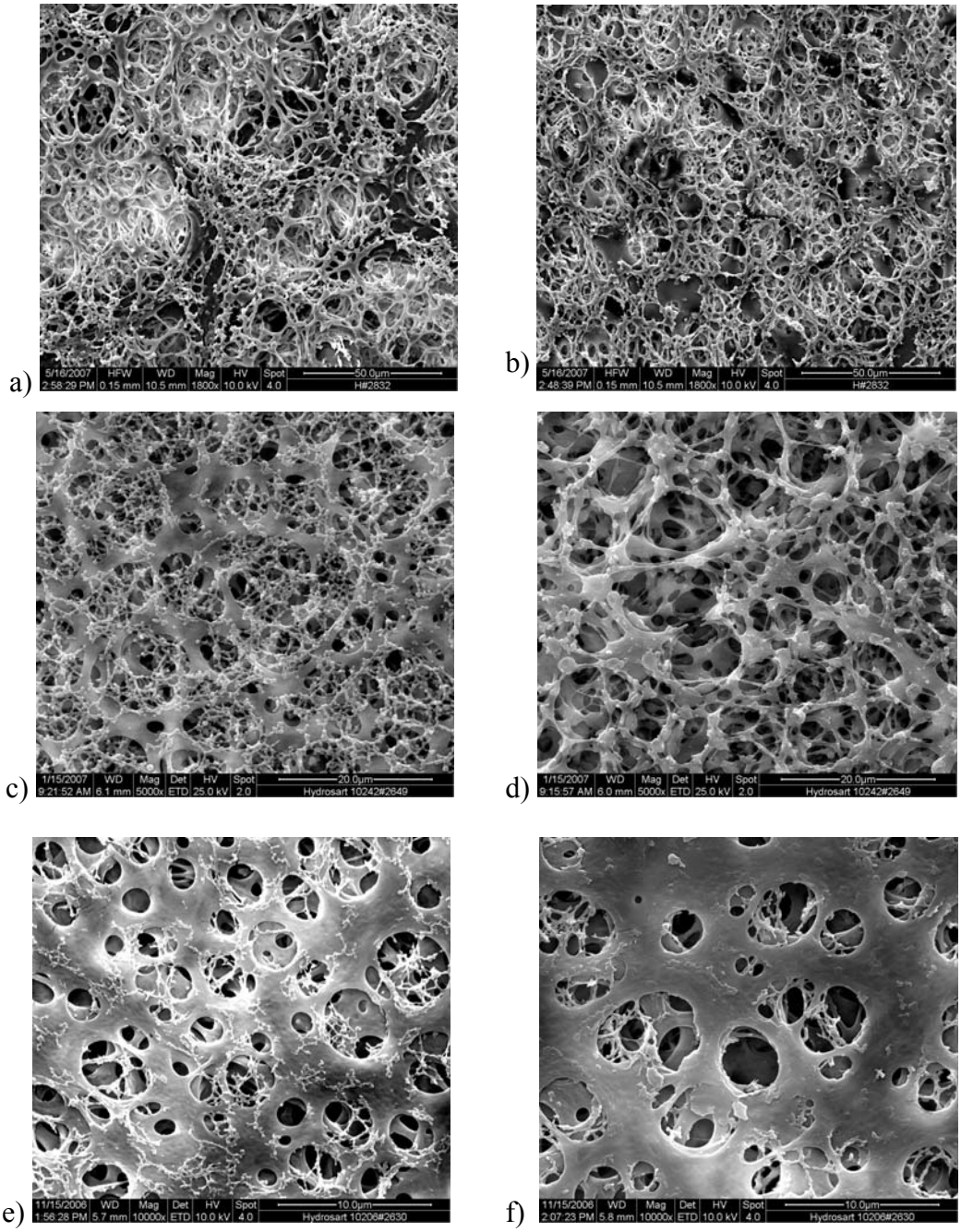


**Figure 5-13.** SEM images of Hydrosart® base membranes. a) Hydrosart 3~5 µm, 10242 #2832, bottom side, ×1,800; b) Hydrosart 3~5 µm, 10242#2832, top side, ×1,800; c) Hydrosart 1~2 µm, 10242#2649, bottom side, ×5,000; d) Hydrosart 1~2 µm, 10242#2649, top side, ×5,000; e) Hydrosart 0.45 µm, 10206#2630, bottom side, ×10,000; f) Hydrosart 0.45 µm, 10206#2630, top side, ×10,000.

The mean values and distributions of trans-membrane pore size for the base membranes, both measured by liquid displacement, are presented in **Table 5-2** and **Figure 5-14**. The experimental mean values agree well with the nominal data of the manufacturer. For unmodified 0.45 μm membrane, about 50% of the total number of pores had a diameter between 0.41 and 0.43 μm, and the entire distribution was narrow (from 0.32 μm to 0.55 μm, **Figure 5-14a**). The distributions were much wider for the two other, 1~2 μm and 3~5 μm, membranes. For the 1~2 μm membrane, 28% of the total number of pores was between 1.0 and 1.1 μm. The entire distribution covered the range from 0.5 to 1.5 μm (**Figure 5-14b**). For the 3~5 μm membrane, 57% of the total number of pores were between 1.5 and 2 μm. The entire distribution covered the range from 1.3 to 8.5 μm (**Figure 5-14c**).

**Table 5-2.** Specifications of the unmodified base membranes

| base membrane* [μm] | experimental mean pore size [μm] | liquid permeability_buffer A [l/(h*m²*bar)] | specific surface area [m²/g] |
|---|---|---|---|
| 0.45 | 0.45 | 26,590 ± 930 | 2.07 |
| 1~2 | 1.13 | 94,400 ± 1130 | 1.02 |
| 3~5 | 2.19 | 199,580 ± 5980 | 1.05 |

*data given by the manufacturer

The specific surface areas for the unmodified membranes, determined using nitrogen adsorption / BET analysis, were 2.07 $m^2/g$ for 0.45 μm membrane, 1.02 $m^2/g$ for the 1~2 μm membrane and 1.05 $m^2/g$ for the 3~5 μm membrane (**Table 5-2**). The significantly higher specific surface area for the 0.45 μm membrane than for the other two membranes indicated that the pore structure of latter two was indeed dominated by very large macropores (diameter > 1 μm). The permeability correlated well with the pore sizes (**Table 5-2**). The buffer permeability increased with larger mean pore size, but less than expected from standard pore flow model (for example, using Hagen-Poiseuille law equation (2-5) in **Section 2.7.)** as approximation, for membranes with same thickness and porosity, flux of the same fluid at the same trans-membrane pressure is proportional to the pore diameter to the power of 2).

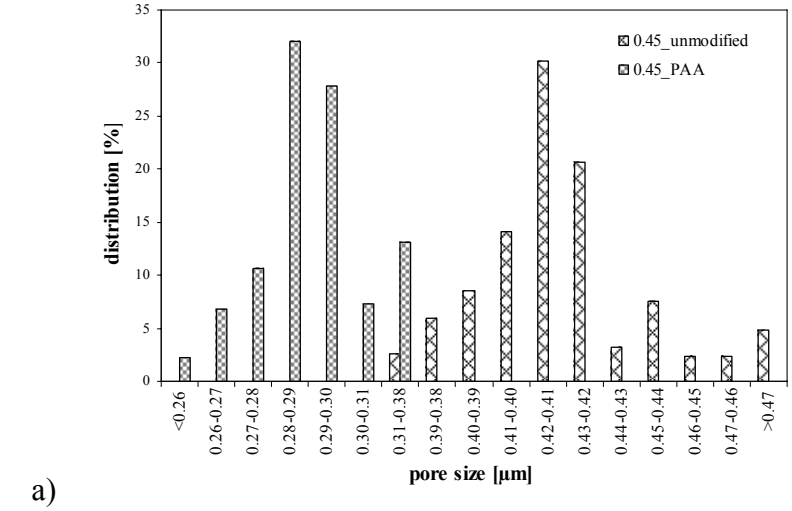


a)

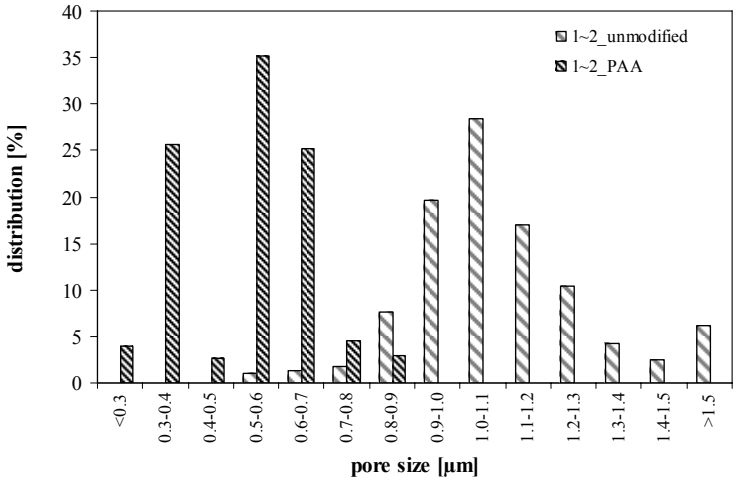


b)

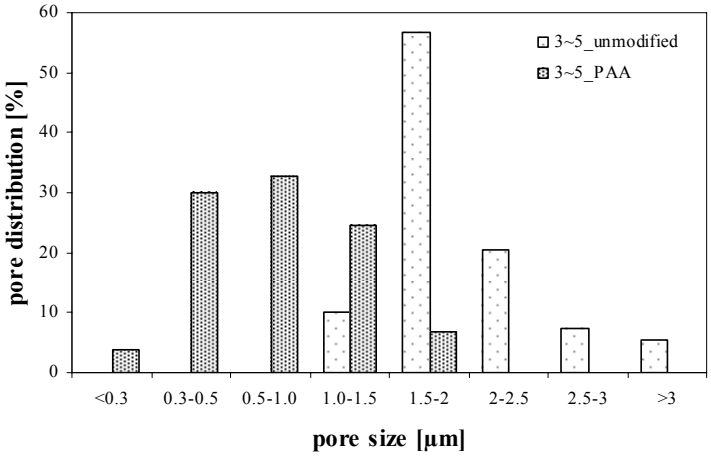


c)

**Figure 5-14.** Pore size distribution from gas flow / liquid dewetting permporometry for original and photo-grafted membranes with poly(acrylic acid): a) 0.45 µm; b) 1~2 µm; c) 3~5 µm.

### 5.2.2. Degree of grafting

The preparation of new membrane adsorber was obtained by precoating of photo initiator BP in non-polar solvent heptane (this non-polar solvent was used for the polar base membrane in order to minimize uptake of photo-initiator in the bulk of the cellulose), followed by subsequent UV initiated hydrogen abstraction reaction to yield polymer radicals on the surface of the membrane in the presence of monomer. The variation of degree of grafting can be obtained by either variation of UV time or concentration of monomers. The total concentration of monomers was kept constant in this work, and UV irradiation time was varied to yield the respective degree of grafting. The influence of UV irradiation time on DG for membranes with different pore sizes was investigated for grafting of AA, at a constant concentration in the reaction mixture (**Figure 5-15a**). As expected, longer irradiation time led to an increase in DG, i.e. the amount of grafted polymer can be adjusted by UV irradiation time.

The pore size distributions of dry membranes significantly changed after grafting of AA. For the 0.45 µm membrane with narrow symmetric pore size distribution, only the mean pore diameter was shifted from 0.42 to 0.30 µm (**Figure 5-14a**). In contrast to the unmodified membrane, a bi-modal pore size distribution with 26% of the pores between 0.3 and 0.4 µm, 60% between 0.5 and 0.7 µm was observed for the grafted 1~2 µm membrane (**Figure 5-14b**). The pore size distribution of the grafted 3~5 µm membrane was much broader compared to the unmodified membrane with most of the pores relatively evenly spread between 0.3 and 1.5 µm (**Figure 5-14c**). The overlap between the pore size distributions of modified and unmodified membranes was much larger for the 0.45 µm membrane than for the 1~2 µm and 3~5 µm membranes. Overall, the shifts of mean pore sizes and pore size distributions indicated successful grafting of the functional cation-exchange polymer to the pore walls in the interior of the membranes.

The effects of grafting on the hydrodynamic properties of the membranes were investigated by determination of the permeability for the 10 mM potassium phosphate buffer, pH 7.0 (buffer A) (**Figure 5-15b**). A systematic decrease of permeability with the irradiation time (and hence DG) was observed. After 4 min, drops of permeability of 98%, 87% and 62% for the 0.45 µm, 1~2 µm and 3~5 µm membranes, respectively were observed. Increase of irradiation time to 15 min resulted in a slight further decrease of permeability for the 0.45 µm and 1~2 µm membranes, while the reduction for the 3~5 µm membrane was significantly larger. **Figure 5-15** reveals the trade-off between DG (and hence thickness of water-swollen

grafted layer) and membrane permeability. The loss of permeability was especially pronounced for the 0.45 µm membrane with the smallest mean pore size. Therefore, the irradiation time for all further grafting functionalizations was set to 4 min for the 0.45 µm membrane, and 8 min for the 1~2 µm and 3~5 µm membranes.

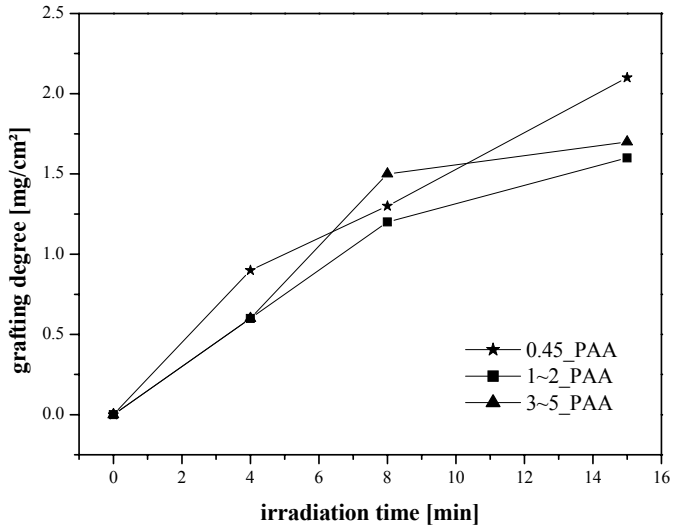


a)

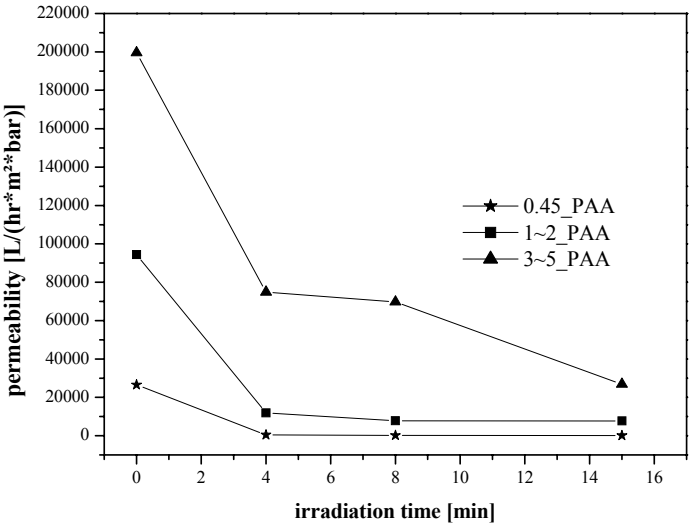


b)

**Figure 5-15.** Influence of UV irradiation time onto, a) DG of membranes grafted with poly(acrylic acid); b) membrane permeability measured with buffer A.

### 5.2.3. Variation of grafted layer structure

All three base membranes with different pore structures had been grafted using three monomer mixtures of same total monomer concentration (cf. **Table 4-2**) leading to different grafted architectures. The DG values obtained with the cross-linker monomer in the reaction mixture (crAA and crAAAm) were consistently larger than for the grafted homopolymer PAA (**Table 5-4**). It is believed, that the second double bond of the cross-linker MBAA can either be incorporated in another growing grafted chain in the boundary layer, or it can react with macro-radicals in solution originating from chain transfer to form a grafted polymer network – both mechanisms will lead to higher amount of surface-bound polymer than in case of grafting homopolymerization (*20, 46*).

The permeability of the membranes with different functional layers was measured using buffer A with a low ionic strength and with 1 M salt concentration to investigate the extension and mobility of the functional chains on the pore surface (**Table 5-3**). Generally, the permeability decreased after grafting. The largest reductions in permeability were found for the grafted linear PAA followed by copolymerization with cross-linker (crAA). The dilution of carboxylic group density in the cross-linked layer by copolymerization with AAm further enhanced this tendency (crAAAm). The changes in permeability from low salt concentration (10 mM potassium phosphate buffer, pH 7.0) to high salt concentration (10 mM potassium phosphate buffer, pH 7.0 plus 1M NaCl) were most pronounced for the grafted homopolymer PAA. The increase in permeability was 6.9 times for the 0.45 µm membrane, 4.4 times for the 1~2 µm membrane and 1.8 times for the 3~5 µm membrane. Grafting of AA copolymers diminished this effect: with cross-linker (crAA), the increase in permeability was 2.0, 1.1 and 1.0 times for the 0.45 µm, 1~2 µm and 3~5 µm membranes, respectively. With cross-linker and the diluent (crAAAm), the increase in permeability was 1.3, 1.2 and 1.1 times for the 0.45 µm, 1~2 µm and 3~5 µm membranes, respectively. Looking at the pore diameters, the smallest changes (close to zero) were observed for the 3~5 µm membrane. In contrast, the flux ratio for the Sartobind C, also based on a 3~5 µm membrane, was 1.8 times (i.e., the same as for the membrane with photo-grafted linear PAA). There was no distinguishable change of permeability for unmodified membranes through the change of salt concentration.

**Table 5-3.** Data overview of the membrane adsorbers measured using SCell module (batch II): grafting conditions, degree of grafting, buffer permeability, ion-exchange capacity and static protein binding capacity

| base membrane | grafting | UV irradiation time [min] | DG [mg/cm²] | permeability [l/(h*m²*bar)] | | ion-exchange capacity | | SBC | | | |
|---|---|---|---|---|---|---|---|---|---|---|---|
| | | | | buffer A | buffer A +1 M NaCl | [µmol/ml membrane] | [µmol/mg gr. polymer] | Lys | | IgG | |
| | | | | | | | | [mg/ml] | [mg/mg gr. polymer] | [mg/ml] | [mg/mg gr. polymer] |
| 0.45 | unmodified | 0 | 0 | 26,590 | 26,200 | n.d. | n.d. | n.d. | n.d. | n.d. | n.d. |
| | PAA | 4 | 0.9 | 450 | 3,090 | 419.3 | 12.1 | 71.4 | 79.3 | 52.3 | 58.1 |
| | crAA | 4 | 1.5 | 7,330 | 15,020 | 707.4 | 8.1 | 69.5 | 46.3 | 46.6 | 31.0 |
| | crAAAm | 4 | 1.0 | 15,670 | 20,800 | 484.0 | 5.6 | 25.8 | 25.8 | 25.3 | 25.3 |
| 1~2 | unmodified | 0 | 0 | 94,400 | 97,280 | n.d. | n.d. | n.d. | n.d. | n.d. | n.d. |
| | PAA | 8 | 1.2 | 7,790 | 33,970 | 456.4 | 13.1 | 62.6 | 52.1 | 66.0 | 55.0 |
| | crAA | 8 | 2.0 | 16,520 | 38,790 | 813.9 | 7.2 | 89.5 | 44.8 | 37.5 | 18.8 |
| | crAAAm | 8 | 1.7 | 54,740 | 66,750 | 467.0 | 4.7 | 35.5 | 20.9 | 33.2 | 19.5 |
| 3~5 | unmodified | 0 | 0 | 199,580 | 191,940 | n.d. | n.d. | n.d. | n.d. | n.d. | n.d. |
| | PAA | 8 | 1.2 | 69,710 | 119,840 | 744.0 | 12.2 | 43.4 | 36.2 | 49.5 | 41.3 |
| | crAA | 8 | 2.1 | 130,870 | 130,730 | 535.9 | 6.2 | 40.3 | 19.2 | 24.6 | 11.7 |
| | crAAAm | 8 | 1.6 | 137,180 | 151,950 | 380.4 | 5.5 | 23.4 | 14.6 | 23.1 | 14.4 |
| | Sartobind C | | | 114,000 | 210,000 | 5.6 | 0.1 | 24.9 | | 11.7 | |
| | Sartobind S | | | 118,000 | 203,000 | 208* | | 46.9 | | 19.5 | |

* measured by the manufacturer using conductometric titration (*58*)

### 5.2.4. Cation-exchange capacity

The ion-exchange capacity of weak cation exchange membranes can be determined statically via titration (*23, 111, 136, 137*) as well as by frontal analysis and elemental analysis for anion exchanger (*111, 138*) or *in situ* under flow-through conditions via the inadvertent pH transient method (*112, 113*).

In the static back-titration method, modified membrane was first protonated by a strong acid, subsequently equilibrated with a known surplus amount of base, and thereafter the titration was performed with this solution. The carboxyl amount from titration was normalized by the respective mass of grafted polymer to eliminate the influence of DG variations. The highest ion-exchange capacities determined by the back-titration method, almost independent of pore size between 12.1 and 13.1 µmol $Na^+$/mg grafted polymer, were observed for the three membranes grafted with the homopolymer PAA (**Table 5-3**). The data were reduced to values between 6.8 and 9.1 µmol/mg as result of copolymerization using the cross-linker MBAA (crAA) and were further reduced to values between 4.7 and 5.6 µmol/mg by addition of the diluent monomer AAm (crAAAm).

*In situ* determination of ion-exchange capacity was performed via detection of the change of pH during step change of ammonium sulphate concentration from 500 M to 20 mM. Typical data are presented for crAA type membranes with different pore sizes (**Figure 5-16a**). The pH increased sharply till to a plateau, then reduced slowly to reach again a constant pH close to the initial value. The slight differences between initial and end values have presumably been caused by the lower real pH value of the 20 mM ammonium sulfate solution in the experiments. The entire process took 240 min for the membranes with the largest pore size (3~5 µm), and 150 min (for 1~2 µm), 180 min (for 0.45 µm) for the other two membranes, all at 5 ml/min.

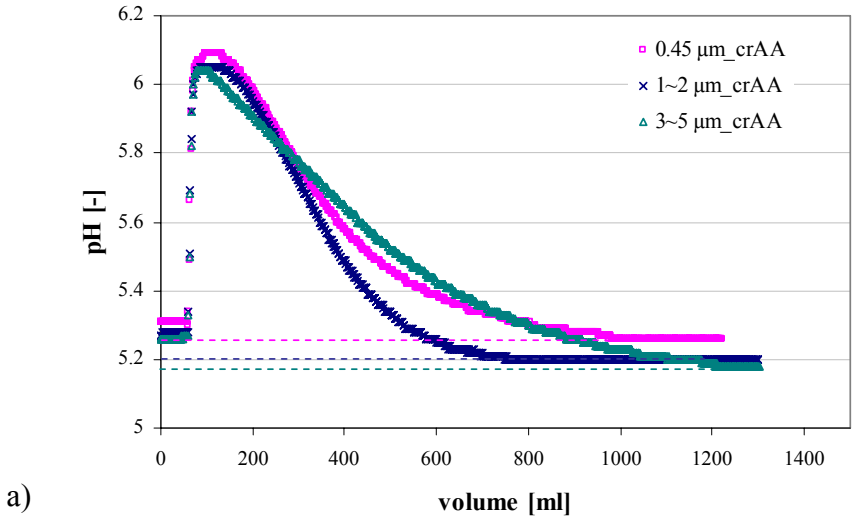


a)

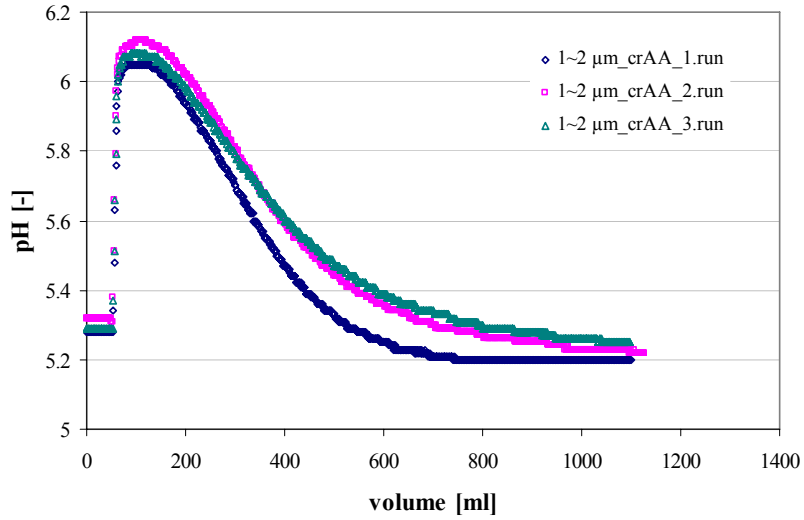


b)

**Figure 5-16.** Ion-exchange capacity measured via pH transient for membranes photo-grafted with a) cross-linked poly(acrylic acid) during the step change from high (0.5 M ammonium sulfate solution, pH 5.3) to low (20 mM ammonium sulfate solution, pH 5.3) concentration solution with 5 sheets of membrane stacked in CIM membrane module at a flow rate of 5 ml/min. Dotted lines are base lines used for peak area calculation. The absorbance was measured at 210 nm; b) Repeatability of 1~2 µm membranes grafted with crAA structure.

The area under the curve has then been used as measure of inadvertent pH transient capacity. The resulting data for the membranes were listed in **Table 5-4**. Considering the influence of DG, the area values were divided by DG. For membranes with the same pore size, PAA type showed the highest value of ion exchange capacity. The membranes with the same grafting structure had similar values, except for 0.45_PAA, and with less dependence of pore size. Repeatability of pH transient has been tested for 1~2-crAA membrane (**Figure 5-16b**). The area deviation was within 9%.

**Table 5-4.** Ion exchange capacity measured via pH transient

| pore size [µm] | grafting layer | DG [mg/cm²] | pH transient area [mAu*ml-buffer] | pH transient area/DG $\frac{mAu*ml\_buffer}{mg*ml^{-1}\_mem}$ |
|---|---|---|---|---|
| 0.45 | PAA | 0.7 | 316 | 10.7 |
| | crAA | 1.7 | 345 | 4.7 |
| | crAAAm | 1.8 | 273 | 3.5 |
| 1~2 | PAA | 1.3 | 351 | 6.2 |
| | crAA | 1.9 | 335 | 4.1 |
| | crAAAm | 2.3 | 339 | 3.4 |
| 3~5 | PAA | 1.4 | 387 | 6.4 |
| | crAA | 1.8 | 440 | 5.6 |
| | crAAAm | 1.9 | 338 | 4.1 |

### 5.2.5. Equilibrium behavior and static binding capacity

The static binding capacity of functionalized membranes was measured for two model proteins. Lysozyme with molecular weight of 14.3 kg/mol and isoelectric point pI ~11.3, and IgG with molecular weight of 160 kg/mol and the pI ~6.0 (**Table 5-3**).

The binding isotherms are presented in **Figure 5-17** for Lys to 0.45 µm membranes (**Figure 5-17a**) and to 3~5 µm membrane (**Figure 5-17b**) with different grafted copolymers.

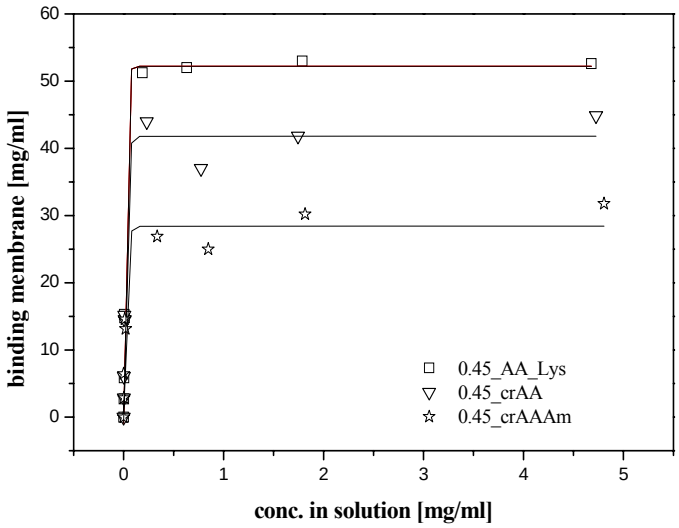


a)

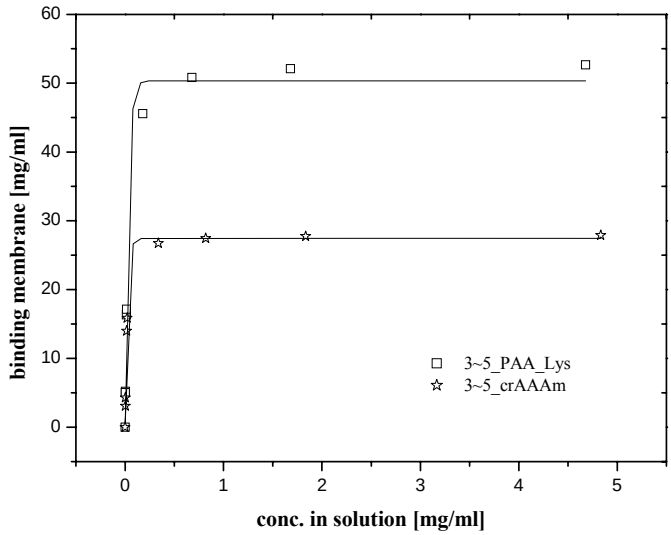


b)

**Figure 5-17.** Binding isotherm at pH 7, measured by batch incubation for a) functionalized 0.45 µm; b) 3~5 µm membranes using lysozyme. Solid lines are for experimental data fitted to Langmuir isotherm by non-linear least-square regression.

In the low Lys concentration range of lower than 0.5 mg/ml, the slope of the curves was very steep, indicating a high binding affinity of Lys to the ion-exchange membranes. The results from curve fitting yielded similar Langmuir equilibrium constants (~55 ml/mg or $7.87*10^5$ L/mol) for the three membranes with different grafted copolymer architectures. However, the

maximum binding capacities were different, i.e. 52, 42 and 28 mg/ml for 0.45_AA, 0.45_crAA and 0.45_crAAAm, respectively. The binding isotherms for Lys were similar for the other pore sizes, for instance, 3~5 µm membrane, however with different maximal binding capacities. The isotherm slope of 0.45_crAAAm in small concentration range was much less steep for IgG ( **Figure 5-18**) than for Lys. The Langmuir constant for 0.45_crAAAm using IgG was 10 ml/mg (or $1.60*10^6$ L/mol). Although the maximum capacity (33 mg/ml) was somewhat lower than obtained for Lys, its molecular affinity for IgG is higher than Lys.

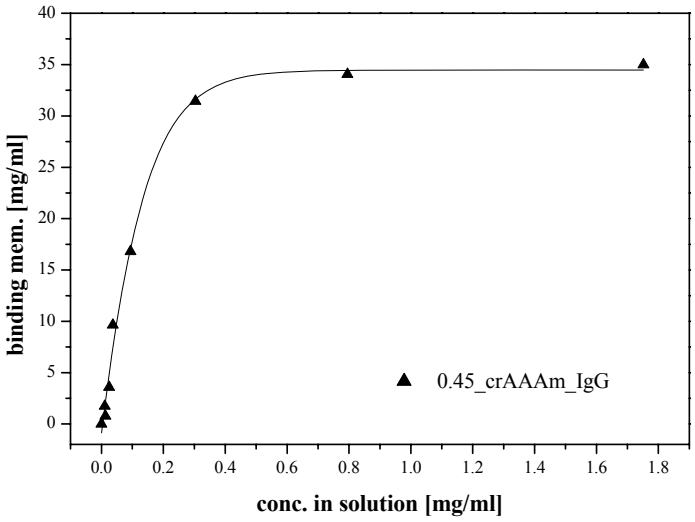


**Figure 5-18.** Binding isotherm at pH 7, measured by batch incubation for functionalized 0.45 µm membranes for IgG. Solid lines are for experimental data fitted to Langmuir isotherm by non-linear least-square regression.

An overview of static and dynamic binding capacity measured using Scell module is given in **Tables 5-3** and **5-6**. Highest SBCs were 89.5 mg/ml Lys (for 1~2_crAA) and 66.0 mg/ml for IgG (for 1~2_PAA) per ml membrane. SBC was also normalized by the respective mass of grafted polymer and expressed as mg protein per mg grafted polymer. The normalized SBC indicated significant dependence on pore sizes of base membrane and architecture of the functional layers. The normalized values significantly decreased with increasing pore size. For the same membrane type, the normalized SBC decreased after introduction of the cross-linked layer (crAA) and the diluent (crAAAm). The SBC for Lys was significantly larger than for IgG in the case of crAA membranes. The SBC of both proteins was in the same range for crAAAm membranes.

### 5.2.6. Breakthrough curve and dispersion property

Most of BTCs and SDCs for porous membranes were found to be sigmoidal (*33, 116*) However, the curves measured using SCell module were more symmetric in shape than those obtained with CIM® module (**Section 5.3.**), indicating a strong dependence of the flow distribution in membrane modules. Data presented here were only for SCell module. In order to allow a quantitative comparison of all data, the slope values of BTC per layer of membranes in the stack was estimated by linear regression of the data between 20% and 70% breakthrough (**Table 5-5**).

**Table 5-5.** Data overview of the membrane adsorbers: slopes of the breakthrough curves (measured using Scell module,where 3 pieces of membrane were stacked in the membrane module)

| base membrane pore size [µm] | grafting | BTC_Lys slope/layer at flow rate [ml/min] | | BTC_IgG slope/layer at flow rate [ml/min] | |
|---|---|---|---|---|---|
| | | 1 | 10 | 1 | 10 |
| 0.45 | PAA | n.d. | n.d. | n.d. | n.d. |
| | crAAAm | 2.8 | 2.6 | 2.6 | 3.8 |
| 1~2 | PAA | 0.8 | 0.9 | 1.3 | 1.4 |
| | crAAAm | 7.6 | 4.8 | 5.5 | 10.7 |
| 3~5 | PAA | 1.8 | 1.8 | 2.9 | 2.9 |
| | crAAAm | 9.5 | 7.7 | 10.6 | 7.1 |
| | Sartobind C | 7.7 | 4.1 | 10.5 | 11.7 |
| | Sartobind S | 5.0 | 4.3 | 9.3 | 8.6 |

For the curves for 3~5 µm membranes bound with Lys at 1 ml/min (**Figure 5-19a**), the approach towards saturation indicates significantly discrimination. 3~5_crAAAm membrane was similar to Sartobind C, while the slope for membrane 3~5_PAA was much lower. An increase of flowrate from 1 to 10 ml/min reduced the sharpness of BTCs. Notable earlier breakthrough took place for Sartobind C leading to the small value of 10% DBC (similar for IgG; cf. **Figure 5-20**). Sartobind S exhibited high binding capacity to Lys, its BTC preformed in the similar manner as the BTC for 3~5_crAAAm membrane (**Figure 5-19**), but the progress towards saturation, as judged from the transition between linear and plateau of

breakthrough curves, was much slower than for 3~5_crAAAm membrane at 10 ml/min (**Figure 5-19b**). The advantage of high binding capacity of Sartobind S as shown for Lys was diminished when it was used for IgG (molecular weight is 10 fold larger than Lys). Its breakthrough occurred much earlier than for membranes 3~5_AA and 3~5_crAAAm (**Figure 5-20**). The slope values for PAA membrane seemed to be independent of flow rate (**Table 5-5**), however, the proceeding towards saturation (between 90~100% breakthrough) was reduced as the flow rate increased. It is particularly significant for the BTCs using IgG (**Figure 5-20**). The saturation speed differed notably from 70% breakthrough. Increasing flow rate reduced the slope value, i.e. the sharpness of BTCs for membrane 3~5_crAAAm and Sartobind S, except for Sartobind C (slope value increased from 10.5 to 11.7 for IgG). Sartobind C presented pronounced earlier breakthrough for IgG and strong dependence of elevated flow rates for Lys (**Figures 5-19** and **5-20**).

The breakthrough curves recorded for 1~2 µm membranes at 10 ml/min are shown for Lys in **Figure 5-21a** and for IgG in **Figure 5-21b**. While the shape of breakthrough curves for 1~2_crAAAm kept almost unchanged with Lys and IgG, the breakthrough of curve for 1~2_AA occurred apparently earlier for Lys at 10 ml/min (**Figure 5-21a**) indicating high dependence of flowrate for Lys, but this effect was smaller for IgG. It is the same case with 0.45_crAAAm membrane (**Figure 5-22**). The small inset in **Figure 5-22** presents the breakthrough of 0.45_crAAAm membranes for Lys and IgG at low (1 ml/min) and high flowrate (10 ml/min). In contrast to the medium and large pore membranes, although the 0.45 µm membrane presented higher values of max.DBC (**Table 5-8**), the slope values were in the same level as that for linear grafted 3~5 µm membranes. Breakthrough took place within ~3.5 ml of feed volume, particularly pronounced for Lys. Generally, the slope values of crAAAm membranes were observed larger than that of PAA membranes. Cross-linker grafted crAAAm membranes and protein with bigger molecular weight such as IgG leads to sharper breakthrough curves.

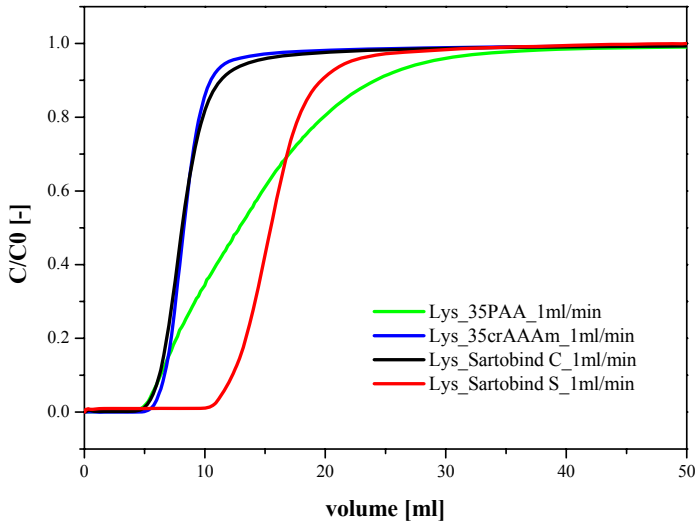


a)

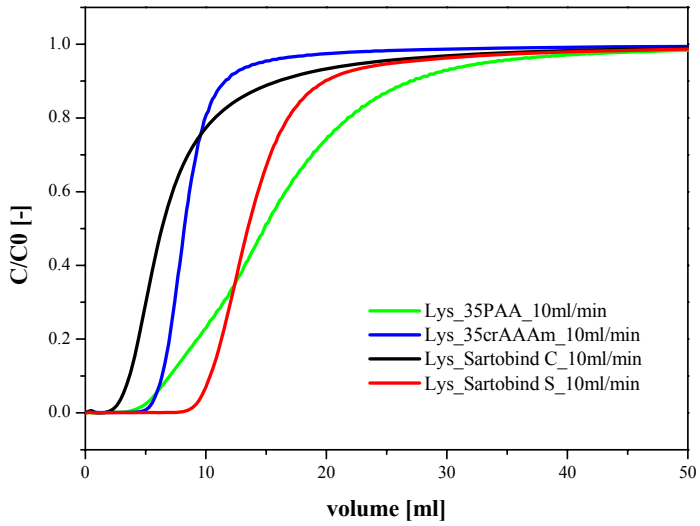


b)

**Figure 5-19.** Breakthrough curves for lysozyme with functionalized 3~5 µm membranes at: a) 1 ml/min, b) 10 ml/min. 3 membranes were stacked in Scell module.

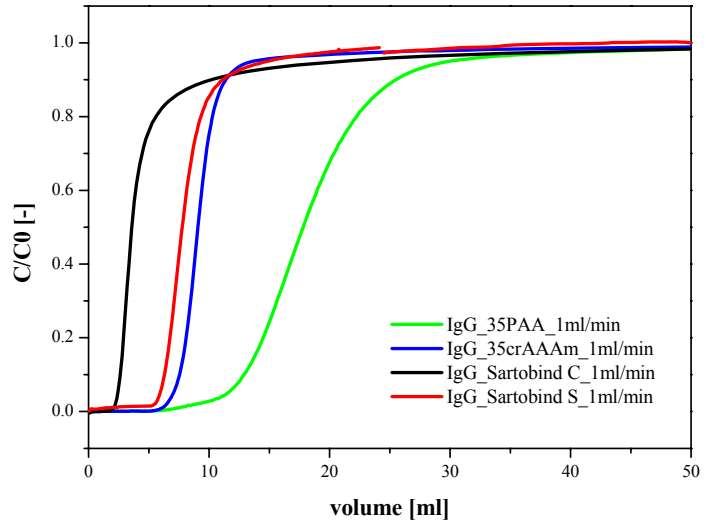


a)

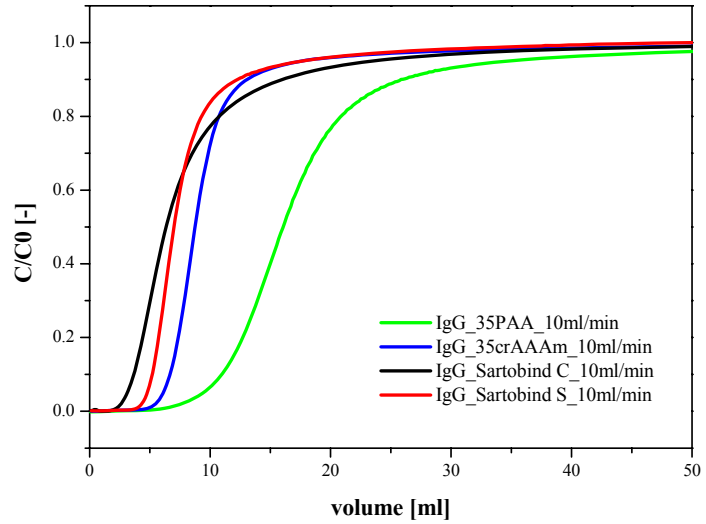


b)

**Figure 5-20.** Breakthrough curves for IgG with functionalized 3~5 µm membranes at: a) 1 ml/min; b) 10 ml/min. 3 membranes were stacked in SCell module.

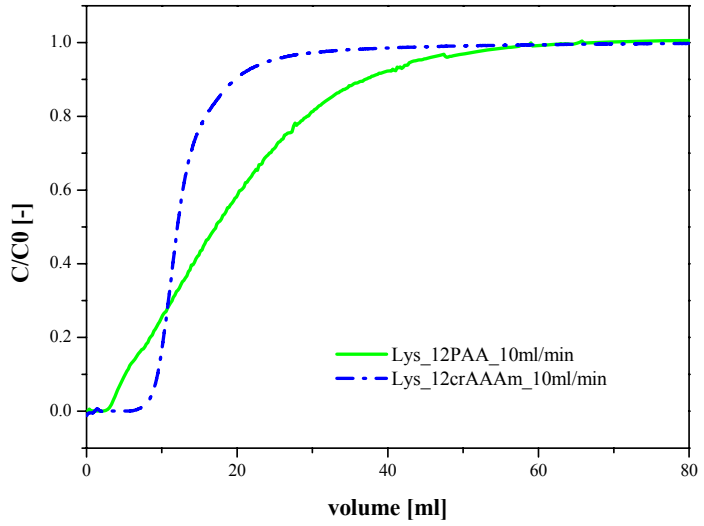


a)

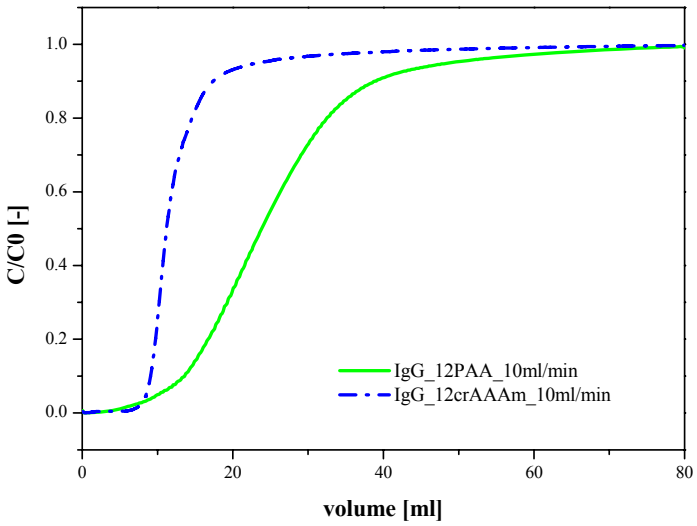


b)

**Figure 5-21.** Breakthrough curves for Lys with functionalized 1~2 µm membranes at 10 ml/min. 3 membranes were stacked in CIM module.

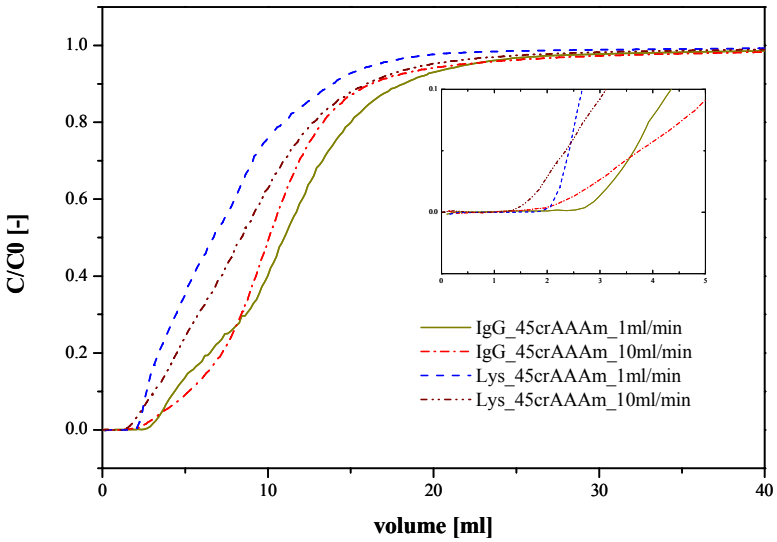


**Figure 5-22.** Breakthrough curves for Lys and IgG with functionalized 0.45 µm membranes. 3 membranes were stacked in CIM module. Left window: 10% breakthrough of 0.45 µm membranes.

### 5.2.7. Dynamic binding capacity

The onset of the breakthrough curve ("10% DBC") is a measure of dynamic binding capacity and efficiency of an adsorber with respect to a minimum loss of unbound solute in flow-through mode. From the complete BTC additional information about the maximum dynamic binding capacity ("max DBC") was retrieved (cf. **Section 4.2.5.2.**).

The results of max DBC and 10% DBC of the functionalized membranes are summarized in **Table 5-6**. The recovery in all dynamic experiments was over 95% (**Table 5-7**). Membrane 1~2_PAA yielded the highest max DBC for both proteins (73.1 mg/ml for Lys, and 77.5 mg/ml for IgG) at low flow rate of 1 ml/min. The highest values for 10% DBC were obtained for membrane 1~2_PAA (23.9 mg/ml for Lys, 37.2 mg/ml for IgG). The max DBC was in the same range as (or even larger than) SBC. For IgG the max DBC was even larger than the SBC. It must be mentioned that the value of SBC was converted from the eluted amount of protein from the functional membranes. The surplus of weakly bound protein had been washed away before elution, while the DBC were calculated from the difference between SDC and BTC without washing in the BTC curve experiment (cf. **Section 4.2.5.2.**).

**Table 5-6.** Dynamic binding capacity (max DBC and 10% DBC) of the membrane adsorbers measured using SCell module (batch II) for Lys and IgG at the flow rates of 1 and 10 ml/min

| base membrane pore size [µm] | grafting | DBC_Lys [mg/ml] | | | | DBC_IgG [mg/ml] | | | |
|---|---|---|---|---|---|---|---|---|---|
| | | max DBC at flow rate [ml/min] | | 10% DBC at flow rate [ml/min] | | max DBC at flow rate [ml/min] | | 10% DBC at flow rate [ml/min] | |
| | | 1 | 10 | 1 | 10 | 1 | 10 | 1 | 10 |
| 1~2 | PAA | 73.1 | 59.4 | 23.9 | 11.5 | 77.5 | 74.2 | 37.2 | 36.6 |
| | crAAAm | 33.3 | 38.1 | 23.0 | 24.5 | 35.7 | 35.9 | 26.9 | 23.3 |
| 3~5 | PAA | 40.5 | 47.0 | 15.1 | 17.1 | 54.6 | 51.8 | 34.6 | 28.9 |
| | crAAAm | 23.9 | 24.2 | 16.2 | 15.1 | 27.0 | 27.1 | 18.8 | 16.2 |
| | Sartobind C | 24.2 | 23.3 | 15.1 | 7.4 | 15.6 | 10.1 | 4.4 | 0.9 |
| | Sartobind S | 44.9 | 44.4 | 33.4 | 30.1 | 22.5 | 21.9 | 15.4 | 12.3 |

**Table 5-7.** Recovery of dynamic experiments using SCell module for batch II

| base membrane pore size [µm] | grafting | recovery_Lys [%] at flow rate [ml/min] | | recovery_IgG [%] at flow rate [ml/min] | |
|---|---|---|---|---|---|
| | | 1 | 10 | 1 | 10 |
| 1~2 | PAA | 95 | 97 | 99 | 95 |
| | crAAAm | 101 | 99 | 98 | 96 |
| 3~5 | PAA | 94 | 105 | 99 | 97 |
| | crAAAm | 95 | 102 | 106 | 99 |
| | Sartobind C | 96 | 99 | 98 | 96 |
| | Sartobind S | 101 | 97 | 97 | 97 |

The dynamic binding capacity values changed with varied functional architecture and pore size of base membranes. Grafting with cross-linker and introduction of spacers leads to reductions of dynamic binding capacity for both proteins to about 50%. However, variation of flow rate showed less impact on the dynamic performance, except for 1~2_PAA and Sartobind C membranes. For membranes prepared using the same functionalization conditions (cf. **Section 4.3.),** 1~2 µm membrane achieved commonly higher dynamic binding capacity (max DBC and 10% DBC) than 3~5 µm membrane. In contrast to Sartobind membranes, the dynamic binding capacity of new prepared membranes showed similar level with IgG as Lys. For Sartobind membranes, binding with larger proteins such as IgG leaded to pronounced reduction of binding capacity under dynamic conditions (**Table 5-6**).

The reusability of modified membranes was tested using 1~2_crAAAm for IgG. After regeneration using 0.1 M NaOH (20 ml), the determination of dynamic capacity was repeated at 10 ml/min for 3 times. No significant changes were found for max DBC as well as 10% DBC.

As the permeability of 0.45 µm membrane was strongly restricted by its pore sizes as shown in **Figure 5-15b**, it reveals that the base membrane with the pore size of 0.45 µm is not suitable for grafting of AA functional layer and hence will not be discussed further. The ratio of SBC for IgG to SBC for Lys of crAA membranes was significant smaller than for AA and crAAAm type (see also **Section 5.2.5.**), revealing undesirable size exclusion effects in the grafted functional layer. Consequently, further analysis of the binding performance covers only the 1~2 mm and 3~5 µm membranes in combination with PAA and crAAAm grafting architectures. The dynamic performance of membranes are compared in terms of utilization of the membrane binding capacity under dynamic conditions at 10 ml/min (10% DBC vs. max DBC), and the influences of the protein size, flow rate (1 ml/min vs. 10 ml/min) as well as architecture of functional layers (AA vs. crAAAm) on the membrane binding performance. The results are summarized in **Table 5-8**.

**Table 5-8.** Dynamic performance of membrane adsorbers, measured using SCell module (batch II): utilization of binding capacity, effects of protein size and flow rate.

| base membrane pore size [μm] | grafting | utilization of binding capacity (max DBC vs. SBC) [%] | | utilization of binding capacity (10% DBC vs. max DBC) [%] | | effect of protein size (IgG vs. Lys) [%] | | effect of flow rate 10% DBC (10 vs. 1 ml/min) [%] | |
|---|---|---|---|---|---|---|---|---|---|
| | | Lys | IgG | Lys | IgG | 10% DBC | Max DBC | Lys | IgG |
| 1~2 | PAA | 95 | 112 | 19 | 49 | 318 | 125 | 48 | 98 |
| | crAAAm | 107 | 108 | 64 | 65 | 95 | 94 | 107 | 87 |
| 3~5 | PAA | 108 | 105 | 36 | 56 | 169 | 110 | 113 | 84 |
| | crAAAm | 103 | 86 | 62 | 60 | 107 | 112 | 93 | 86 |
| | Sartobind C | 94 | 86 | 32 | 9 | 12 | 43 | 49 | 20 |
| | Sartobind S | 95 | 112 | 66 | 56 | 37 | 52 | 90 | 72 |

#### 5.2.7.1. Utilization of the membrane binding capacity under dynamic conditions

The utilization of membrane binding capacity under dynamic binding conditions expressed as a ratio of 10% DBC vs. max DBC at 10 ml/min is depicted in **Table 5-8**. Membranes with linear grafted PAA show lower utilization of the binding capacity than the crAAAm membranes. This effect is especially pronounced for the smaller protein Lys (19% for membrane 1~2_PAA). The utilization of the photo-grafted membrane binding capacity seems to be unaffected for the larger protein IgG. In strong contrast, value of Sartobind C is significantly low. The utilization for IgG was only 9%.

#### 5.2.7.2. Influence of the protein size

The influence of molecular weight of protein was interpreted by the ratio of binding capacity of IgG to Lys (**Table 5-6**). The max DBC value is comparable for IgG and Lys for the PAA and crAAAm membranes. However, the 10% DBC ratios are considerably higher for PAA membranes (169~318%) than for crAAAm which is in accordance with the low utilization of the membrane capacity for Lys (cf. **Table 5-6**). In contrast, the effect of the protein size is considerable large for Sartobind membranes. The ratio for 10% DBC was 12% and 37% for Sartobind C and S, respectively.

#### 5.2.7.3. Influence of the flow rate

Negligible effect of the flow rate on the max DBC values was observed for new prepared crAAAm membranes. A susceptibility of 10% DBC to flow rate was pronounced only for 1~2_PAA membranes and binding of Lys. The breakthrough curves recorded for membranes 3~5_PAA and 3~5_crAAAm at 1 and 10 ml/min for Lys and IgG are shown in **Figures 5-19** and **5-20**, respectively. The shape of the BTC reflects well the utilization of the membrane binding capacity (**Section 5.2.6.**) It is also obviously that elevated flow rates could strongly impact the performance of Sartobind C membranes. And this effect was further enhanced, when it was bound with large protein IgG. The ratio of 10% DBC at 10 ml/min vs. at 1 ml/min was only 20% for IgG (**Table 5-8**).

### 5.2.8. Static visualization of protein binding to modified membranes by CLSM

The CLSM images of protein binding to functionalized cation exchanger membrane adsorbers crAAAm with different pore sizes at similar depths (cf. **Section 4.2.2.3.**) are presented in **Figure 5-23**. The binding pattern of membrane 3~5_crAAAm was similar to that of Sartobind® S (**Figure 5-8**). The functionalization process did not change the morphology of membrane pores (cf. Appendix **Figures 8-2 and 8-3**). The overlap of the images for bound protein to that of the membrane matrix indicated that the protein binding proceeds in a layer anchored to the cellulose network, especially on the pore walls, and barely directly on the thick cellulose. Hence, the protein filled in a relatively thick layer a significant fraction of the macropores, leaving the interior of these pores empty (**Figure 5-23a**). The macrostructure of the membrane 1~2_crAAAm looks more compact with a uniform protein distribution with more finely dispersed macropores. The overlap of images confirmed the above described binding pattern, in particular that the functional layer was only grafted to the pore walls of the membrane adsorber and not inside the cellulose fibers (**Figure 5-23b**). The porous structure image of the 0.45 µm membrane was much more fine and regular (**Figure 5-23c**). No significant difference of binding patterns could be identified for membranes with different grafted layers, for instance for the 3~5 µm membranes in **Figure 5-24**. It illustrates the overlapped images of labeled protein binding to stained membranes. Similar to Sartobind membrane, effective visible depth was approx. 20 µm as demonstrated by the 3D images in **Figure 5-25** for stained membrane (**Figure 5-25a**) and labeled protein (**Figure 5-25b**) of 3~5_crAAAm membrane.

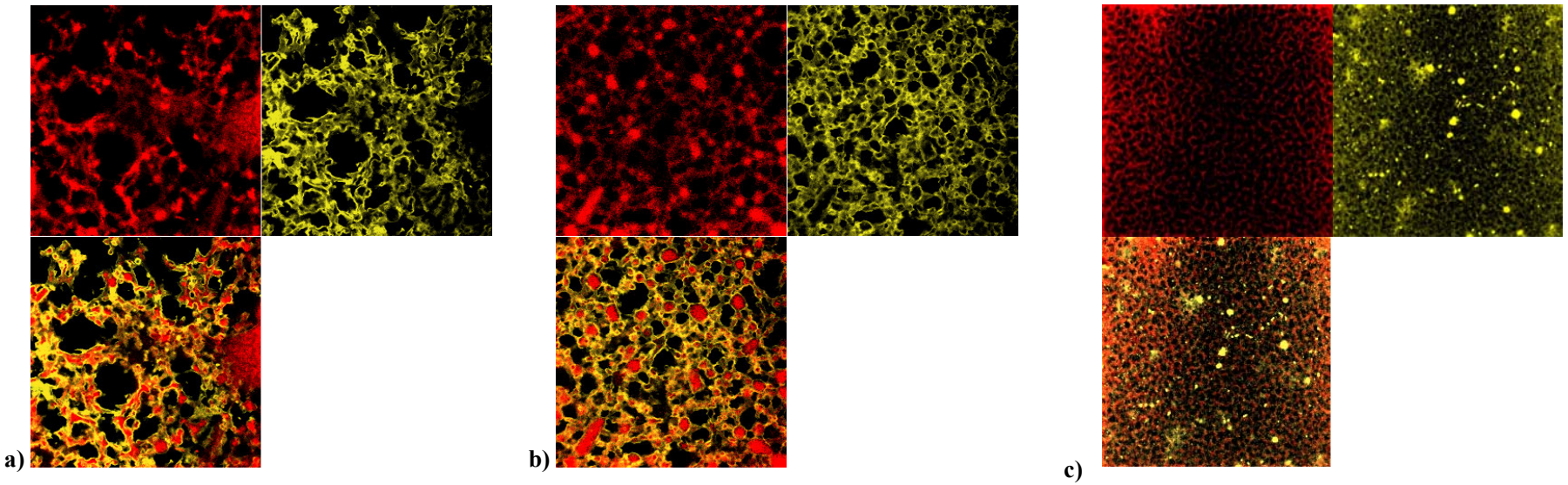


**Figure 5-23.** CLSM images of membrane adsorbers functionalized with crAAAm. Upper left: stained membrane (488 nm); upper right: bound Lys (633 nm) after 2 h incubation with labeled Lys (0.4 mg/ml, pH 7.0); down left: overlap of labeled protein binding to stained membrane. The images, 92.1* 92.1 µm$^2$, were taken for: a) membrane 3~5_crAAAm, 10 µm depth; b) membrane 1~2_crAAAm, 8 µm depth; c) membrane 0.45_crAAAm, 7 µm depth; from the outer surface of the bottom side of membranes.

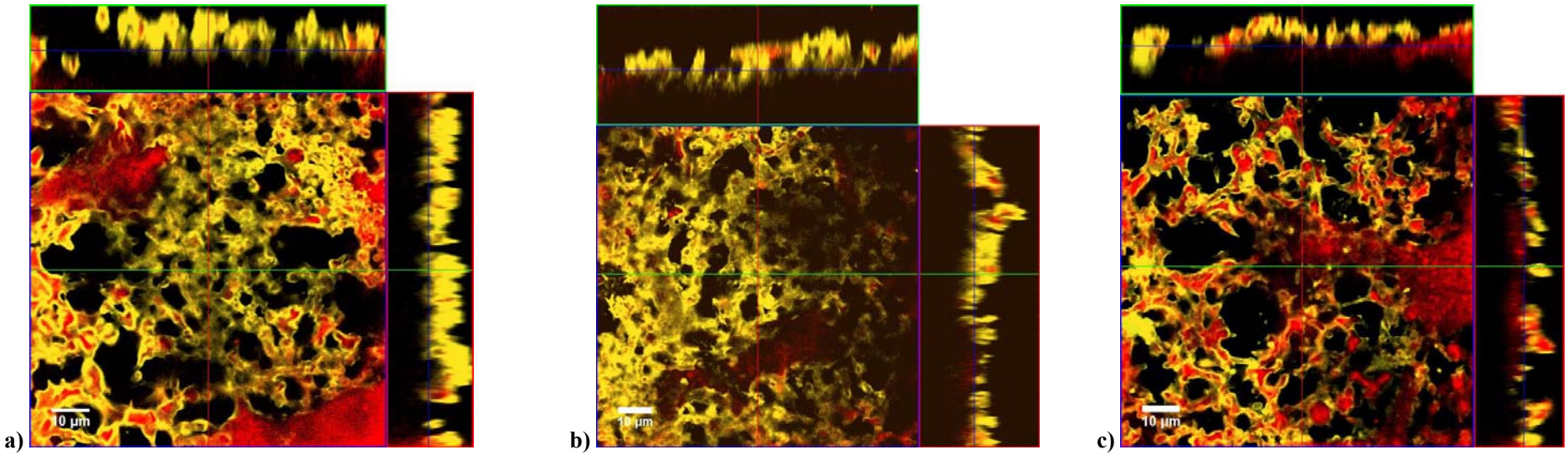


**Figure 5-24.** CLSM images of the membrane adsorbers with different functionalization layers. The images were overlap of labeled protein binding to stained membrane. a) 35_PAA, 11 µm depth; b) 3~5_crAA, 18 µm depth; c) 3~5_crAAAm, 10 µm depth. Dimension of the image area was 92.1* 92.1 $\mu m^2$.

a)

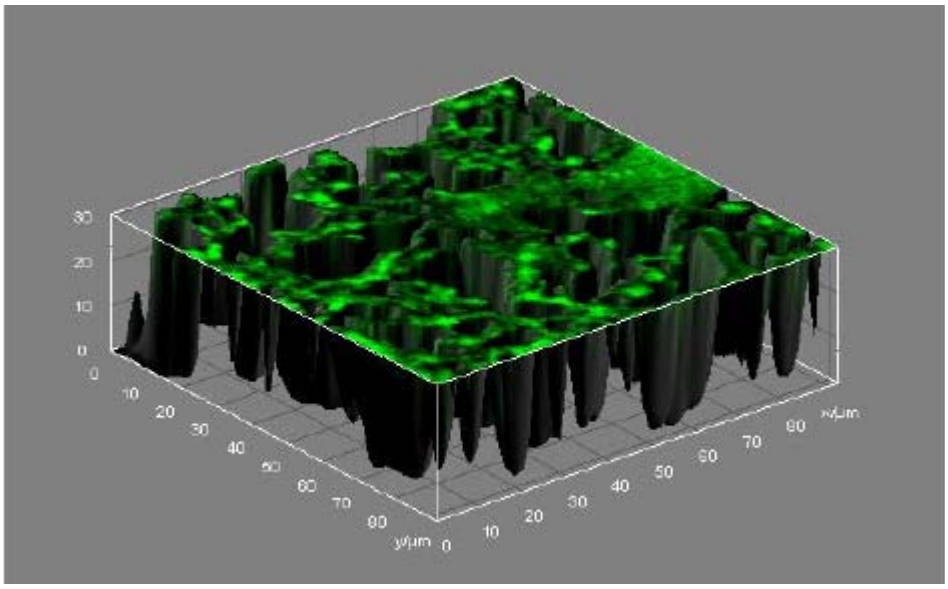


b)

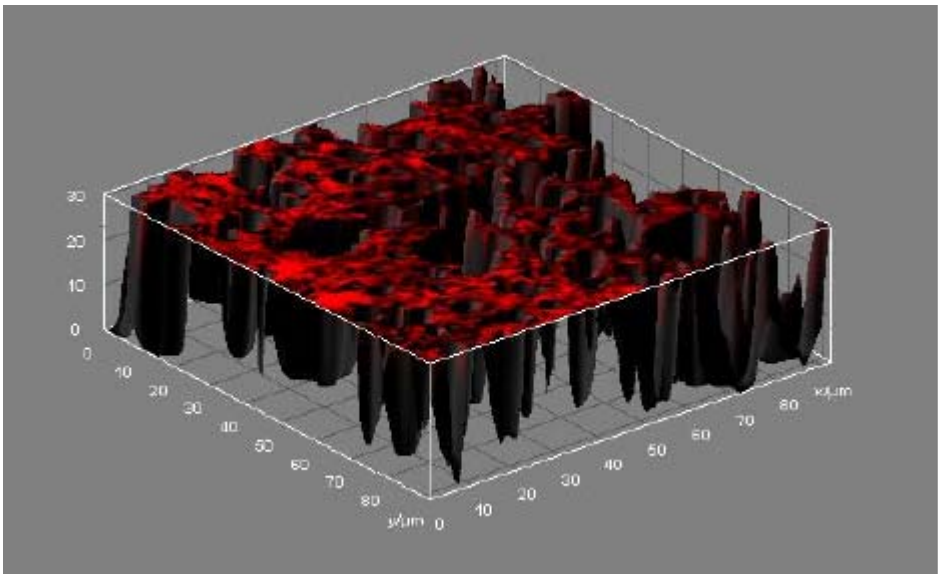


**Figure 5-25.** 3D CLSM images of 3~5-crAAAm, a) DTAF stained membrane (488 nm); b) Cy5 labelled Lys (633nm).

0.45 µm membrane could be strongly stained with the fluorescence dye due to the higher specific surface area. With the exception of some agglomerates (cf. **Figure 5-23c**), the distribution of protein was relatively uniform as the morphology of the stained membrane. The darkness in the middle part was probably caused by the unevenness of the membrane. A mixture of labeled and unlabelled protein had been used here, but indications of affinity discrimination between labeled and unlabeled Lys (*130*) were not observed. Also, the used ratio of labeled vs. native protein (0.83) was higher than that used in other literatures which tried to avoid fluorescence quenching (*99, 130*). The apparent agglomerates of bound protein

could be caused by high local binding capacities, presumably created by high local degree of functionalization. However, it should be kept in mind that the pore size of 0.45 µm base membrane was just around the limit range of 3 D resolution of the method (about 1 $\mu m^3$; cf. **section 6.1.3.).**

All presented results are for the "bottom" sides of the membranes, because this surface and the layer underneath are more uniform and less porous than the "top" sides, and consequently there is a larger fraction of area for protein binding per image. However, analogous results with respect to correlations between pore morphology and protein binding have been obtained for the "top" sides as well (**Figure 8-4**).

## 5.3. Efficiency comparison of membrane modules

### 5.3.1. Performance of dynamic binding capacity in different membrane modules

The dynamic data measured using SCell module has been presented in **Section 5.2**. for batch II membranes. In this part, the data are compared with those measured using CIM module for batch I membranes in order to investigate the influence of membrane modules. **Figure 5-26** illustrates the BTCs of 3~5 µm membranes with Lys measured using CIM module. The breakthrough curve shapes of both studied modules are to some extend sigmoid. When compared with the BTCs measured with SCell module (**Figure 5-19**), obviously earlier breakthrough of curves was observed for the CIM module. The slope values of BTCs using CIM module (**Table 5-9)** was commonly larger than that measured using SCell module (cf. **Table 5-5**). Determination using CIM module leads to higher values of BTC slopes, and thus steeper BTCs than using Sartorius cell.

**Table 5-9.** Data overview of the membrane adsorbers measured using CIM module (Batch I): slopes of the breakthrough curves

| base membrane pore size [µm] | grafting | layers per stack for BTC | BTC_Lys slope/layers at flow rate [ml/min] | | BTC_IgG slope/layers at flow rate [ml/min] | |
|---|---|---|---|---|---|---|
| | | | 1 | 10 | 1 | 10 |
| 0.45 | PAA | n.d. | n.d. | n.d. | n.d. | n.d. |
| | crAAAm | 3 | 26.9 | 27.6 | 15 | 21.5 |
| 1~2 | PAA | 3 | 8.8 | 9.2 | 7.2 | 8.7 |
| | crAAAm | 3 | 9.4 | 13.7 | 8.9 | 10.6 |
| 3~5 | PAA | 5 | 4.6 | 6.1 | 3.5 | 4.1 |
| | crAAAm | 5 | 8.2 | 10.9 | 4.9 | 5.6 |
| | Sartobind C | 5 | 9.5 | 14.8 | 9.5 | 19.3 |
| | Sartobind S | 5 | 8.0 | 8.9 | 11.4 | 11.4 |

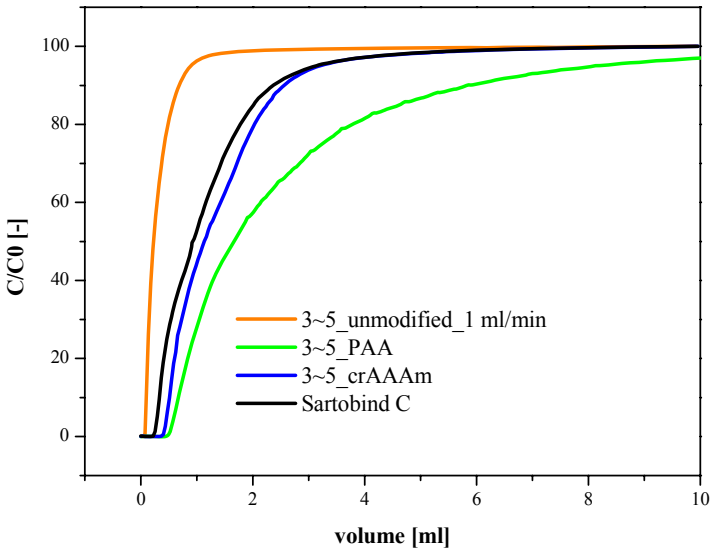


a)

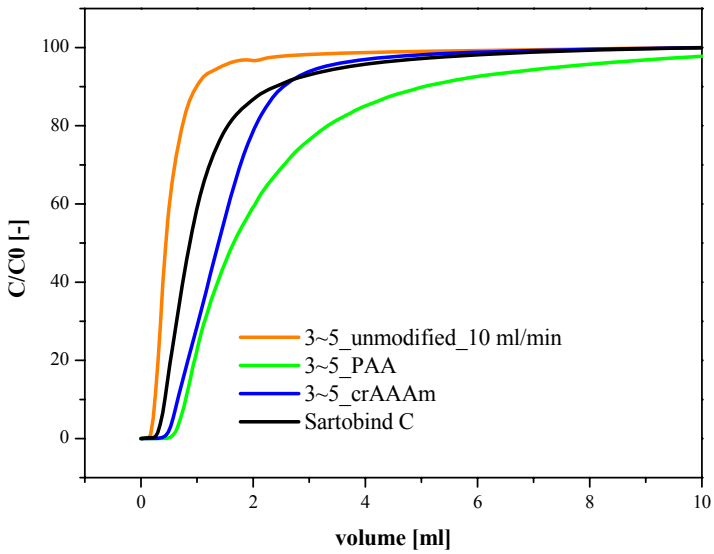


b)

**Figure 5-26.** Breakthrough curves for lysozyme with functionalized 3~5 µm membranes at: a) 1 ml/min, b) 10 ml/min. 5 membranes were stacked in CIM module.

**Table 5-10.** Static and dynamic binding capacity of membrane adsorbers measured using CIM module (Batch I). Dynamic binding capacity (max DBC and 10% DBC) of the membrane adsorbers was measured for Lys and IgG at the flow rates of 1 and 10 ml/min.

| base membrane pore size [µm] | grafting | DG [mg/cm²] | SBC_Lys [mg/ml] | DBC_Lys [mg/ml] | | | | SBC_IgG [mg/ml] | DBC_IgG [mg/ml] | | | |
|---|---|---|---|---|---|---|---|---|---|---|---|---|
| | | | | max DBC at flow rate [ml/min] | | 10% DBC at flow rate [ml/min] | | | max DBC at flow rate [ml/min] | | 10% DBC at flow rate [ml/min] | |
| | | | | 1 | 10 | 1 | 10 | | 1 | 10 | 1 | 10 |
| 1~2 | PAA | 1.2 | 88 | 53 | 46.7 | 8.7 | 12.5 | 90.7 | 69.9 | 62.0 | 23.2 | 15.6 |
| | crAAAm | 1.6 | 46.6 | 37.4 | 33.1 | 8.7 | 12.5 | 31.9 | 36.1 | 34.8 | 8.7 | 6.4 |
| 3~5 | PAA | 1.5 | 55.4 | 36.8 | 33.9 | 5.2 | 7.7 | 44.5 | 32 | 27.3 | 4.0 | 5.6 |
| | crAAAm | 1.8 | 27.1 | 18.7 | 18.9 | 3.9 | 4.2 | 23.2 | 20.0 | 18.5 | 4.0 | 3.2 |
| | Sartobind C | n.d. | 24.9 | 16.8 | 13.7 | 0.1 | 0.7 | 11.8 | 7.4 | 2.4 | 0.4 | 0.1 |
| | Sartobind S | n.d. | 46.9 | 36.7 | 34.1 | 7.0 | 6.5 | 19.5 | 15 | 14.2 | 5.4 | 5.4 |

**Table 5-11.** Dynamic performance of membrane adsorbers measured using CIM module (Batch I): utilization of binding capacity, effects of protein size and flow rate.

| base membrane pore size [µm] | grafting | utilization of binding capacity (max.DBC vs. SBC) [%] | | utilization of binding capacity (10% DBC vs. max DBC) [%] | | effect of protein size (IgG vs. Lys) [%] | | effect of flow rate 10% DBC (10 vs. 1 ml/min) [%] | |
|---|---|---|---|---|---|---|---|---|---|
| | | Lys | IgG | Lys | IgG | 10% DBC | max DBC | Lys | IgG |
| 1~2 | PAA | 53 | 68 | 27 | 25 | 125 | 133 | 144 | 67 |
| | crAAAm | 71 | 109 | 38 | 18 | 51 | 105 | 144 | 74 |
| 3~5 | PAA | 61 | 61 | 23 | 21 | 73 | 79 | 149 | 140 |
| | crAAAm | 69 | 80 | 22 | 18 | 79 | 97 | 205 | 72 |
| | Sartobind C | 55 | 20 | 6 | 6 | 20 | 20 | 500 | 33 |
| | Sartobind S | 73 | 73 | 19 | 43 | 83 | 37 | 93 | 100 |

**Table 5-10** shows the static and dynamic binding capacity of batch I membranes determined using CIM module. Comparing with the data using SCell module (for batch II membranes) in **Table 5-3**, the SBC values of membranes are similar to batch II, i.e. for the same membrane type, the SBC decreased after introduction of the cross-linked layer (crAA) and the diluent (crAAAm). The SBCs for Lys are generally larger than for IgG. The SBCs for crAAAm membranes is in the same range for both proteins.

An overview of dynamic performance of batch I membrane measured using CIM module is presented in **Table 5-11** . Comparing the data measured using SCell module in **Table 5-8**, it is obvious that the utilization of SBCs at 10 ml/min (max. DBC vs SBC) are in most cases lower than 80%, in striking contrast to the values measured using SCell module (the values were commonly larger than 80%, **Table 5-8**).

While the 10% dynamic utilization using SCell module is around 49~60% for photografted membranes, the values using CIM module are only 18~25%. Reference membrane Sartobind S has only 19%, much lower than the measured value using SCell module (≥ 60%). In comparison with the CIM module, the increase of maximum dynamic binding capacity using the Scell module is around 40%. The increase for breakthrough capacity (measured at 10% protein concentration in permeate) is over 50%. The effect of protein size and flow rates measured using CIM module is also higher than using SCell module. An increasing of flow rate leads to dramatic reduction of 10% DBC.

### 5.3.2. Model based quantitative characterization of the internal flow distribution within membrane modules

Radial multi-zone flow model (**Section 2.8.2.**) was employed for quantification of flow distribution within membrane modules. The model is mathematically represented and analytically solved as a network of continuously stirred tank reactors (CSTR). An additional plug flow reactor (PFR) is connected in series with the CSTR network in order to account for a time-lag that is not associated with system dispersion (**Figure 2-12**). The capability of the model to describe experimental breakthrough data was compared to the often applied standard model for extra-membrane system dispersion which consists of a single CSTR in series with a PFR (**Figure 2-10**). The commercial CIM module and a custom designed SCell module were studied with acetone and lysozyme as test tracers at varied flow rates and for varied membrane pore sizes under non-binding conditions.

Axial symmetry was assumed in the radial zone model, i.e. $\tau_{ia} = \tau_{ib}$ for $1 \le i \le n$. The least squares residual $r_{LS}$ and the maximal absolute deviation $r_{\max}$ were used for judging the quality of the curve fittings. A maximum absolute deviation $r_{\max}$ between 1 and 5 percent was considered satisfactory, since lower values could not be achieved due to measurement noise. In most cases, satisfactory curve fittings were achieved with the radial zone model and a minimal number of two zones for the Scell module and of one or two zones for the CIM module, depending on the test tracers.

**Figure 5-27** compares experimental breakthrough curves (black) and the corresponding best fitting model simulations (red) for the Scell module (left panel) and for the CIM module (right panel). The breakthrough curves were measured at 10 ml/min using 1~2 µm membrane and 2 wt% acetone, i.e. under non-binding conditions. The shown curve fittings were performed with $n$ = 0, 1 and 2 (top to bottom). For the traditional CSTR-PFR model ($n$ = 0) an obvious discrepancy between fitted and measured breakthrough curves was observed at the breakthrough point for both modules. The zone model with $n$ = 1 reduced this discrepancy in the breakthrough phase for Scell module, and shifted the distortion to the transition phase between linear and plateau of breakthrough curves (**Figure 5-27b**). Meanwhile, suitable curve fitting was achieved with one zone for the CIM module (**Figure 5-27e**). The maximal absolute deviations were dramatically reduced from $n$ = 0 to $n$ = 1 for both modules. Two zones were required in order to achieve satisfactory curve fitting for the Scell module (**Figure 5-27c**). The maximal residual reduced further from 2.83 at $n$ = 1 to 1.93 at $n$ = 2. However, the addition of a second radial zone ($n$ = 2) did not improve the curve fitting for CIM module. The residual values did not change as compared to $n$ = 1. Hence, the special case of the proposed model with one radial zone and axial symmetry is most suitable for fitting acetone breakthrough data of the CIM module. The total void volume was relatively constant, about 1.2~1.3 ml for SCell module and about 0.4 ml for CIM module (**Table 5-12**). These data are in good agreement with the experimental results from frontal analyses for both module systems.

**Table 5-12.** Breakdown of the total system volume into PFR volume and the volume of the CSTR network (average over n = 0, 1 and 2) as determined by fitting breakthrough curves that were measured using lysozyme and acetone for unmodified membranes with different pore sizes under non-binding conditions.

Test tracer: 2 mg/ml lysozyme

| membrane pore size [µm] | average volume _SCell [ml] | | | average volume _CIM [ml] | | |
|---|---|---|---|---|---|---|
| | V_total | V_PFR | V_CSTR | V_total | V_PFR | V_CSTR |
| 0.45 | 1.37 | 0.58 | 0.79 | 1.77 | 0.27 | 1.50 |
| 1~2 | 1.30 | 0.60 | 0.70 | 1.80 | 0.21 | 1.58 |
| 3~5 | 1.23 | 0.57 | 0.66 | 1.32 | 0.19 | 1.12 |

Test tracer: 2% acetone

| membrane pore size [µm] | average volume _SCell [ml] | | | average volume _CIM [ml] | | |
|---|---|---|---|---|---|---|
| | V_total | V_PFR | V_CSTR | V_total | V_PFR | V_CSTR |
| 0.45 | 1.53 | 0.63 | 0.90 | 0.36 | 0.23 | 0.13 |
| 1~2 | 1.32 | 0.67 | 0.64 | 0.41 | 0.20 | 0.21 |
| 3~5 | 1.30 | 0.62 | 0.68 | 0.43 | 0.19 | 0.24 |

Breakthrough curves using lysozyme under the same conditions could be well modeled using two radial zones. The best curve fittings were achieved by shifting the transition phase (**Figure 5-28**). The total estimated volume of the Scell module stays at approx. 1.2~1.3 ml as is the case with acetone, however, the corresponding values for the CIM module strongly fluctuated and drastically increased for $n = 2$ (**Figure 5-28d-f**). **Table 5-12** shows the average volumes as determined by the best curve fittings with $n = 0$, 1 and 2. The apparent total void volume of the CIM module was determined at 1.32~1.77 ml using lysozyme and at approx. 0.4 ml using acetone as test tracers. The Hydrosart membranes do not have binding ligands and are made from non-binding cellulose, and hence no binding should occur. However, the significant time-lag in the breakthrough curves of **Figure 5-28** indicated that non-specific binding has taken place in the CIM module, and this is probably due to the porous discs. The value for non-specific protein binding in this module is approx. 2~3 mg/ml (cf. (*139*)).

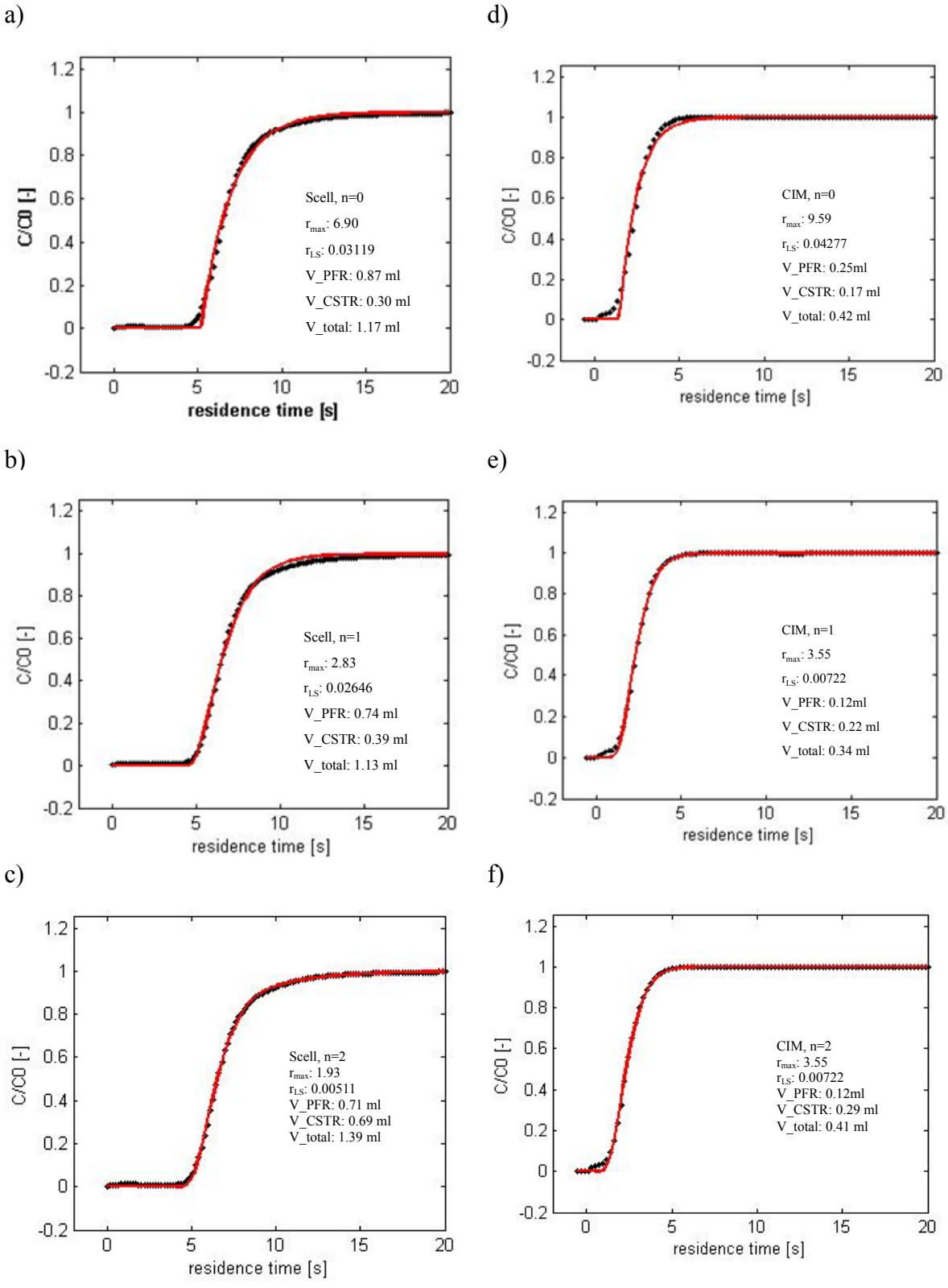


**Figure 5-27.** Breakthrough curves (black) of Scell (left panel) and CIM (right panel) membrane module versus best fits (red) of (top to bottom) traditional model ($n = 0$), radial zone model with one zone ($n = 1$) and with two zones ($n = 2$). Breakthrough curves were measured at 10 ml/min using 1% acetone and 1~2 µm membrane under non-binding conditions.

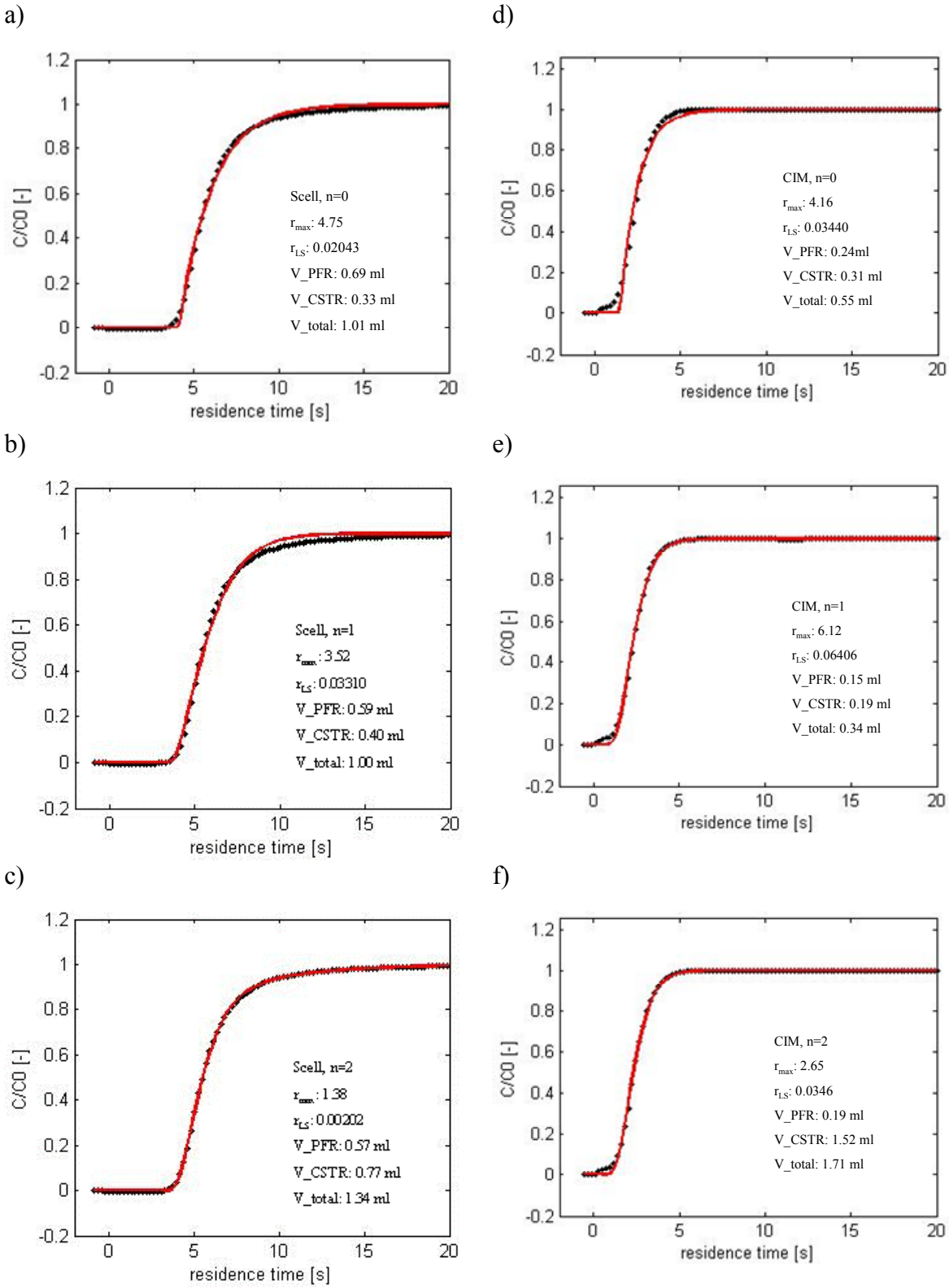


**Figure 5-28.** Breakthrough curves (black) of Scell (left panel) and CIM (right panel) membrane module versus best fits (red) of (top to bottom) traditional model ($n = 0$), radial zone model with one zone ($n = 1$) and with two zones ($n = 2$). Breakthrough curves were measured at 10 ml/min using 2 mg/ml lysozyme and 1~2 µm membrane under non-binding conditions.

# 6. Discussion

## 6.1. Detailed analysis of membrane adsorber pore structure and protein binding by advanced microscopy

### 6.1.1. Images comparison

The morphologies for the bottom side of Sartobind membranes performed by SEM in dry (**Figure 5-4a**) and by ESEM in wet state (**Figure 5-4c**) are quite similar, i.e., a very coarse structure, consisting of relatively thick cellulose-based fibers connected to a network of fine fibers and clustered membrane material, together forming the macropores on the outer surface. Due to intrinsic difficulties with investigations of the porous membranes in completely wet state in the ESEM, the effects of water uptake and release from the gas phase of membranes have been investigated, and had observed that smaller fibers within the macropores showed a significant volume change and mobility, while the macropore network remained unchanged. However, under the experimental conditions in ESEM, the scanned outer membrane surface does presumably not contain anymore water in the pore volume, so that only the image of a hydrated membrane matrix is obtained. With help of fluorescence labeling technique in combination with CLSM, the pore morphology in completely wet state (**Figure 5-4b**) and also inside the membrane volume can be imaged (**Figure 5-5**). However, the three-dimensional resolution (> 1 $\mu m^3$) and depth of penetration in the sample (up to 20 μm) are limited. Overall, SEM, ESEM and CLSM show similar and complementary morphologies at different depths of membrane, and the morphology of CLSM image for the dye-stained membrane is similar to that in wet state measured using ESEM.

Same as the SEM images in dry state, the difference of functional layers formed by chemical grafting between membranes can not be identified by ESEM even in swelling state (**Figure 5-7**). The use of two different fluorescence dyes for labelled membrane (DTAF) and protein (Cy5) enables simultaneous visualization of membrane pore structure and protein binding to the membrane functional layer at different depth of membranes by CLSM. The visualization of protein binding was possible, and significant binding in the pore volume but not extending throughout the entire diameter of the macropores has been confirmed (**Figures 5-8, 5-9**).

### 6.1.2. Static visualization of protein binding by CLSM

Lysozyme from hen egg, consisting of 129 amino acids, has a molecular weight of 14.3 kg/mol and a pI of 11.3. Amino acids carrying positive charge are 6 lysines and 11 arginines. Along with the 9 negatively charged amino acids, a positive net charge of lysozyme at pH 7.0 had been observed (*140*). Lysozyme has a shape similar to an ellipsoid, with a length of about 5 nm and a width of about 3 nm. During protein labeling, the fluorescence dye Cy5, having a molecular weight of 789 g/mol, will be covalently attached to the primary amino group of a lysine residue. Only 1 or 2 Cy5 molecules will be bound to one lysozyme molecule under the used labeling conditions. Although molecular weight of fluorophore molecules is generally much smaller than compared to the molecular weight of protein molecules, the behavior of labeled and native protein could be different, e.g. signal overshoot in the middle of resin-based particle had been observed (*130*). The effects of labeling onto ion-exchange binding, which had been recently studied and discussed in detail for lysozyme (*132*), were considered by not using a mixture of labeled and unlabeled protein (as done in many other studies, cf. (*99, 130*)). Therefore, a mixture of all the six isoforms of mono-labeled lysozyme was used in this part. By this means, fractionation between labeled and unlabelled protein within the adsorber according to different affinities can be avoided.

Typical protein binding pattern of cellulose membrane is demonstrated in **Figure 6-1**. The (yellow color) protein fills in a relatively thick and homogeneous layer significant fraction of the macropores of membrane matrix (red color) leaving the interior of the pore empty, while the bound protein density is much lower in the region of the thick cellulose fibers, which should only be responsible for mechanical stability of the membranes. The differences in binding patterns between Sartobind C (**Figure 5-8**) and Sartobind S (**Figure 5-9**) membranes might be introduced by differences in the grafted functional polymer layers, the nature of ion-exchange group or the porous base materials as demonstrated by dynamic performance in Section 6.2.

It is important to keep in mind that the protein dimension is smaller than the lateral resolution of the method (cf. **Section 6.1.3.**). Consequently, protein visualization is based on a fluorescence intensity beyond the detection limit in a volume $\geq$ 1 $\mu m^3$. The subtle dependences of protein binding pattern illustrated in **Figure 5-10**, mainly on protein concentration, could be caused by the detection limit of the used system. An exact quantitative correlation between fluorescence intensity and protein amount has not yet been established for the used system due to the complex pore morphology (cf**. 5.1.2.1.).** As the

protein amount was given in excess, the binding sites could be saturated by protein molecules, and these differences between images could not be recognized in this study. And this difference might be explained by the differences in driving force and kinetic influences onto diffusion and binding processes determined by the protein binding isotherm, which is presumably also a function of the accessibility of binding sites of functional layer in the macroporous membrane adsorber.

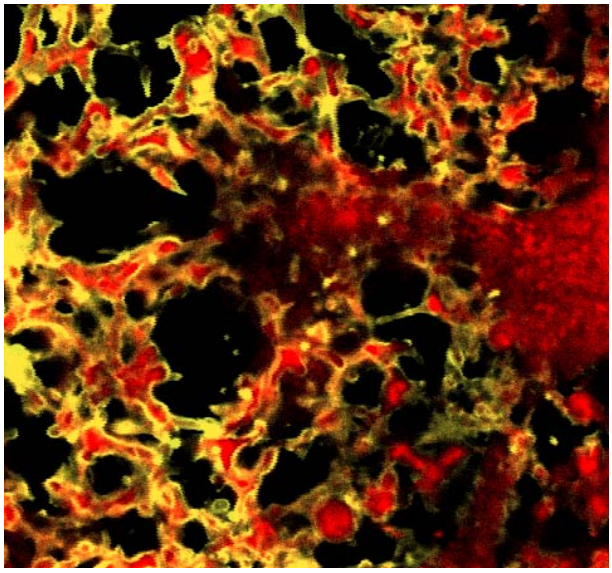

**Figure 6-1.** CLSM image of 35_crAAAm membrane, bottom side, 10 µm below the surface. Overlap of (yellow colour) labelled protein (0.4 mg/ml, pH 7.0) at 488 nm binding to (red colour) stained membrane at 633 nm.

### 6.1.3. Protein binding under flow-through and *in situ* monitoring by CLSM

The *in situ* membrane module can be simplified according to a system model as shown in **Figure 6-2,** consisting of PFR ($V_1$: the total volume of the capillaries, 88 µL), CSTR ($V_2$: the hold-up volume of the membrane module in front of the membrane, 105 µL), and the membrane volume ($V_3$: 17 µL). For the flow rate of 0.3 mL/min, the first protein would enter the hold-up volume of the membrane module ~20 s after injection. Due to mixing in volume $V_2$, the protein would start to enter the membrane from this moment. The time to reach complete saturation of all binding sites in the membrane volume ($V_3$, reduced by the volume of the 10 µm thick layer below the CLSM focus) after a step injection (which is not the case in practice, cf. above), without axial dispersion and at no kinetic hindrance by the binding, would be ~110 s.

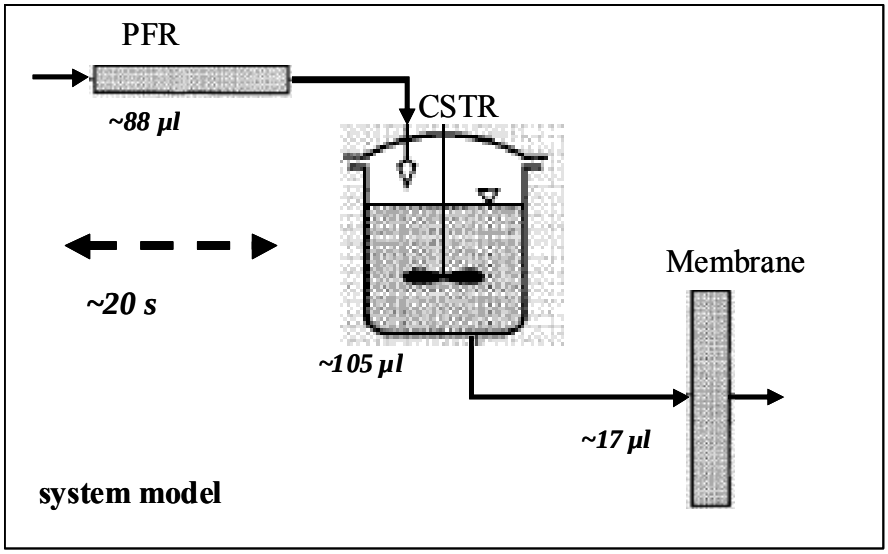


**Figure 6-2.** Simplified system model of *in situ* membrane module for CLSM, consisting of the HPLC capillary (considered as PFR) and the flow distributor before the membrane (considered as CSTR; cf. **Figure 4-1**).

Axial dispersion in the Sartobind membranes is much larger, which is demonstrated by the breakthrough curve measured at the same linear flow rate in CIM membrane module (**Figure 6-3**). The time to saturation for the Sartobind S membrane at 10% breakthrough was indeed ~70 s when compared with the unmodified base membrane having the same pore structure. Therefore, the observed delay until first protein detection in the *in situ* CLSM experiments can be quite well understood. On the other hand, the significant dispersion of breakthrough curve observed in chromatography (400 s to 100% saturation) seems to be largely underestimated in the CLSM experiment (20 s to saturation after appearance of the first trace of protein). This, however, can be explained by the not yet established quantitative relationships between fluorescence intensity and protein concentration. It should be noted that in chromatography the time between 10 and 80 % breakthrough (100 s) is also much shorter than reaching complete saturation (time between 80 and 100% are additional 300 s), and especially the latter changes are hardly distinguished by fluorescence imaging.

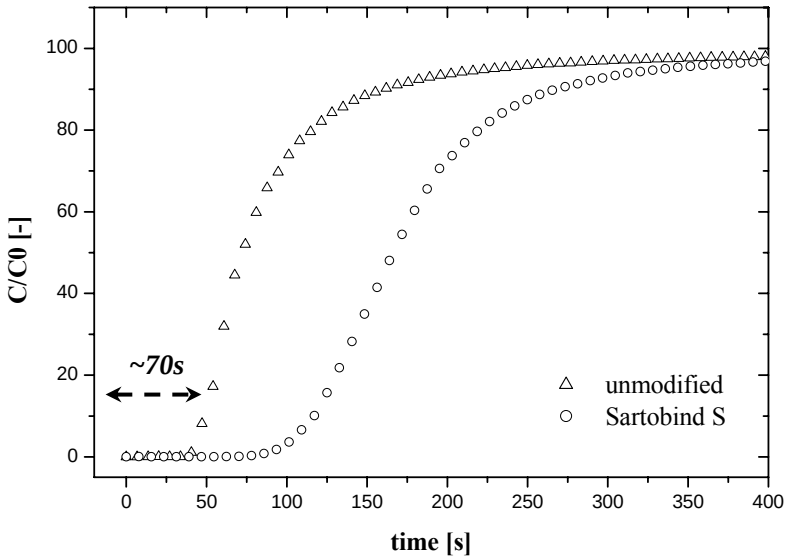


**Figure 6-3.** Breakthrough curves at 0.3 mg/ml for 1 layer of membrane Sartobind S and unmodified cellulose base membrane for 2 mg/ml Lys, measured using CIM membrane module.

Using the time-resolved data from *in situ* CLSM, breakthrough curves can also be established for the labeled protein. The fluorescence image intensity of bound protein in three selected areas (size of 2.2×2.2 μm²) as function of time was normalized by the fluorescence intensity of the labelled membrane in the same area (**Figure 6-4**). In all cases, the intensities showed a relatively large fluctuation after a relatively steep increase (**Figure 6-4b**). Because the relationship between intensity and concentration is not known (cf. above), the steepness can not be discussed quantitatively. However, the breakthrough times were significantly different. The fastest breakthrough occurred in a region with fine fibres in a macropore (area 1), while late breakthrough was seen in an area close to a very thick cellulose fibre (area 3). One should keep in mind that the plane of observation was ~220 μm behind the outer surface where the protein had entered. Nevertheless, it may be conceived that the very heterogeneous morphology of membrane causes uneven flow distribution, e.g. channelling. The design of the flow-through cell, which is limited here by the operation conditions (cf. **section 4.2.1.3.** and **Figure 4-1b**), could be another important contributor to the system dispersion in this chromatographic system.

a)

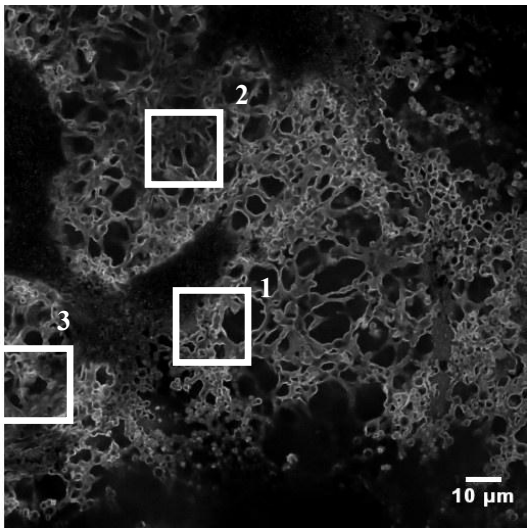


b)

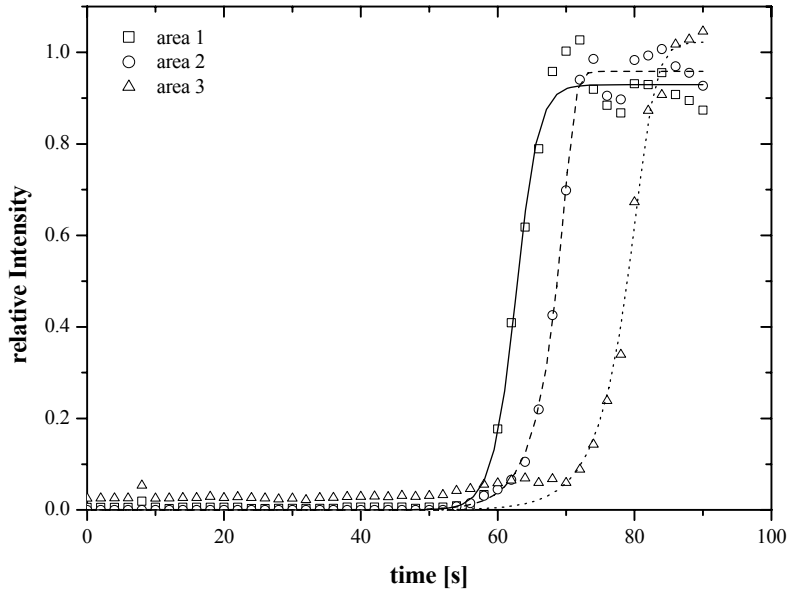


**Figure 6-4**. a) Image of bound lysozyme (633 nm) in Sartobind® S membrane after 84 s (cf. **Figure 5-11**): The highlighted areas (2.2×2.2 µm$^2$) were selected for construction of breakthrough curves from complete data set; b) breakthrough curves of the areas shown in a). The intensity of protein fluorescence was normalized by the fluorescence intensity of the labelled membrane in the same area.

Therefore, the most important conclusion from this experiment is that in addition to the information from conventional chromatography evaluation with respect to (average) axial dispersion, the lateral microscopic resolution in the x-y plane can give much additional information about possible reasons of such loss in chromatographic resolution.

### 6.1.4. Limitation of the used microscopic methods

ESEM was used to study how the membrane pore geometry would change upon uptake or release of water from/to the gas phase. This compromise had been chosen because the investigation of water-wet sample did not yield images where the pore structure could be clearly resolved (cf. **5.1.2.1.**). The lateral resolution achieved for Sartobind membranes at a relative humidity of 50% was about 100 nm, far away from 5 to 10 nm for standard SEM under ideal conditions (*141*). The main reason for this is the property of the regenerated cellulose membrane, i.e. its non-conductivity (release of excessive charge built-up due to electron beam is by absorbed water only) and its pronounced sensitivity to heating by the electron beam during scanning.

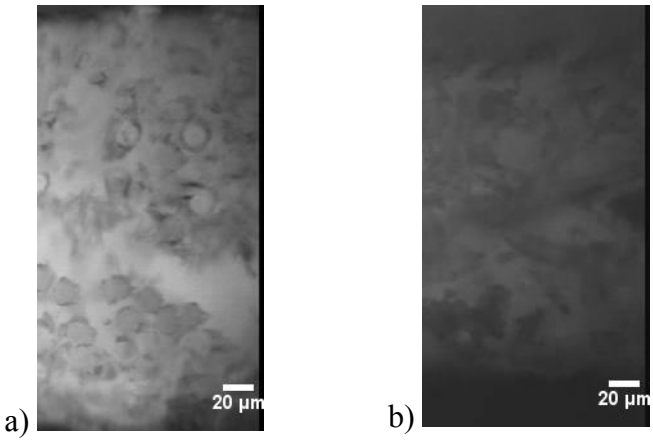


**Figure 6-5.** Fluorescence microscopy images of cross section of a) Hydrosart membrane; b) Sartobind S membrane. The membranes were stained using 10 µg/ml DTAF.

***Staining of membranes***

CLSM allows noninvasive image scanning at variable depth within the membrane; i.e. it has the potential for visualization of pore structure in three dimensions. However, lateral resolution and sensitivity depend critically on the fluorophor which is essential for detection and on the intensities of excitation and emitted light within the three-dimensional object. For a material with no intrinsic fluorescence, staining with a fluorescence dye is necessary. The staining intensity and its variation in different depths within the specimen can result in different attenuation of excitation or emitted light. This problem is less relevant in this study because the sampling depth was limited due to other reasons discussed below. During this study, it was observed that the efficiency of the labeling reaction of the cellulose matrix with the hydroxyl-reactive dye was lower for the S than for the C membrane as illustrated by cross section image measured by fluorescence microscopy in **Figure 6-5.** This can be explained by electrostatic repulsion between the dye derivative, carrying a negative charge under labeling conditions, and the sulfonic acid groups of the S membrane, and this problem had been reduced by using a higher salt concentration during staining of the S membranes (cf. **Section 4.2.2.3.**).

One possible reason for this is the necessity to label the protein molecules with a fluorophore. Molecular weight of fluorophore molecules is generally much smaller than compared with the molecular weight of protein molecules. Protein labeling will alter the rate of rotation of both molecules and always implicates the difference a change of adsorption behavior (*142*). Under circumstances the difference between the native and labeled protein can be big enough to cause unexpected confocal scans such as signal overshoot as shown in **Figure 6-6**. This was taken into account by using only Cy5-Lys isoform for the investigation of static binding capacity of Sartobind membranes (**Sections 5.1.2.3. and 6.1.1.**).

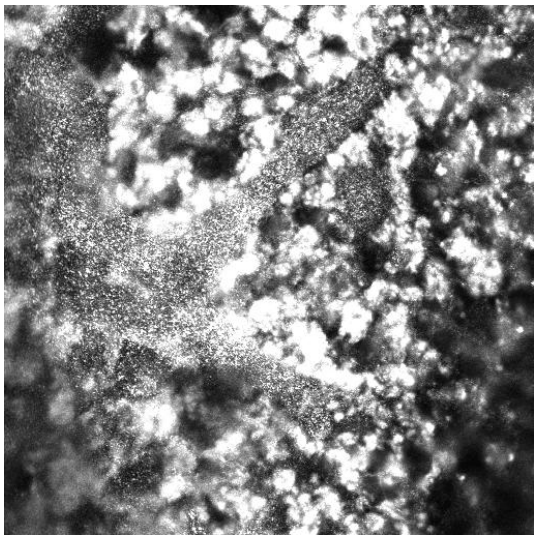

**Figure 6-6.** CLSM images of Sartobind C, bottom side, 16 µm from the outer surface. The membrane was incubated with 2 mg/ml mixer of LYS-Cy5 isoform and native for 60 min.

***Light attenuation***

As shown in **Figure 5-5**, obtained quantitative images depth is approx. 20 µm. Another major difficulty in the application of CLSM results from light attenuation. Excitation and fluorescence light are attenuated in dependency of the location of focused point, different fluorescence signals can be obtained from the same amount of labeled protein thus resulting in false conclusion about protein distribution of adsorptive materials. Light attenuation can be generated by many environmental parameters, such as refraction index mismatch among the objectives, solid phase and used immersion medium, fluorophore concentration dependent reabsorption of excitation and emitted photos in a specimen, photo-bleaching and quenching of fluorophores as well as fluorescence dye environment (*97, 100, 143, 144*). The optical elements in the microscope, heterogeneous morphology and autofluorescence of investigated materials should be also taken into account.

Refraction index mismatch causes a loss of excitation as well as emitted fluorescence intensity. A mismatch of refraction index results in an incorrect scaling of an image stack in the axial direction and in increasing spherical aberrations, which broadens the point spread function (PSF) of CLSM. The PSF width increases with focusing deeper inside the specimen and causes spreading of excitation energy over a larger volume, thus reducing the fluorescence

signal. Objects in a specimen comparable to or smaller than the wavelength scatter both excitation and emission light. The major source of scattering in the analysis of protein-dye conjugate is generated by so called Raleigh scattering (*90*). Objects larger than the wavelength and having a different refraction index from the environment partially refract both excitation and emission photons. Scattering and refraction depend mainly on the morphology and density of the specimen (*97, 145*).

When light moves from a medium with reflection index $n_1$ into a second medium with reflection index $n_2$, both reflection and refraction of light may occur by the same upper structure on their back way (**Figure 6-7**). The most common effect is refraction of light, referred as the ratio of illumination intensity $I_{ref}$ to reflected intensity $I_0$. It is the key factor to determine signal strength giving by equation (6-1) as following:

$$\frac{I_{ref}}{I_0} = \left( \frac{n_1 - n_2}{n_1 + n_2} \right)^2 \qquad (6\text{-}1)$$

The smaller the difference in the refraction index n between the two media, the larger is the observed thickness. Together with light absorption effects caused by the upper structure of same material, this self-shadowing effect reduces image contrast by lowering the signal strength.

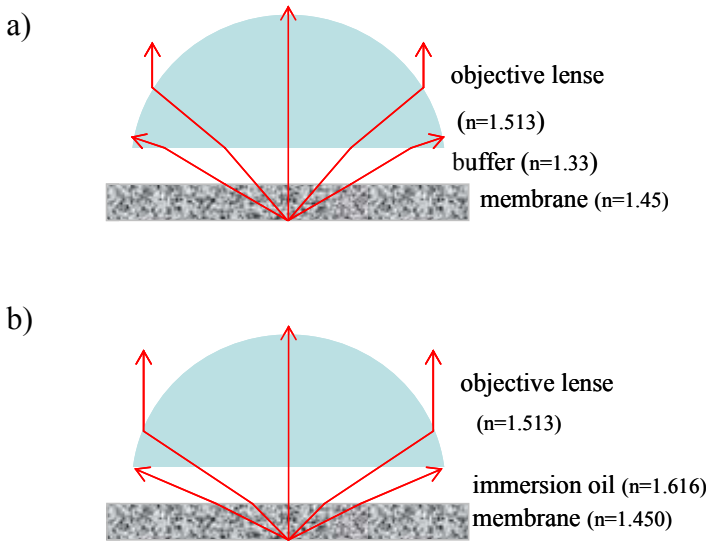


**Figure 6-7.** Light refraction of detection system in CLSM. A) Phosphate buffer; b) Oil, as immersion medium.

The refraction index is 1.45 for cellulose and 1.513 for objective lines. For the investigation system for commercial Sartobind membranes, aqueous phosphate buffer (n = 1.33) had been used as immersion medium (**Figure 6-7a**). The mismatch of refraction index causes a steep decay of excitation intensity over thickness. This problem should be less relevant for new prepared membranes because immersion oil (n = 1.616) was used as detection medium (**Figure 6-7b).** However, significant change in visible depth (larger than 20 µm) could not been recognized (**Section 5.2.8.**).

Photo-bleaching can cause an irreversible decay of fluorescence with time. The susceptibility towards photo-bleaching varies with respective fluorophores. This problem is more pronounced for the fluorescein derivative DTAF used for membrane staining than for the Cy5 dye used for the protein labeling (cf. **5.1.2.3**). The scanning times was adapted accordingly, and scanning sequence of images had been generated in multi-track mode (**Section 4.2.2.3.**).

Florescence quenching reduces the fluorescence quantum yield, but does not change in the fluorescence emission spectrum. It is dependent on used labeling concentration and labeling degree (*90*). For this reason, some works have employed mixture of labeled and native protein in order to avoid fluorescence quenching. This problem is less relevant in the study of 3~5 µm and 1~2 µm for commercial (**Figure 5-11**) and new prepared membranes (**Figures 5-23a** and **5-23b**), however, as shown in **Figure 5-23c**, it could be a problem for the compact structure of 0.45 µm membrane.

Reabsorption of emitted light occurs when the Stoke's shift of the used fluorophores is small enough to cause an overlap of the excitation and emission spectra. A part of the photons, which have been emitted after the excitation of the fluorophore, can be reabsorbed by other fluorophore molecules on the path between the focal point and the detector, thus attenuating the detected signal. The detected signal will be reduced in dependence of the concentration of fluorophores. It can be minimized or even fully neglected when a very low florophore concentration is used for experiment (*146*). The influence of reabsorption could be compensated by the linear correlation between fluorescence intensity and the concentration of adsorbed protein-dye conjugates (*93*).

A common method to compensate and correct for light attenuation is the "Contrast matching" technique which is based on the addition of additives, such as DMSO (*99*), aqueous sugar solution (*147*), dimethyl sulfoxide (*144*), into the chromatographic system in order to adjust the refraction index of the liquid phase. However, as shown in **Figure 6-8**, the usage of DMSO as immersion medium did not yield notable improvement in scanning depth. It reveals

that the refraction index mismatch is not the main factor for light attenuation during this work. Furthermore, this modification has changed the real operation conditions for chromatographic process. Other approaches for compensation of light attenuation involves correction in z-scan as performed for resin-based particles by Dziennik (*148*) or biological membrane by Čapek (*145*). However, their prerequisite is homogeneous loaded specimen. Mathematical approaches to solve the light attenuation problem by applying a physical model of excitation and fluorescence emission phenomena has been reported for resin based particles (*143, 149*). By the way, the auto-fluorescence effect of regenerated cellulose materials at a certain wavelength was eliminated by setting of adapted gain values in this work (cf. **Section 4.2.2.3.**). Overall, the anisotropic morphology of the Sartorius membranes, a random network of irregular shaped elements of varied size (cf. **Figure 5-3**), is critical for the complications to describe correctly light attenuation in the CLSM experiments.

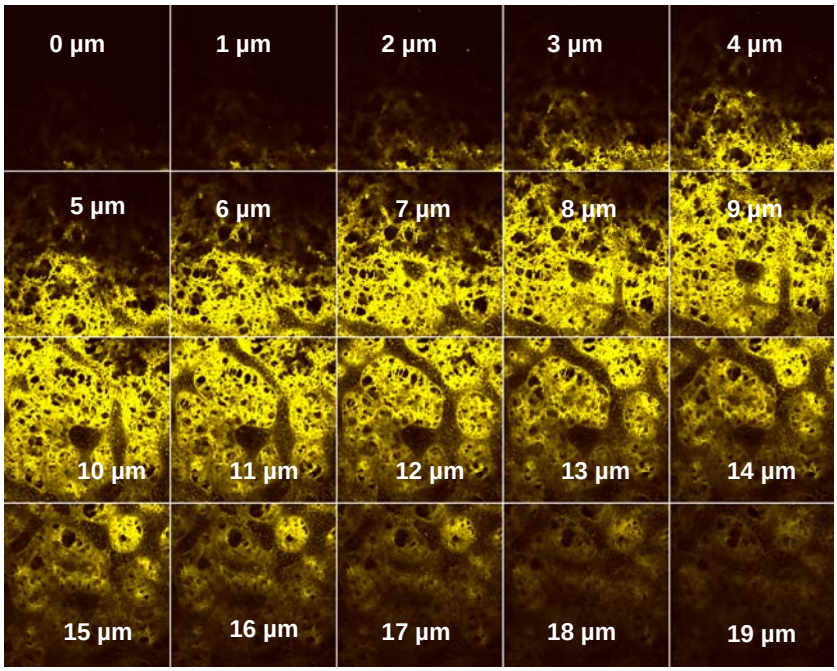


**Figure 6-8.** CLSM image of Sartobind S membrane, bottom side, after bound with 0.03 mg/ml Cy5-Lys isoform for overnight, and immersed in DMSO for 1hour.

***Resolution of the CLSM system***

The limit of lateral resolution of a CLSM can be estimated using the point objects method of Inoué (*90*) (cf. (*97*)) (**Appendix 8**). The image of an infinitely small luminous object point is itself not infinitely small, but is a circular Airy diffraction image with a central bright disk and progressively weaker concentric dark and bright rings. The lateral resolvable diameter of an object in a specimen, $d_{Airy}$, depending on the wavelength of light in vacuum and numerical aperture of the objective lens calculated according to the Rayleigh criterion is about 1 μm for the used CLSM system. The accuracy in z direction is due to the focus of the excitation light which is also larger than 1 μm. Objects are resolved if their dimensions are larger than 1 μm. Consequently, using CLSM only macro-pores larger than 1 μm can be separately identified in the stained membranes as in the case with photo-grafted membranes (**Figure 5-23**). The protein binding images of membranes with pore size ≥ 1 μm can be well resolved. The visualization of bound protein is based on a fluorescence intensity beyond the detection limit in a volume $\geq$ 1 $\mu m^3$. No significant differences could be identified between CLSM images of 3~5 μm membranes with different grafted functional architectures (cf. **Figure 5-24**), probably because the resolution of this method is too low to detect differences in the dimension of the thickness of the grafted layers on the pore walls. The prerequisite to solve the above problems for quantification of protein binding to membrane is to establish an exact quantitative correlation between fluorescence intensity and fluorophores amount. Irrespective the technical problems with CLSM in the highly irregular pore structures making exact quantitative estimations very complicated, all results can be discussed with respect to the protein distribution in the system of membrane macropores as well as the relative bound protein amount in the x-y plane, indicated by the light intensity acquired at same CLSM z-position and gain setting.

## 6.2. Influence of pore structure and architecture of photo-grafted functional layers on separation performance[2]

### 6.2.1. Base membrane

The cellulose 0.45 μm, 1~2 μm and 3~5 μm membranes used in this study exhibit a complex macroporous structure, with a relatively wide range of pore size distribution, in particular for the large pore 1~2 μm and 3~5 μm membranes. The membranes showed typical trends with the increasing pore size: specific surface area decreased, permeability increased and the pore size distribution became broader (cf. **Table 5-2** and **Figure 5-14**). The permeability correlates well with the pore size (cf. **Table 5-2**). Only for the 0.45 μm membrane, the pore size distribution was similarly narrow to those of commercial MF membranes (*150, 151*).

### 6.2.2. Grafted functional polymer layers by UV-initiated grafting

The UV-initiated grafting of AA monomer to the membrane surface results in a polymer layer architecture carrying negatively charged carboxylic groups. The liquid displacement method provides pore size distribution at conditions where the grafted polymer layer is collapsed. When considering the permporometry data (cf. **Figure 5-14**), it should be kept in mind that only the smallest part of each pore size in the membrane barrier was detected. A significant reduction of the pore size had been observed for all three base membranes after grafting of the PAA polymer. However, the grafting did not change the morphology of the base membrane significantly as observed from SEM (Appendix **Figure 8-2** and **8-3**) and CLSM images (**Figure 5-23**). This can be related to the well-documented surface selectivity of the photo-initiation using the "type II" photoinitiator benzophenone leading to end-on grafted polymer chains on a preserved base polymer (*10*). The degree of grafting can be adjusted by UV irradiation time (**Figure 5-15a**). The efficiency of the grafting functionalization expressed as the degree of grafting (equation 4-4). It was slightly influenced by the pore structure: for the 0.45 μm membranes with about 2 times larger specific surface than for the other two membranes (cf. **Table 5-2**), higher DG values had been achieved under the same conditions (cf. **Figure 5-15a**).

A deviation of DG values from saple to sample in the range of up to 20% had been observed. This could be generated by the used small area of prepared membranes (diameter 25 mm) and inhomogeneous irradiation by the used UV-lamp.

[2] The discussion about dynamic performance of membranes in section 6.2 is based on the measurement using Scell module.

The liquid permeability data are of direct relevance for performance of membrane adsorbers. Since the $pK_a$ of carboxyl groups is about 4.5, the functional ligands are deprotonated at pH 7. This leads to a pronounced extension of the polymer chains from the pore surface toward the pore interior due to an electrostatic repulsion in a buffer with low ionic strength (10 mM potassium phosphate buffer, pH 7.0 or 20 mM sodium acetate, pH 5.0).

The salt effect was very pronounced, since a high ionic strength solution screens the electrostatic interactions: the grafted PAA chains collapse and this causes the increase of permeability using buffer A (10 mM potassium phosphate buffer, pH 7.0) or B (20 mM sodium acetate, pH 5.0, plus 1 M salt). During the chromatography process, the bound protein is eluted by this means through breaking the ionic bonds. However, also in the de-swollen conformation, the reduction of effective pore diameter by the grafted polymer was still significant. The changes of pore size distribution judged from liquid permeability using 10 mM potassium phosphate buffer indicated that the resulting grafted layers in the pores had indeed a thickness in the range of up to several hundreds nanometers. The calculated thickness of grafted layer after Hagen-Poiseuilie law (equation 2-5) is approx. 280 nm for 35_crAAAm and approx. 480 nm for 35_PAA. Such extension causes a narrowing or even blocking of membrane pores, and this had been observed as a reduction of the membrane permeability (cf. **Figure 5-15b** and **Table 5-4**).

### 6.2.3. Influence of internal architecture of grafted functional layers

An adapted structure of functional layers can be implemented by using UV-initiated functionalization. The charge density of ion-exchange groups can be diluted by introduction of an uncharged spacer between the repeating units of grafted chains. The stabilization of binding layers can be reinforced by chemical cross-linking, which restricts their flexibility to some extent depending on the content of cross-linker (**Scheme 6-1**). The influence of different architectures of the grafted polymer layer on the membrane performance was investigated using the crosslinker (crAA) and an uncharged monomer (crAAAm) as additives in the grafting monomer mixtures (**Table 4-2**). Due to the low permeability of the grafted 0.45 µm membrane, the shorter irradiation time of 4 min had been chosen in contrast to the 1~2 µm and 3~5 µm membranes with 8 min irradiation time. For a proper comparison, the values of ion exchange and protein binding capacities were normalized to the weight of the grafted polymer (DG).

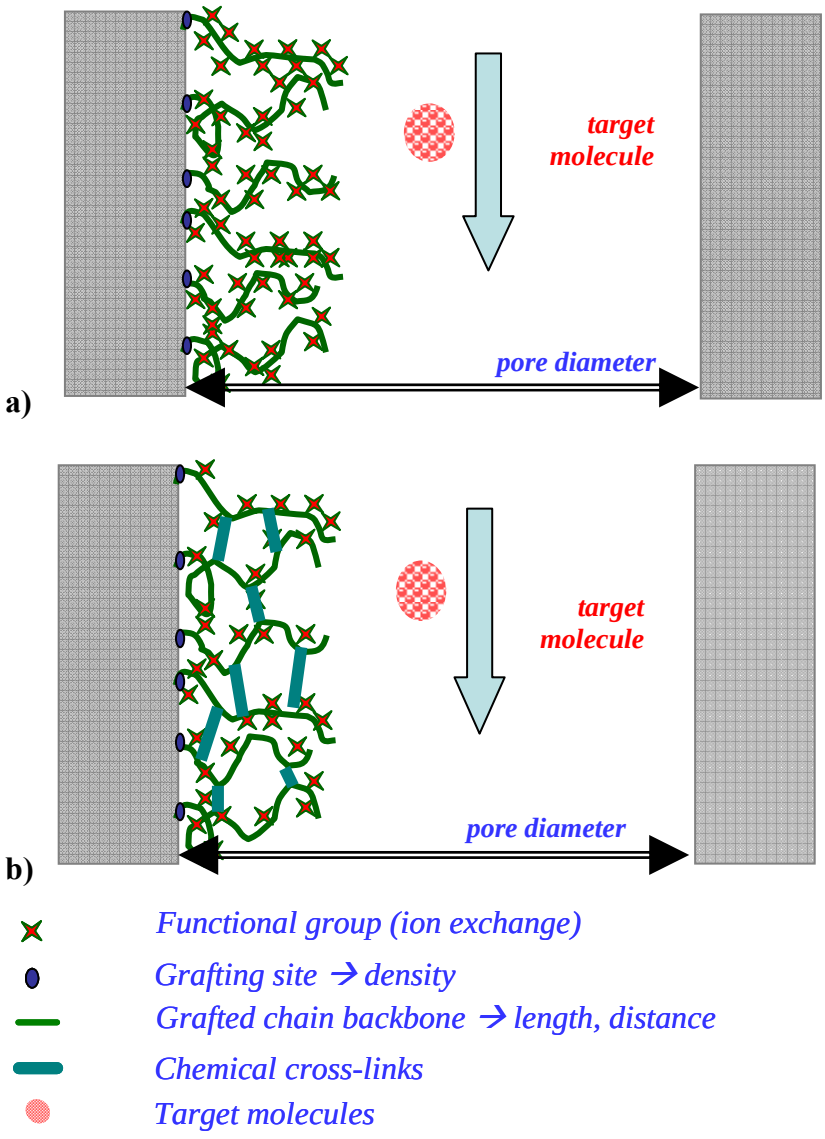


**Schema 6-1.** Adapted architecture of grafted functional layer: a) linear polymer chains with high density of ion-exchange groups; b) linear polymer chains with suited dilution of ion-exchange groups and stabilization of binding layer by chemical cross-linking.

#### 6.2.3.1. Ion exchange capacity

**Figure 6-9** shows the correlation between ion-exchange capacity from titration (cf. **Table 5-3**) and pH transient area for membrane adsorbers prepared by surface functionalization of different base membranes using different monomer mixtures. Data were normalized by the grafted polymer amount. The normalized ion-exchange capacity exhibited a decreasing trend as consequence of grafting with cross-linker, and further by dilution of charge density, and less dependence of pore size of base membranes (cf. **Table 5-3**).

Taking all results (**Table 5-3**, **Table 5-5**) for the various membranes together, it can be concluded that with increasing amount of carboxylic groups in the membrane, the amount of protons consumed by the step decrease of salt cation concentration in the liquid phase also increased. The fair correlation between pH transient area and ion-exchange capacity of membranes with various functional layers from back-titration confirms the consistency of both methods (**Figure 6-9**). Hence, the higher capacity of the PAA type relative to the crAA and crAAAm type membrane adsorbers for all pore sizes can be also confirmed by the alternative, dynamic determination method.

Although the total static ion-exchange capacity can be determined via back titration method, the membranes must be broken into small pieces. The non-invasive pH transient method provides the possibility for dynamic test of ion-exchange capacity for membrane adsorbers in analog to monolithic chromatographic column (*113*) without destroying of membranes, however, this method will take relative long time (cf. **Section 5.2.4.**).

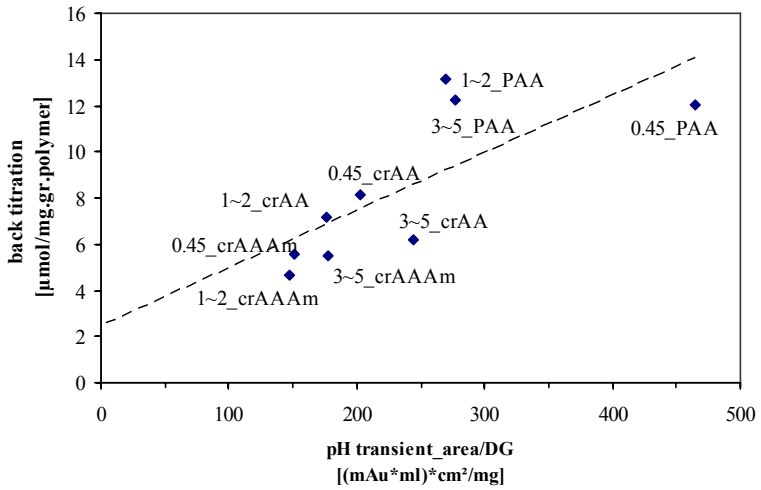


**Figure 6-9.** Correlation between ion-exchange capacity from titration (cf. **Table 5-3**) and pH transient area for membrane adsorbers (cf. **Table 5-4)** prepared by surface functionalization of different base membranes using different monomer mixtures. Data were normalized by the degree of grafting.

As the standard deviations of back titration were very small, the measured value for AA with cross-linker seemed too small. This unexpected discrepancy might be understood by gradual collapse of polymer chains resulting from mutual attraction of ion-pairs formed by the counterion condensation beyond a critical value of the charge density of the polymer chains as predicted by Manning (*151*) (**Figure 6-10**). Such a polymer network collapse due to ion-pair association was further confirmed by cross-linked polyelectrolyte gels in aqueous medium. In some regimes, an increasing degree of ionization during titration can lead to an initial swelling of the gel upon charging with subsequent jumplike collapse at a higher fraction of charged monomer units (*137, 150, 152*). This behavior is probably similar to one of the cross-linker grafted functional chains in this work.

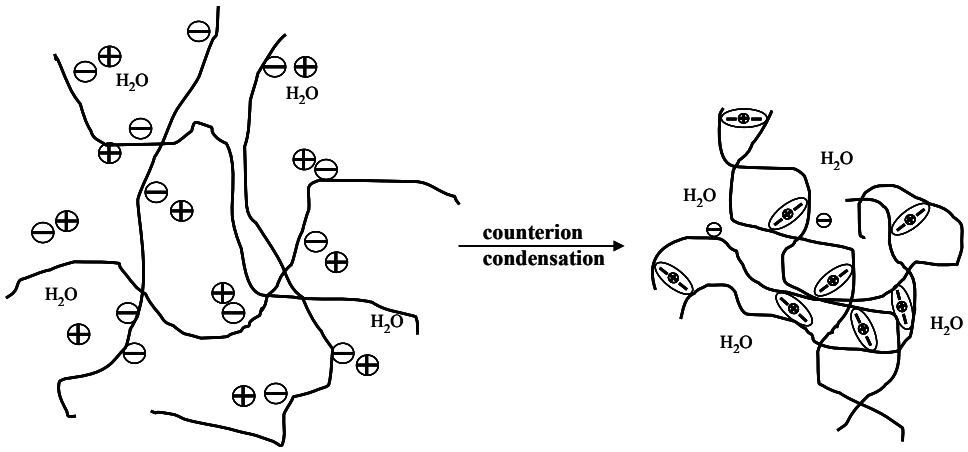


**Figure 6-10.** Counterion condensation of polymer chains resulting from mutual attraction of ion-pairs formed by the counterion condensation beyond a critical value of the charge density of the polymer chains as proposed by Manning (*151*).

### 6.2.3.2. Membrane permeability and static binding capacity

In **Figure 6-6a**, it can be seen that the magnitude of the permeability of the grafted membranes is predominantly determined by the pore size of the base membrane. Overall, a trade-off exists between the ion-exchange capacity (cf. **Figures 6-11** and **6-12**), which is a function of DG, and the permeability of the surface-functionalized membranes. The grafting of the PAA caused the strongest decrease of permeability followed by the crAA and crAAAm polymer architectures. The introduction of the crosslinker and the uncharged monomer resulted in a dilution of the charged carboxylic groups in the grafted polymer layer by ~60% for crAAAm, respectively. Consequently, higher permeability and lower static binding capacities had been observed for both proteins Lys and IgG, when the charge density in the grafted polymer layer was reduced (**Figures 6-12a**, **6-12b** and **Table 5-3**).

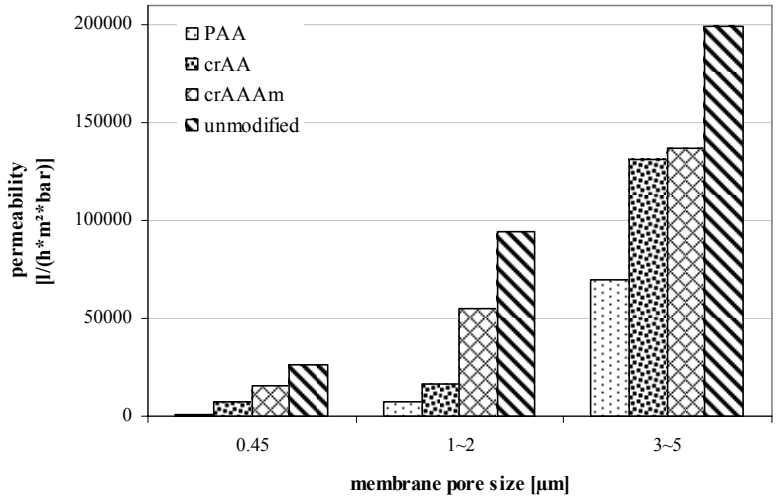


a)

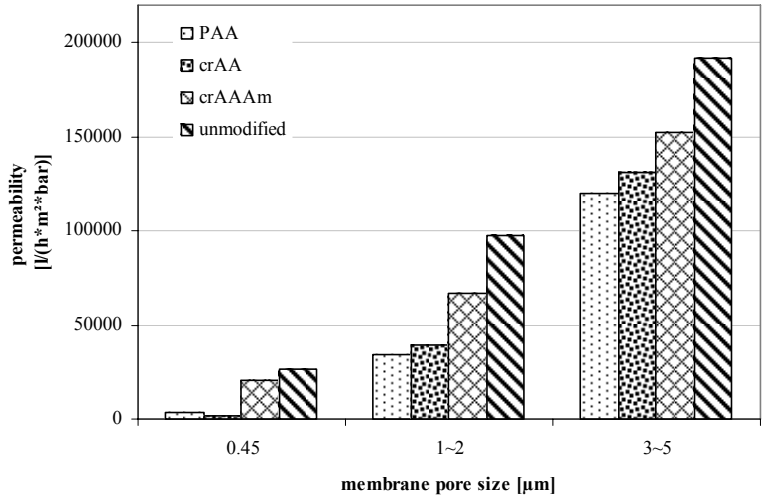


b)

**Figure 6-11.** Dependence of permeability of membrane adsorber upon the base membrane type and functional layer structure, measured using: a) buffer A; b) buffer A + 1 M NaCl.

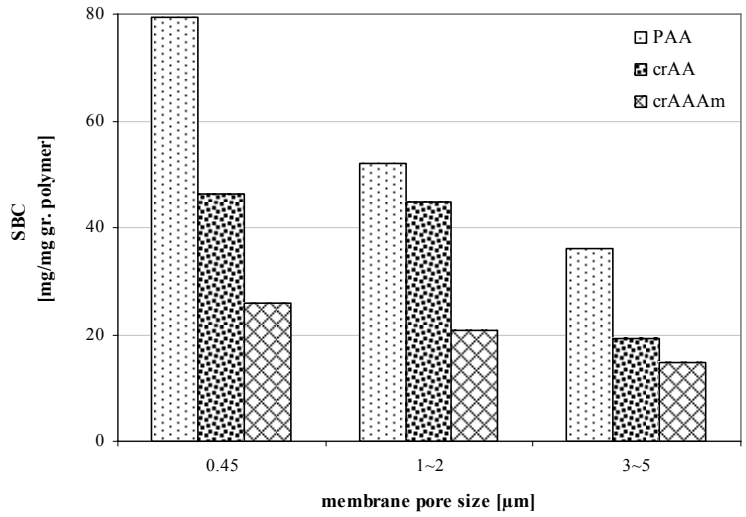


a)

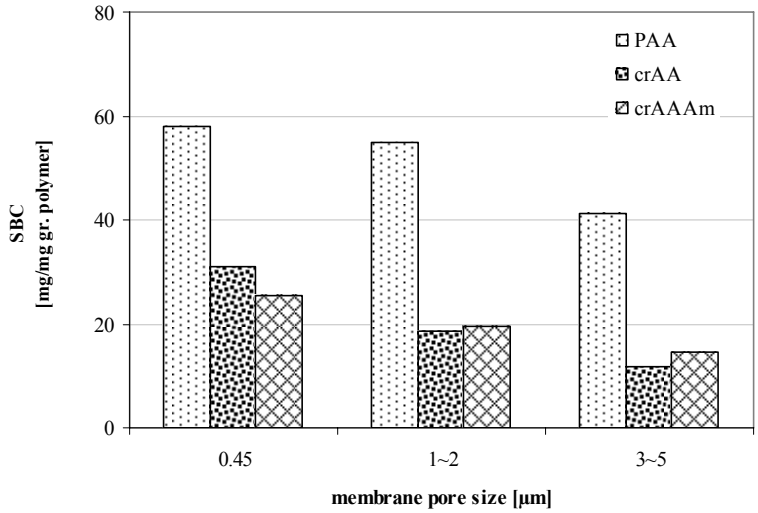


b)

**Figure 6-12.** Static binding capacity of membrane adsorbers with different pore sizes and grafted layer structures for: a) Lys; b) IgG.

An overview about the correlation between static binding capacity (for Lys) and permeability (for 10 mM potassium phosphate buffer, pH 7.0) is plotted in **Figure 6-13** for all functionalized membranes with varied grafting structure and UV irradiation time.

In addition to high binding capacity to proteins, an adapted membrane adsorber should have high throughput under low transmembrane pressure drop, i.e. possible compromise between high permeability and improved binding capacity as indicated by the red arrow in **Figure 6-13**. 0.45 µm membrane indicated high SBC with compensation of permeability, i.e. a pronounced

trade-off effect between SBC and permeability can be identified. In contrast, with similar values of SBC, 1~2 µm and 3~5 µm showed larger values in permeability. It seems that increasing of pore sizes could reduce such trade-off effect.

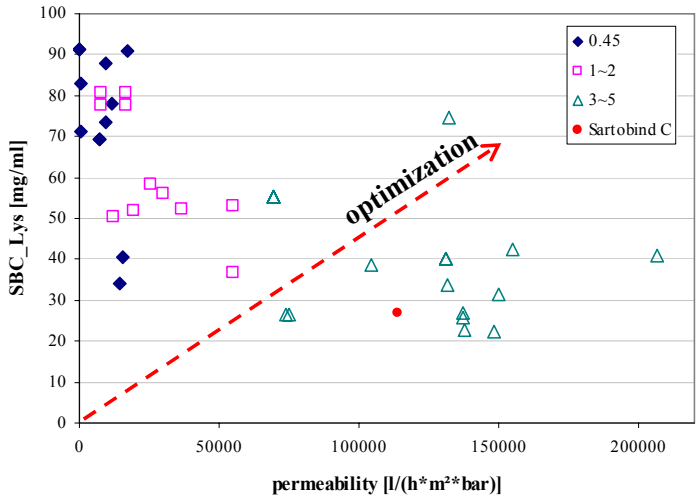


**Figure 6-13.** Overview: Correlation between static binding capacity for Lys and permeability using buffer A.

The trade-off effect can be also eliminated by variation of architecture of grafting layers. SBC of crAAAm grafted membranes indicates good correlation with its permeability, and this has been enhanced with increasing of pore sizes (**Figures 6-14a, b** and **c**). Both 3~5_PAA and 3~5_crAAAm type membrane showed that increasing of irradiation time could improve the SBC without significant loss of permeability (**Figure 6-9c)** in contrast to 0.45 µm membrane in **Figure 6-14a**. Shorter irradiation times (4 min) generates a higher value of permeability for 0.45_crAAAm membrane which is restricted by the small pore size (cf. **Section 6.2.2.**). Increase of the monomer concentration of AA in polymer mixture (approach M2 in **Figure 6-14c**) could bring to negative effect for optimization. Overall, the good correlation in **Figure 6-14** indicates that variation of grafted functional layers and UV irradiation time as well as membrane pore sizes could reduce the trade-off effect between permeability and SBC. Although the impact of dynamic conditions and the property of target molecules has not been taken into account, the results provides promising approach for development of membrane adsorbers.

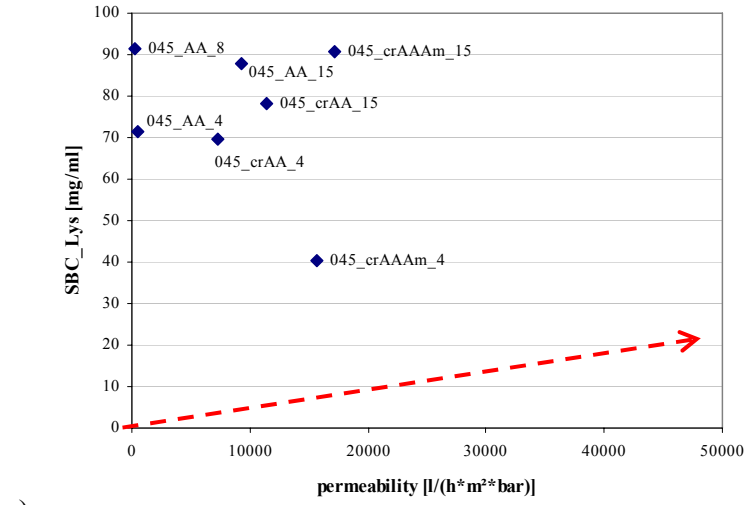


a)

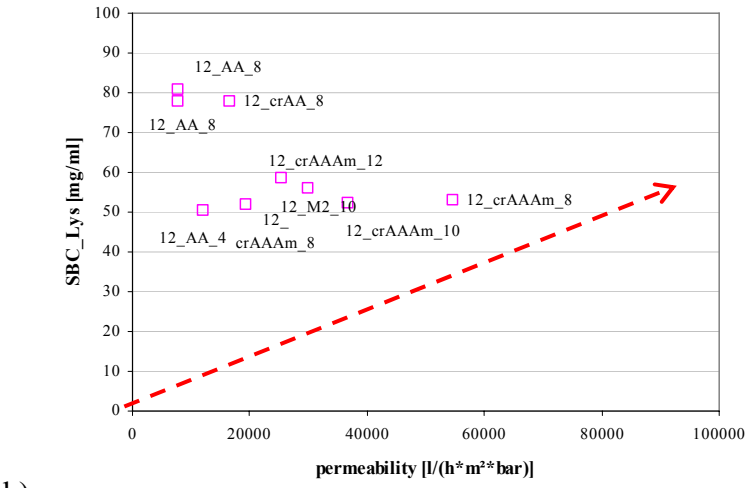


b)

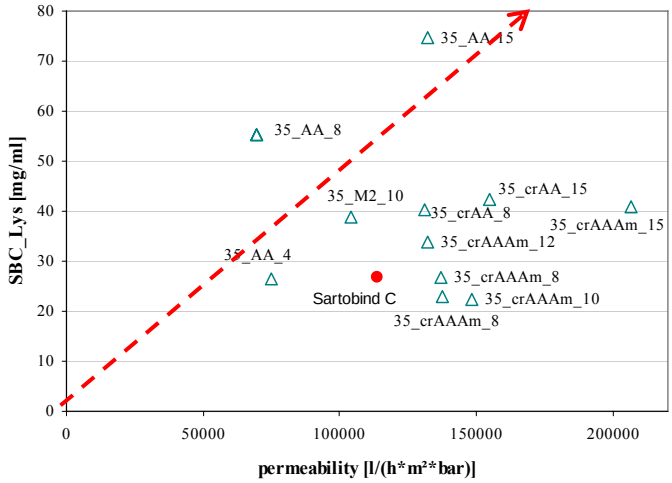


c)

**Figure 6-14.** Correlation between static binding capacity (for Lys) and permeability (using buffer A) for a) 0.45 µm; b) 1~2 µm; c) 3~5 µm membrane.

35_crAAAm_8: 3~5 µm membrane, grafted with crAAAm structure, UV irradiation time was 8 min. M2 presents for 35_crAAAm, grafted polymer concentration was AA: AAm: MBAA=41: 14: 6 g/l.

#### 6.2.3.3. Influence of salt concentration on the grafted polymer architecture

As already discussed in **Section 6.2.2.**, the conformation of the grafted chains depends on the charge of the carboxylic groups which is mainly influenced by pH value and (at pH > $pK_a$) ionic strength of the buffer used (*153*). The salt effect is very pronounced, since counter ions in a high ionic strength solution screen the electrostatic interactions: the grafted chains collapse and this causes the increase of permeability using 1 M salt in the buffer A (**Table 5-3** and **Figure 6-15b**). The change of the permeability by change of the ionic strength was especially large for the PAA type membranes. The membrane 0.45_PAA showed an increase by factor 6.9 from buffer A to buffer A + 1 M NaCl. The effective thickness of the grafted layer in expanded conformation was already relatively close to the pore radius in this case. Similar result was reported for a PAA-grafted 0.4 µm polypropylene membrane (*46*). Less change of the membrane permeability (correlated with effective pore radius) for the membranes with the larger pores, i.e. 1~2_PAA and 3~5_PAA, by factors 4.4 and 1.7, respectively, had been observed. The reduced flexibility of the grafted polymer layer due to the cross-linking resulted in a diminished effect of the salt concentration on the membrane permeability. The susceptibility of permeability to salt concentration is strongly reduced. In contrast, as reported previously, the dilution of charge density in the functional polymer layer using only uncharged spacer AAm without the cross-linker, had caused even larger susceptibility to changes in pH value and salt concentration (*46*).

### 6.2.4. Dynamic membrane performance

In addition to the properties of base membrane (pore size, pore size distribution), the dynamic performance of a membrane adsorber depends on variety of factors like axial dispersion in membrane device through uneven membrane thickness or non-uniformities in membrane porosity as well as the properties of target molecules such as pI value and molecular weight. Commonly, the use of membranes in multiple-layer configuration can reduce axial dispersion to some extent (*31*). However, for membrane adsorbers produced by grafting of a polymer layer on the membrane surface, the influence of the architecture of functional layers must also be taken into consideration (*38*). As described in **Section 5.2.7.**, the analysis of the dynamic binding performance included only the base 1~2 µm and 3~5 µm membranes with PAA and crAAAm grafting architectures. The utilization of the membrane binding capacity is of a high importance as the feed is usually applied only until the concentration of the target solute in the

flow-through reached up to 10% of its initial concentration. The less available binding capacity is utilized, the more membrane area is needed to meet the target load densities which increases the costs of the purification step. High utilization of membrane binding capacity, negligible size exclusion effects and no influence of the flow rate on the dynamic binding capacity are the criteria which can be used to optimize the base membrane structure and the architecture of the grafted polymer layer. In the following section, the dynamic performance of membranes will be discussed with respect of flow distribution in the membranes and mass transfer to binding sites of functional layers as well as the influence of protein properties.

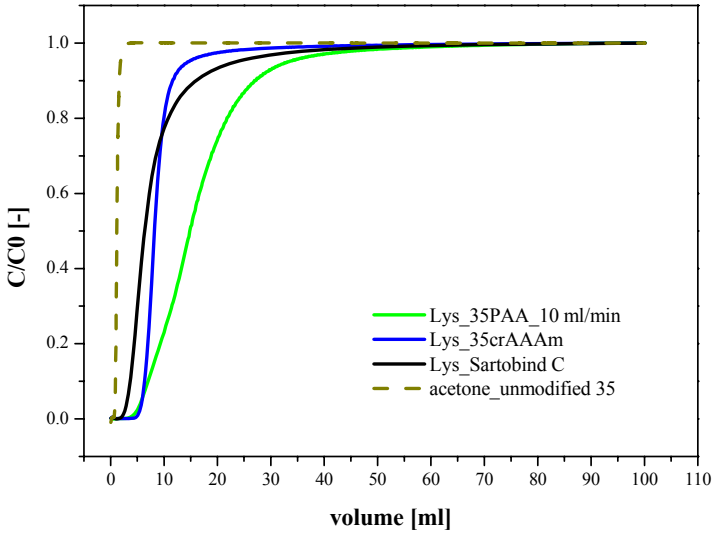


**Figure 6-15.** Breakthrough curves for lysozyme using 3~5 µm membranes at 10 ml/min. 3 membranes were stacked in Scell module. System dispersion was measured using acetone for unmodified membranes.

The slope of the BTCs and the shape of their transition area towards the saturation reveal the contribution of mass transfer and binding kinetics within membrane stack to the system dispersion. The BTC slopes of crAAAm grafted membranes are steeper than for linear PAA membranes (**Table 5-5**)**.** Increasing pore sizes and grafting with cross-linker generally lead to steeper BTCs. System dispersion under non-protein binding conditions presents the non-ideality of the used chromatographic system (**Figure 6-15**). As the membranes with varied functional architecture have been prepared on the same base materials and showed similar affinity for the same protein (**Figure 5-17**), the discrimination among the BTCs of functionalized membranes should have been caused by flow distribution in the membranes. Their contribution to system dispersion depends on the thickness of the functional layer at the same charge density (*33*).

The flow of the feed preferentially takes place through the larger pores of a membrane with a broad pore size distribution, where resistances are relative smaller, and thereby only very little solute will be carried through the smaller pores (*4, 45*). For grafted polymer chains in extended conformation from the pore surface toward to the pore interior only a fraction of binding sites is accessible for target molecules by pore diffusion in the laminar boundary layer, which characterizes transport in the stagnant liquid phase inside a porous stationary phase (*33*). The thicker the functional layer is, the more stagnant liquid is bound within this absorbing hydrogel film of the porous membrane adsorber. The same mechanism occurs for grafted functional chains at high density (or strong confinement in small pores), illustrated in **Scheme 6-2a** for small pores filled with cross-linker grafted functional layer such as 0.45_crAAAm membrane. The initial binding of proteins at the entrance of the functional layer could result in steric hindrance (blocking) and charge repulsion for subsequent protein entering this layer leading to size exclusion for protein binding. 1~2_PAA membrane presented pronounced low binding capacity at a higher flow rate of 10 ml/min (**Table 5-6**). This might be caused by another kind of exclusion effect as illustrated in **Scheme 6-2b**. Such exclusion effect reduces protein binding for linear grafted layer due to high density of functional layers. The Collapse of the grafted layers depend upon saturation of outer surface region with protein. The fact, that this effect is much more pronounced for 1~2_PAA membranes than for 3~5_PAA membranes implies that the low utilization of the binding capacity for membrane 1~2_PAA is probably the consequence of the interplay of pore size exclusion effect of membrane and the properties of functional layer (**Tables 5-6** and **5-8**).

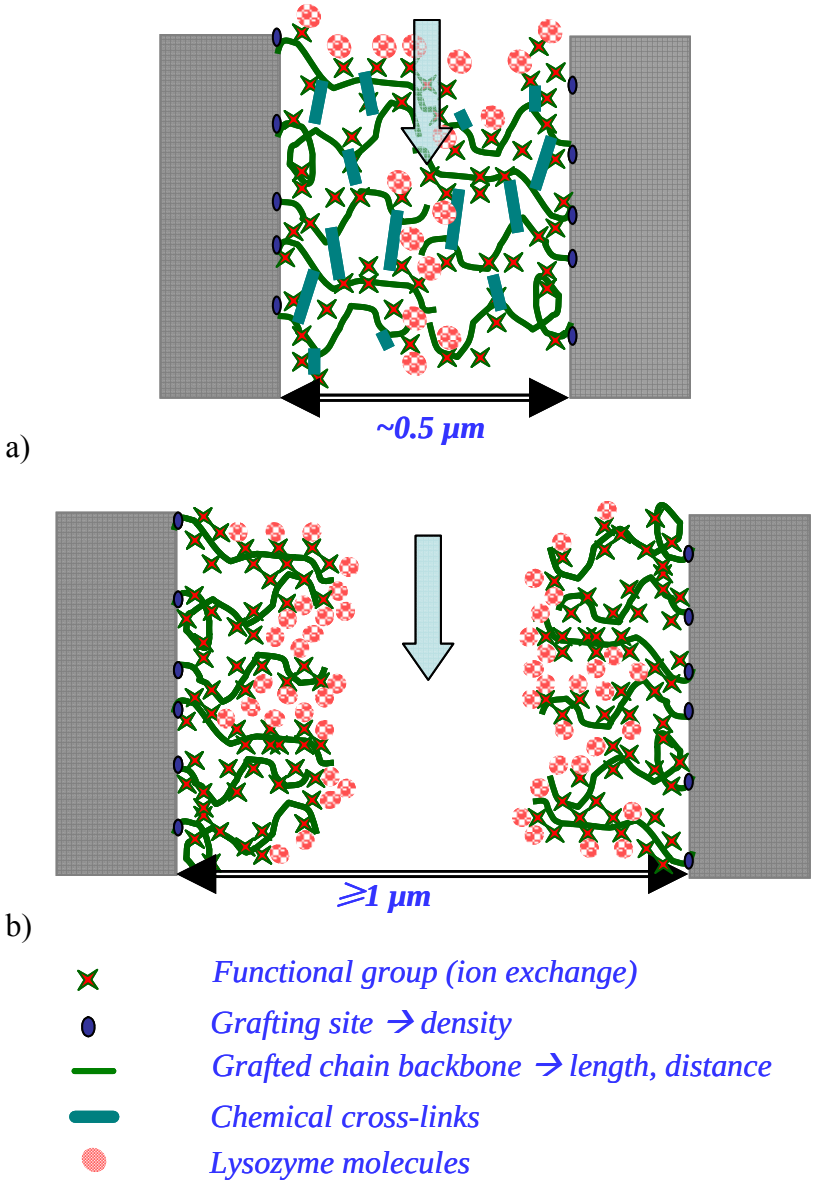


**Schema 6-2.** a) Size exclusion effect for protein binding for pores filled with cross-linker grafted functional layer (membrane 0.45_crAAAm). b) Exclusion effect reduces protein binding for linear grafted layer at high flow rate, due to high charge density and partitial collapse of grafted layer upon saturation of outer surface region with protein (membrane 1~2_PAA).

Furthermore, the different diffusion coefficients of both proteins ($1.48*10^{-11}$ $m^2/s$ for IgG $6.07*10^{-11}$ $m^2/s$ for Lys (*31*) could be another reason for the less steeper BTCs of IgG. Smaller diffusion coefficients lower the degree of a back mixing in the membrane pores where laminar

flow dominates for the larger protein, and therefore lead to a smaller contribution of the axial mixing to system dispersion.

Cross-linking of functional layer restricts the stretching of functional chains to some extend (evidenced by the liquid permeability data in **Section 6.2.3.3.**) facilitating the diffusion processes to the binding site, i.e. the accessibility to solute molecules. This can particularly be observed at high flow rate as in case of membrane 1~2_crAAAm in contrast to uncross-linked membrane 1~2_PAA. On the other hand, the uniform structure of the cross-linking leads to reduced mixing within the membrane, enhances the flow distribution within the membrane stack (**Figures 5-20~22)**, and significantly reduces the contribution of the membrane itself to the total system dispersion. Similarly, the smaller pore size with the narrower pore size distribution (1~2 μm membrane vs. 3~5 μm membrane; **Figure 5-14**) improves the sharpness of BTC. It appears that advanced performance of membrane adsorbers has have been achieved by optimized thickness and charge density of the functional layers.

The images of CLSM in similar depths showed that the location of binding sites of protein well correlated with the chemical modification. Increasing of fluorescence signal intensity and density of protein binding had been observed with decreasing pore sizes (**Figures 5-23** and **5-24**).

Due to absence of washing step after protein injection (**Section 5.2.7.**), the max. dynamic binding capacity values for adsorption are generally equivalent to their SBC values (**Tables 5-3**, **5-6**). These indicate that the binding capacity is independent of flow rates and fast loading should not affect the performance of membranes. However, it should be noted that in the case with larger protein molecules, the influence of flow rates should still be taken into consideration (*154*). The interaction between a protein and an ion exchanger depends on the net charge of the protein, the ionic strength of the buffer, the surface charge distribution of the protein, the nature of particular ions in the liquid phase and the properties of the ion exchanger (*51*). The higher molecular weight (160 kDa) of IgG could be one reason for its higher binding capacity. Because of the higher molecular binding constant of IgG comparing with Lys (**Section 5.2.5.**), the binding of large protein could be performed in multivalent way to form a thicker monolayer on the functional surface (*40*). Similar trends had been observed through mathematical modeling of experimental data of ion-exchange membranes by Yang and Etzel for a small protein $\alpha$－ lactalbumin, and a larger protein thyroglobulin, and further evaluated using three different kinetic approaches (*121*, *125*). The work of Wickramasingehe *et al.* had confirmed this phenomenon by confocal microscopic visualization of protein

adsorption in membrane adsorbers (*99*).

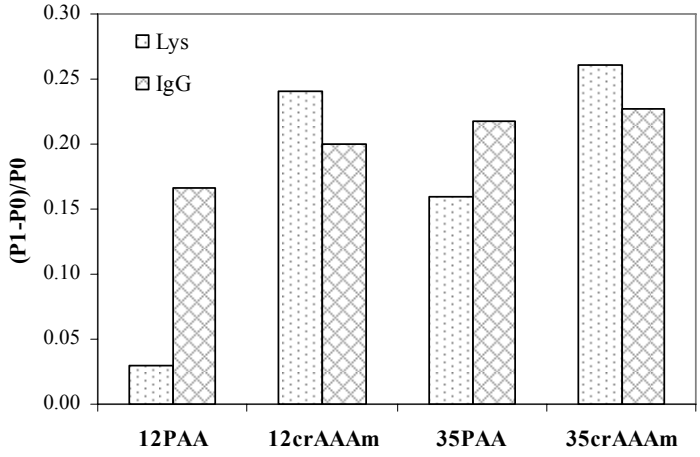


**Figure 6-16.** Transmembrane pressure drop after binding of protein. Data are selected from BTC measurement in SCell module at 10 ml/min.

P0: transmembrnae pressure before protein injection; P1: transmembrnae pressure after protein injection

The novel membrane adsorbers present better performance for the larger protein (IgG). The different pH values of the binding buffers for Lys and IgG should have contribution to the discriminations in the binding behavior of both proteins (*155*). At pH 7.0, which is far away from the pI of Lys (~11.3), and near the pI of IgG (~6), the net charge of IgG is much less than that of Lys. Highly charged Lys is attracted and replaces more counter-ions in the microenvironment of carboxylic groups resulting in a stronger collapse of functional chains (*135*) than IgG. **Figure 6-16** shows the transmembrane pressure drop after protein injection during the BTC determination. For cross-linker grafted membranes, the pressure change for Lys was significant larger than for IgG. However, the case with PAA membranes was in sharp contrast. The self-cross-linking of the linear grafted polymer chains might reduce the respective collapse effect. As consequence, the contact area of functional chains with Lys was probably smaller than for IgG. Due to high charge density 1~2_PAA membrane, and collapses upon saturation of outer surface region with protein (*135*), exclusion effect reduces protein binding for linear grafted layer at high flow rate (**Scheme 6-2b**). Such exclusion phenomenon had been directly observed in bead resins using CLSM (*156*). The size exclusion effect for large proteins could be induced by high charge density of functional chains, and more important, the thickness of functional layers. The approach to reduce the thickness of grafted

layers by using only cross-linker (crAA) has been proven not very successful because a significant size exclusion effect of the larger protein occurred (**Figure 6-12b**). An adapted internal architecture of membrane adsorber with high throughput and improved dynamic binding capacity has been successfully achieved by the combination of both cross-linking and dilution of the charged groups (crAAAm). In such way, a three-dimensional functional layer on the membrane pore surface consists of stabilized binding layers with suitable charge density and a defined mesh size, which is tailored to the size of the target molecules. Pronounced exclusion effect for the Sartobind membranes could be accounted for the structure of their hydrogel functional layers as elucidated above (cf. **Table 5-8)**.

### 6.2.5. Comparison of protein binding capacity and other membrane adsorber system

Diverse works have attempted to improve the binding capacity of membrane adsorbers via more suitable base materials (*17, 21*) or improved surface chemistries (*11, 23, 25, 66, 157, 158*). **Table 6-1** compares the binding capacity of the new prepared membranes with the capacities of other membrane systems in literature. Saito and co-workers (*159*) employed radiation-induced graft polymerization of glycidyl methacrylate and subsequent chemical modifications using diethylamine and ethanolamine to bind protein. Eight anion-exchange porous hollow-fiber polyethylene membranes were packed into a membrane module. Irrespective of the flow-rate, for rates ranging from 10 to 100 ml/min, a DBC value of 67 mg/ml (**Table 6-1**, row 1) had been achieved for BSA.

The modified polysulfone membrane via radiation-induced graft polymerization by Ventura *at al*. (*157*) showed high values of SBC for Lys, ovalbumin, and conalbumin in hollow fiber membranes cartridge. However, trade-off between permeability and SBC had been observed (**Table 6-1**, row 4). Furthermore, DBC values were significant smaller than SBC (0.4~0.6 for Lys).

Affinity membranes made from cellulose, glass fiber and nylon membranes had been modified using various technologies (*66, 158, 160*). Nevertheless, the binding capacities were relatively low (**Table 6-1**, row 2, 9, 10). Bruening and co-workers (*22*) had used a multi-step sequence including surface-initiated controlled atom transfer radical polymerization (ATRP) for preparation of high-capacity affinity membrane adsorbers based on inorganic alumina membranes. These membranes had SBC as high as 150 mg/cm³ (**Table 6-1**, row 5). Nevertheless, DBC was largely limited. During binding of 130 mg/cm³ BSA, the flow rate decreased from 2.4 to 0.9 ml/min. Husson and co-workers (*25*) had used surface-initiated

ATRP for the functionalization of macroporous regenerated cellulose membrane. The grafted brushes had been reported to enhance static and dynamic capacity for Lys (**Table 6-1**, row 6). However, to achieve a fully controlled grafting via ATRP requires more efforts which may be hard to implement in large technical scale.

The specific surface area of membranes is essentially lower than of resin-based bead. Wessling and co-workers (*21*) had attempted to expand the specific surface area by incorporation of ion-exchange resins into an EVAL porous matrix. The achieved binding capacity values were pronounced. However, the membranes showed more pronounced flux dependent adsorption behavior in comparison with Sartobind membranes (**Table 6-1**, row 7). The available surface of electrospun cellulose acetate nanofilbers (diameter of 1~2 μm) (*17*) has been reported as much as two orders of magnitude lager than for commercial regenerated cellulose membrane, and its 10% DBC (at 1 ml/min) had reached 26.9 mg/g (**Table 6-1**, row 8).

Photo-initiated graft copolymerization has been successfully applied as an easy and robust approach for the preparation of high capacity ion exchange membranes for polypropylene (*20, 23, 46*) and regenerated cellulose (*47*). In the work of Ulbricht and Yang (*23*), highest binding efficiency had been achieved by entrapping method for photo initiator immobilization compared with the adsorption method (**Table 6-1**, row 11). He and Ulbricht (*20, 79*) prepared membranes by synergist immobilization method. The light cross linker grafted anion exchange membranes had shown enhanced permeability and maintained high protein binding capacity for over 80 mg/ml for BSA (**Table 6-1**, row 12).

The adsorption method of UV-initiated heterogeneous copolymerization has been successfully employed for flat sheet regenerated cellulose membranes in this work with respective of the influence of membrane functional architecture. Although the specific area of flat sheet cellulose membrane is relatively lower (**Figure 5-2**) than for PP membranes (*79*), the binding capacity of 1~2_PAA membranes have reached SBC values of 62.6 mg/ml and 66.0 mg/ml, and max. DBC values of 73.1 mg/ml and 77.5 mg/ml for Lys and IgG, respectively. 10% DBC value for the big protein IgG has even reached 37 mg/ml at 10 ml/min (**Table 6-1**, row 13).

**Table 6-1.** Comparson of protein binding capacity of new prepared membrane adsorbers with other membrane systems

| base membrane | functional group | protein | SBC [mg/ml] | (max.) DBC [mg/ml] | reference |
|---|---|---|---|---|---|
| polyethylene | DEA-EA | BSA | - | 67 | (*159*) |
| cellulose | Iminodiacetate-$Cu^{2+}$ | BSA | 4.2 | - | (*66*) |
| cotton cellulose | PVBT | BSA | - | 40 mg/g | (*161*) |
| polysulfone | GMA-DEGMA | Lys/ ovalbumin/ conalbumin | 140/88/66 | 0.65 of SBC | (*157*) |
| alumina | PHEMA | BSA | 150 | 133 | (*22*) |
| regenerated cellulose | PAA | Lys | 98.5 | 72.1 | (*25*) |
| EVAL matrix | Lewatit CNP80 WS | Lys | 147 | 63 | (*21*) |
| regenerated cellulose electrospun nanofilbers | DEAE | BSA | 40 mg/g | (10% DBC) 26.9 mg/g | (*17*) |
| glas fiber | trypsin and papain immobilized | BSA | - | 8.6 | (*158*) |
| nylon | VBTAC | IgG | 9.8 | - | (*160*) |
| polypropylene | PAA | Lys | - | 62* 0.5 ml/min | (*23*) |
| polypropylene | METMAC | BSA/ Trypsin | >80/120 | 10% more than SBC | (*20*) |
| regenerated cellulose | PAA | Lys/ IgG | 62.6/66.0 | 73.1/77.5 10% DBC: 24/37 | this work |

**Abbreviation**: DEA –EA (diethylamino- Ethanolamino); DEAE (diethylaminoethyl); EVAL (copolymer of ethylene and vinyl); GMA- DEGMA (glycidyl methacrylate- diethyleneglycol dimethacrylate); METMAC (Poly(2-(methacryloyloxy)ethyl)-trimethylammonium chloride)); PHEMA (poly(2-hydroxylethyl methacrylate)); PVBT (Poly(vinylbenzyltrimethylammonium chloride)); VBTAC (vinylbenzyltrimethylammonium chloride)

Overall, in terms of utilization of binding capacity, size exclusion effects and influence of the flow rates on dynamic performance of membranes, 1~2 µm and 3~5 µm membranes with crAAAm-type grafted layer provided competitive performance for both small (Lys) and large (IgG) proteins (**Table 5-8**). However, at about the same mass of the grafted polymer per area of the pore walls, 1~2 µm membrane has achieved higher binding capacity under static and dynamic operation conditions. This could result from its narrower pore size distribution and concomitant higher utilization of the pore volume (cf. **Section 6.2.5.1.**). The use of macroporous membrane with a narrow membrane pores size distribution coupled with effective flow distributor can minimize axial dispersion and provide uniform utilization of all active sites (*45*). The performance of the 0.45 µm membrane is limited by its too small pore size.

In order to overcome the convective mass transfer limitation of transporting the target to the surface of the functional layers, i.e. the residence time $t_R (=\frac{L}{u})$ of the liquid in the membrane must greatly exceed the time scale $t_f (=\frac{d_m^2}{4D})$ for film diffusion, where L is the membrane stack thickness, u is the flow rate, $d_m$ is the membrane pore size and D is diffusion coefficient of the protein. Suen and Etzel recommended that for maximization of binding capacity, the optimum pore size of membrane matrix should be less than ~15 µm (*32, 162*). They further suggested that membranes with a pore size of about 1 µm can be used to eliminate mass transfer limitations for large proteins when residence times are about one second (*31, 163*). This is justified for 1~2 µm membrane with crAAAm structure.

## 6.3. Effect of membrane module design on the efficiency of membrane adsorber process

The earlier breakthrough by using CIM module (**Figure 5-26**) results in low values of 10% breakthrough. This could be the consequence of smaller volume of membranes stacked in module comparing with SCell module (CIM module: 0.11 $cm^3$; SCell module: 0.35 $cm^3$). The striking discrepancy between **Tables 5-6** and **5-10** reveals that the difference in the design of membrane modules should be one reason for the low utilization of dynamic binding capacity measured using CIM module.

Model based quantitative characterization of the internal flow distribution within membrane modules was based on a novel radial multi-zone flow model (**cf. Section 2.8.2**.). The internal volumetric flow distribution fitted with two zones within the SCell module has been explored in dependence upon the membrane pore sizes and flow rates (**Figure 6-17**). This distribution is expressed as the ratio of volumetric flow through zone 2 vs. zone 1. Due to $f \sim \frac{1}{\tau}$ this ratio also represents the residence time taken in zone 1 vs. in zone 2. High flux ratios indicated that the residence time of molecules flowing through peripheral regions is longer than through the central region. The smaller the flux ratio is, the more uniform the flow distribution is within membrane module.

**Figure 6-17** shows a decreasing trend of flux ratios with increasing membrane pore sizes and flow rates for lysozyme. Only the ratios for 1~2 μm and 3~5 μm membranes are at the same level for a flow rate of 5 ml/min. An increasing flow rate can lead to more uniform flow distribution in the channels before and after the membrane stack (*26, 28*). The dependence on the membrane pore sizes can be understood by the resistance differences due to membrane structure. The 0.45 μm membrane has a more dense morphology than the others (cf. **Figure 5-23**). However, these dependencies were only pronouncedly observed for acetone at a flow rate of 1 ml/min.

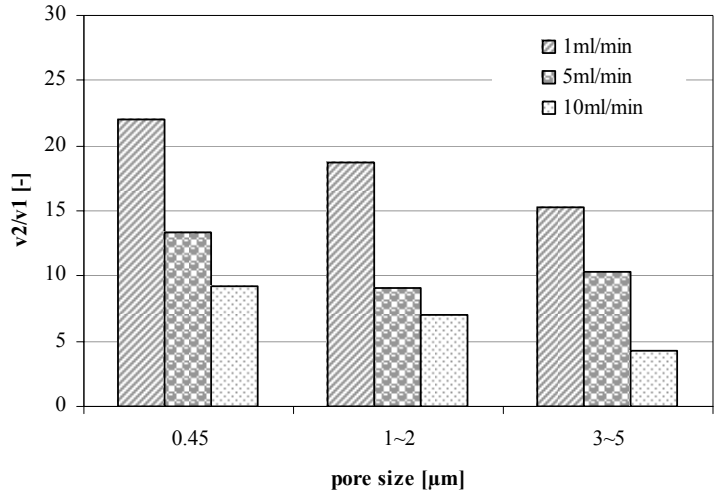


a)

**Figure 6-17.** Ratio of volumetric flow through zones 2 and 1 in dependence of membrane pore sizes and flow rates of test tracers. Breakthrough curves were measured using Lys in Scell module.

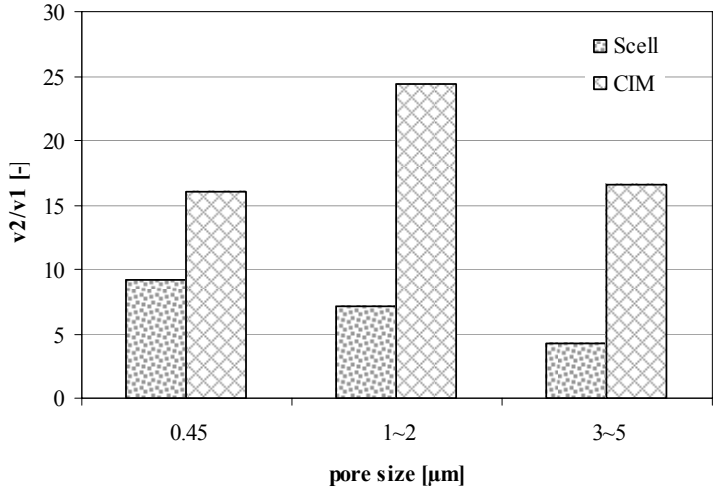


**Figure 6-18.** Comparison of volumetric flow ratio through zones 2 and 1 in terms of membrane pore sizes in SCell module and CIM modules. The breakthrough curves were measured using Lys at 10 ml/min.

Further analysis of the flow distribution in both zones is plotted in **Figure 6-18** for both membrane modules. The breakthrough curves were measured at 10 ml/min using lysozyme. Suitable curve fittings were found using two zones. The residence time taken to reach the peripheral region was pronouncedly higher in CIM module than in Scell modules. No tendency as function of the pore sizes could be identified for the CIM module. Within the CIM module, flow permeates preferentially through the central region of the porous discs, and only a small fraction of the fluid flows through the peripheral region. The solute flow paths have therefore more variations in the CIM module, and this can be well judged by comparison of the fractions of PFR and CSTR for both modules under the same conditions (see **Figure 6-19**). While the contributions of PFR and CSTR were comparable for the Scell module in **Figure 6-19a** (with ~0.6 ml for PFR and ~0.7 ml for CSTR; **Table 5-12**), the description of the CIM module was essentially governed by the CSTR network as shown in **Figure 6-19b** (with ~0.2 ml for PFR and ~1.5 ml for CSTR; **Table 5-12**). The flow channels in the Scell module enable easier access of fluid to the peripheral region of the membrane stack leading to a more uniform distribution of solute and subsequently better utilization of this region.

Until now, the striking discrepancy of dynamic performance between the both membrane modules (cf. **section 5.3.**) can be well explained. The design of CIM module generates steeper BTC than SCell module (**Tables 5-5** and **5-9**). However, it suffers from earlier break though, and therefore smaller utilization of 10% DBC. The smaller effective diameter of the CIM module enhances this effect. The short-cut flow through generates quick saturation only in the central region of the stack, and leads to premature breakthrough. Consequently, lower dynamic capacity values for batch I membranes are generated by unsuitable design of CIM membrane module.

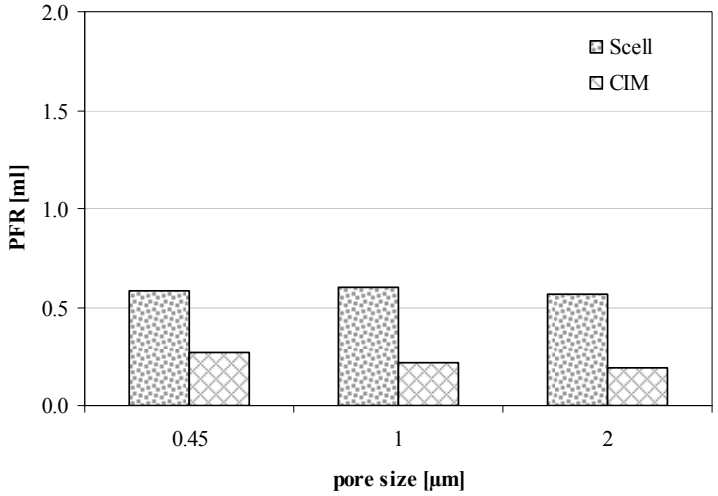


a)

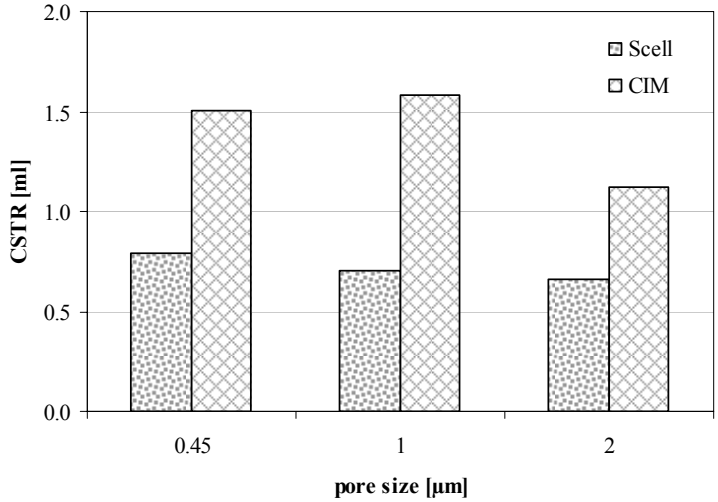


b)

**Figure 6-19.** Respective fraction of PFR and CSTR volumes (average over 0, 1 and 2 zones) for Scell and CIM modules in terms of membrane pore sizes. The breakthrough curves were measured at 10 ml/min using 2 mg/ml lysozyme under non-binding conditions.

# 7. Conclusion and outlook

Commercial macroporous weak cation exchange membrane adsorbers based on regenerated cellulose membranes have been characterized with help of different microscopic techniques in combination with static and dynamic protein binding experiment. Due to intrinsic difficulties with investigations of the porous membranes in completely wet state in the ESEM, the effects of water uptake and release from the gas phase have been investigated: While the macropore network remained unchanged, smaller fibers within the macropores showed a significant volume change and mobility. Using staining of the membrane matrix in combination with CLSM, the pore morphology in completely wet state and also inside the membrane volume can be imaged. However, the three-dimensional resolution (> 1 $\mu m^3$) and depth of penetration in the sample (up to 20 μm) are limited. The visualization of protein binding was possible, and significant binding in the pore volume but not extending throughout the entire diameter of the macropores has been confirmed. For the first time, the dynamic protein binding in macroporous membrane adsorbers has been monitored *in situ* using CLSM and qualitatively analyzed.

Based on the knowledge obtained from advanced microscopy in combination with more conventional binding experiments, novel weak cation-exchange membrane adsorbers with different pore sizes have been prepared via UV-initiated grafting of tailored functional polymeric ion-exchange layers on macroporous supports made from stabilized regenerated cellulose, and their improved separation performance has been related to the key parameters such as matrix pore structure and architecture of grafted functional polymer layers. The influence of the membranes and membrane modules on mass transport has been discussed. The linear grafted PAA structure reveals pronounced trade-off between permeability and static binding capacity of the functional membrane, whereas, the magnitude depends upon the pore size of the base membranes. This trade-off effect has partially been overcome by adapted architecture of the grafted functional layer achieved by the introduction of suited uncharged groups and stabilization of binding layer by chemical cross-linking (crAAAm architecture). The susceptibility of the membrane adsorber to the change in salt concentration has been minimized by such adapted architecture. Also, the utilization of available binding sites at 10% breakthrough has been significantly improved to about 70%, in contrast to the grafted linear PAA, where the utilization was only between 20~40% for Lys. There was no considerable size exclusion effect for large proteins due to mesh size of functional cross-linked layers. As the permeability of 0.45 μm membranes is strongly restricted by its relative small pore size, the

base 0.45 µm membrane is not suitable for grafting of AA functional layer to achieve porous membrane adsorber with acceptable dynamic performance. Blocking effect at the entrance of functional layers was observed for membranes with linear grafted PAA (e.g. 1~2_PAA), which have high charge density of polymer chains and large thickness of functional layer. In this case, the accessibility of further binding sites for protein is hindered. Such blocking effect has been successfully overcome by the adapted grafted layer architecture (e.g., membrane 1~2_crAAAm). In contrast, 3~5 µm membranes were less susceptible to high flow rate, but their wide pore size distribution as compared to the 1~2 µm membranes has disadvantages with respect to dynamic binding capacity at the same mass of grafted polymer per area of pore wall. Otherwise, 1~2 µm and 3~5 µm membranes have presented similar performance in terms of utilization in binding capacity, size exclusion effect for large protein and influence of high flow rate. Investigation of system dispersion based on breakthrough curves has confirmed that the adapted grafted layer architecture has drastically reduced the contribution of the membrane to total system dispersion. The optimum pore structure of base membranes (here 1~2 µm) in combination with the best suited architecture of functional layers identified in this study (crAAAm) has yielded maximum dynamic binding capacities of 38 mg/ml for Lys and 36 mg/ml for IgG, and 10% breakthrough capacities of 24 mg/ml for Lys and 23 mg/ml for IgG, all at 10 ml/min.

The dynamic separation performance of newly prepared membranes has been compared by using two different membrane modules, CIM® and Sartorius® custom membrane module (SCell module). It has been shown that the average utilization of maximum binding capacity of the membranes was improved by approx. 60% for maximum dynamic binding capacity and 10% breakthrough for SCell module in comparison with CIM module. The influence of membrane modules is therefore very critical. Subsequently, the internal flow distribution within two membrane modules has been quantified based on a novel radial multi zone flow model for flat sheet chromatographic membrane modules (*118*). The model accounts for commonly observed inhomogeneous radial flow distributions within such membrane modules. Internal flow distributions of the two small scale membrane modules have been quantified and characterized by the number of radial zones and by the fractional volumetric flow through these zones. The void volumes estimated by curve fitting were in good agreement with earlier experimental results for acetone as completely inert tracer. The apparent increase of void volume for the CIM module with a protein tracer can be explained by non-specific binding to the porous polymer discs used for flow-distribution. The internal flow paths within the Scell module can be well described by two radial zones. The ratio of volumetric flow through the

two zones responded systematically to the increase of membrane pore size and flow rate. In comparison, one or two radial zones were required for describing the internal flow paths of the CIM module depending on the test tracers. The system dispersion was essentially dominated by the CSTRs used for modeling the preferential flow through the central region of membrane module. The channels for flow distribution within the Scell module significantly improve the utilization of peripheral regions of the membrane stack, consequently delay the onset of breakthrough, and ultimately reduce system dispersion. Different binding characteristics in distinct spatial regions in flow-through membrane module had been observed during *in situ* visualization of protein binding experiment. Perspectively, flow-through module could be improved in terms of the minimum dead volume and homogeneous flow distribution within module.

Continuous photografting of membranes and membrane adsorber in large scale has become interesting for industry. Zhang and Ranby had developed a process that can be used for continuous photografting of polymer films and fibers (*164*). A flow chart of such process setup compatible with functionalization of membrane adsorber is shown in **Figure 7-1**. In the presoaking step, membrane roll is fed continuously at a velocity of 1~10 m/min into a chamber containing monomer solution and initiator such as BP, the membrane will be subsequently dried for immobilization of photoinitiator, coated with monomers, and travels to UV-lamp chamber for irradiation. During this procedure, the membrane is covered between two films (PET) to maintain a minimal amount of coated monomer. If the residence time in coating tank is not adequate, optional precoating monomer solution can be performed before coating procedure. The amount of time the membrane takes to travel from the presoaking solution to the area where it is irradiated with a UV lamp is controlled, allowing the diffusion of the monomer and initiator into the amorphous regions of the polymer. The irradiation time is regulated by varying the motor speed of transporter and irradiation zone. After irradiation, the membrane will be extracted and dried.

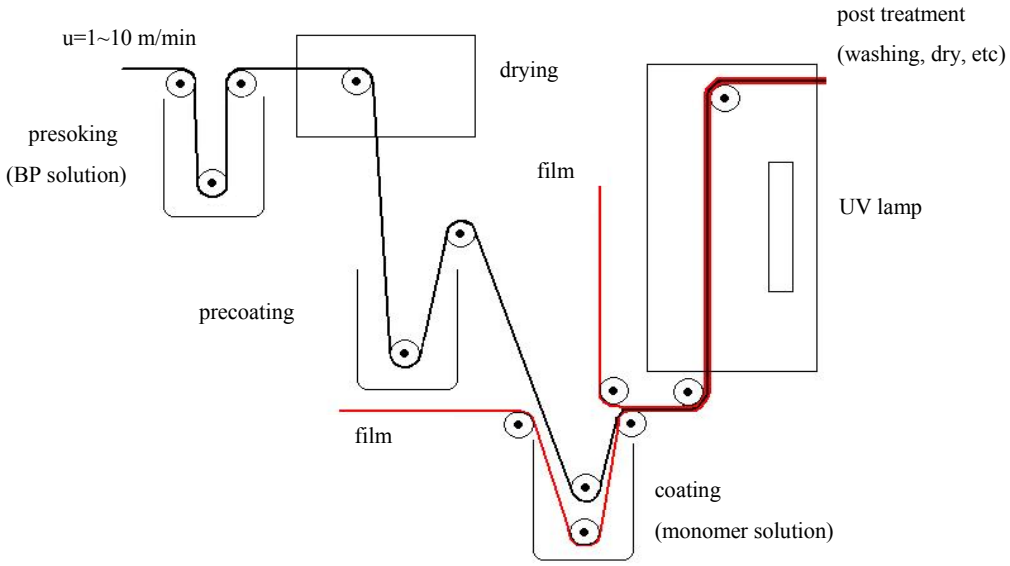


**Figure 7-1.** Flow chart of a continuous photo-grafting procedure for membrane adsorber manufacturing.

The screening of preparation procedures as described in **Section 4.3**. has been carried out in terms of the solution amount and residence time in respective tanks. It had been found that the presoaking time with BP solution can be limited to 5 min, however, a drying procedure for immobilization of BP is required (*165*). A detailed study with help of Design of Experiment could provide more valuable information for the fabrication of membrane adsorber in industrial scale. The characterization of newly prepared membranes via UV-initiated grafting polymerization has provided the basis for a promising strategy for further optimization towards high performance macroporous membrane adsorbers. Combining with improved chemistry of functional layers, membrane adsorbers will be more comparable to conventional chromatographic column.

# 8. Appendix

## 8.1. Preparation of the buffers

a. 10 mM potassium phosphate buffer, pH 7.0 is diluted from 2 M concentrated buffer.

For preparation of 2M potassium phosphate buffer, at first, a basic solution (348.4g $K_2HPO_4$ in 1 liter deionized water) and an acidic solution (272.2 g $KH_2PO_4$. $H_2O$ in 1 liter deionized water, heated at approx. 70°C) are prepared. Basic solution is added to the acidic solution to adjust the pH value to pH 7.0.

b. 20 mM Sodium acetate, pH 5.0.

0.0132 mol $CH_3COONa$ is dissolved in 900 ml deionized water, then pH value is adjusted by acetic acid to pH 5.0. The total volume is filled with deionized water to 1 liter.

c. Sodium phosphate buffer, pH 7.0 *(volume: 1 liter)*

| Ionic strength | $Na_2HPO_4$ [mM] | $NaH_2PO_4$ [mM] | NaCl [g] |
|---|---|---|---|
| 6 mM | 1.6 | 1.7 | |
| 20 mM+50 mM NaCl | 10.75 | 9.24 | 0.496 |
| 10 mM +500 mM NaCl | 6.6 | 3.3 | 27.91 |

d. 0.1 M Sodium carbonate buffer, pH 9.3

8.4 g $NaHCO_3$ is dissolved in 900 ml deionized water. The solution is then titrated with NaOH to pH 9.3. The total volume is filled with deionized water to 1 liter.

## 8.2. Resolution of CLSM system (*90*)

The limit of lateral resolution of a CLSM can be estimated using the point objects method of Inoué (*90*) (cf. (*97*)).

lateral resolution: $d_{airy} = 1.22 * \frac{\lambda_0}{NA_{obj}}$ (8-1)

where $d_{airy}$ is expressed as the distance in the specimen plane. $\lambda_0$ is the wavelength of light in vacuum and $NA_{obj}$ is the numerical aperture of the objective lens, here $NA_{obj}$=1.3.

axial resolution (z-axial): $Z_{\min} = \frac{4\lambda_0 * n}{(NA_{obj})^2}$ (8-2)

$Z_{\min}$ corresponds to the distance by which the microscope objective has to be raised in order to focus the first intensity minimum observed along the axis of the 3D diffraction pattern instead of the central maximum. The refraction index for immersion oil $n_{oil}$=1.5616. The calculated lateral resolution of CLSM system for investigation of new prepared membranes was 0.45 µm for 488 nm, 0.58 µm for 633 nm. Axial resolution is 1.8 µm for 488 nm, 2.3 µm for 633 nm.

## 8.3. Images of membranes

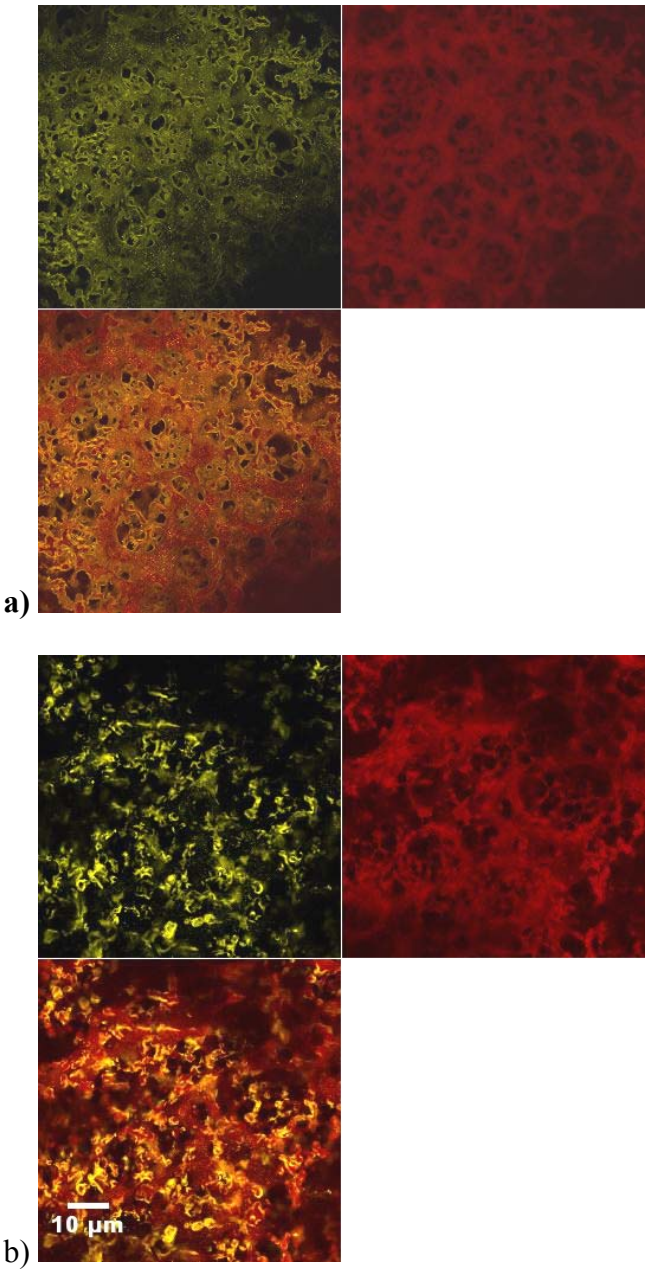


**Figure 8-1.** CLSM images of top side of Sartobind membranes. a) Sartobind S, 10 µm depth; b) Sartobind C, 9 µm depth, from the outer side of membranes.

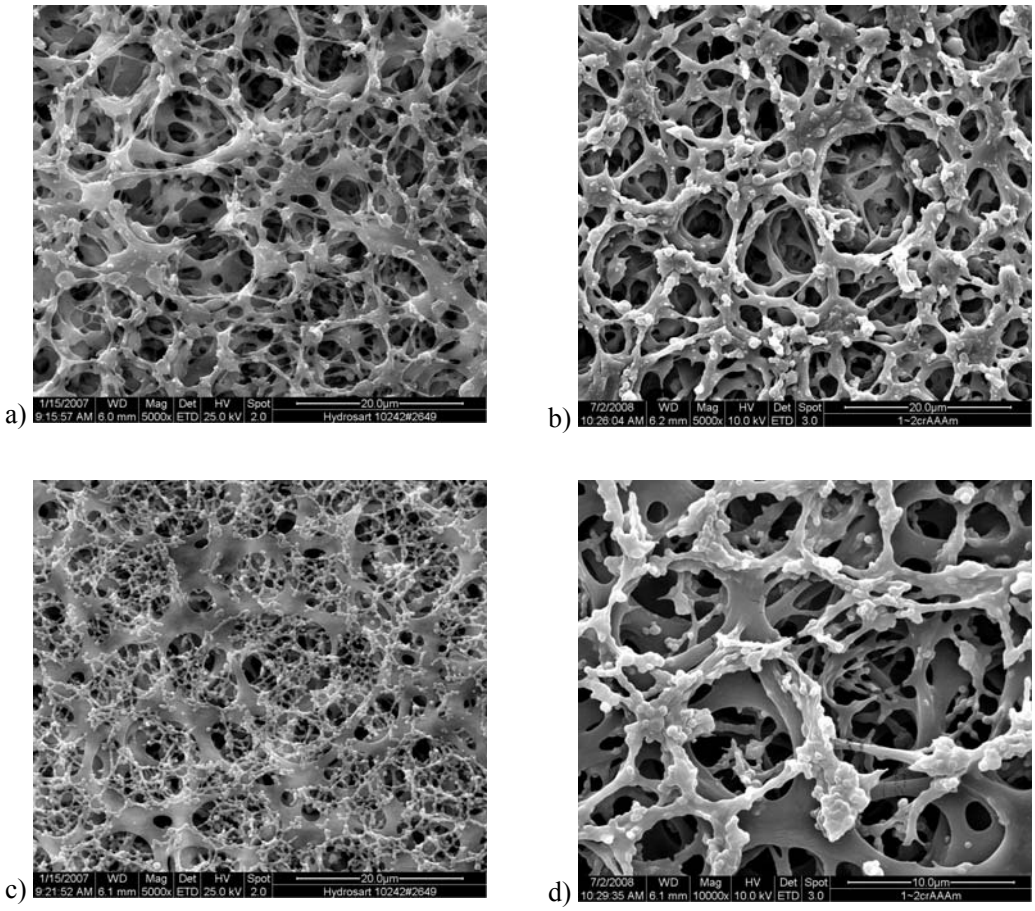


**Figure 8-2.** SEM images of 1~2 µm membranes. a) Hydrosart 1~2 µm, top side, magnification 5000; b) modified 1~2_crAAAm, DG 1.6, top side, magnification 5000; c) Hydrosart 1~2 µm, bottom side, magnification 5000; d) modified 1~2_crAAAm, DG 1.6, bottom side, magnification 10000.

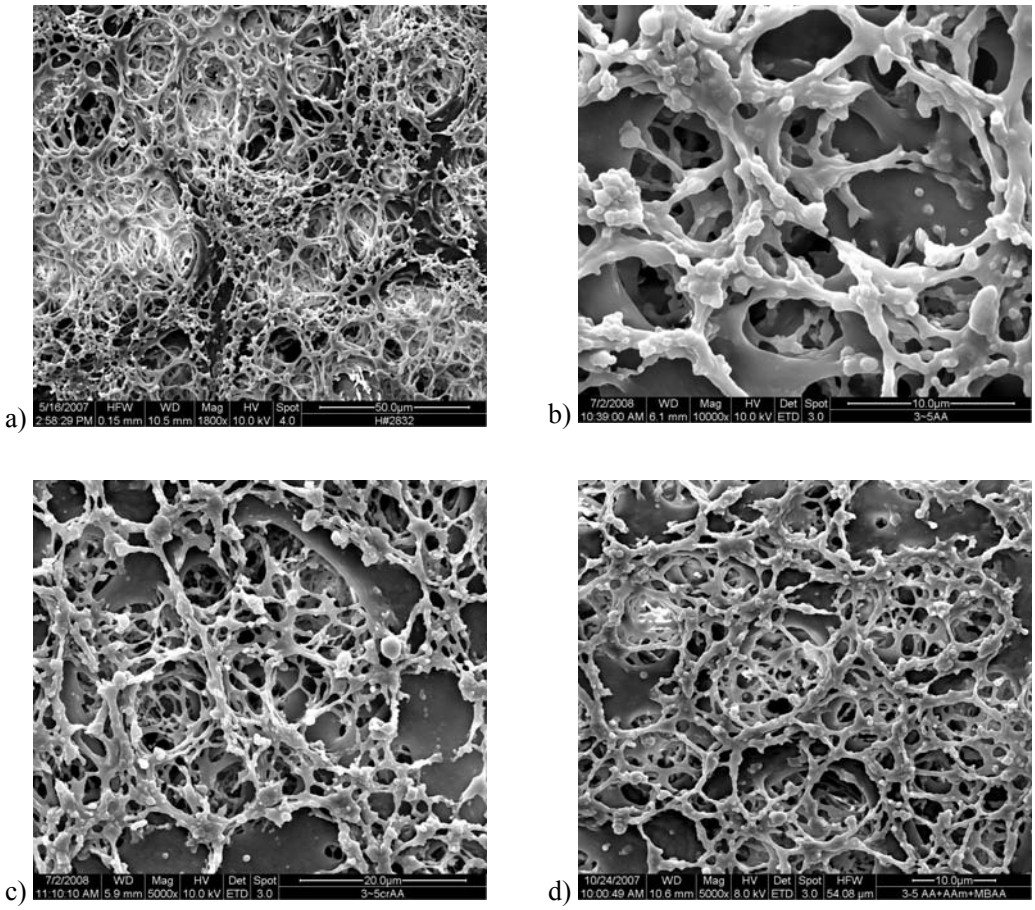


**Figure 8-3.** SEM images of bottom side of 3~5 µm membranes, a) Hydrosart 3~5 µm, magnification 1800; b) modified 3~5_PAA, DG 1.5, magnification 10000; c) modified 3~5_crAA, DG 1.8, magnification 5000; d) modified 3~5_crAAAm, DG 1.8; magnification 5000.

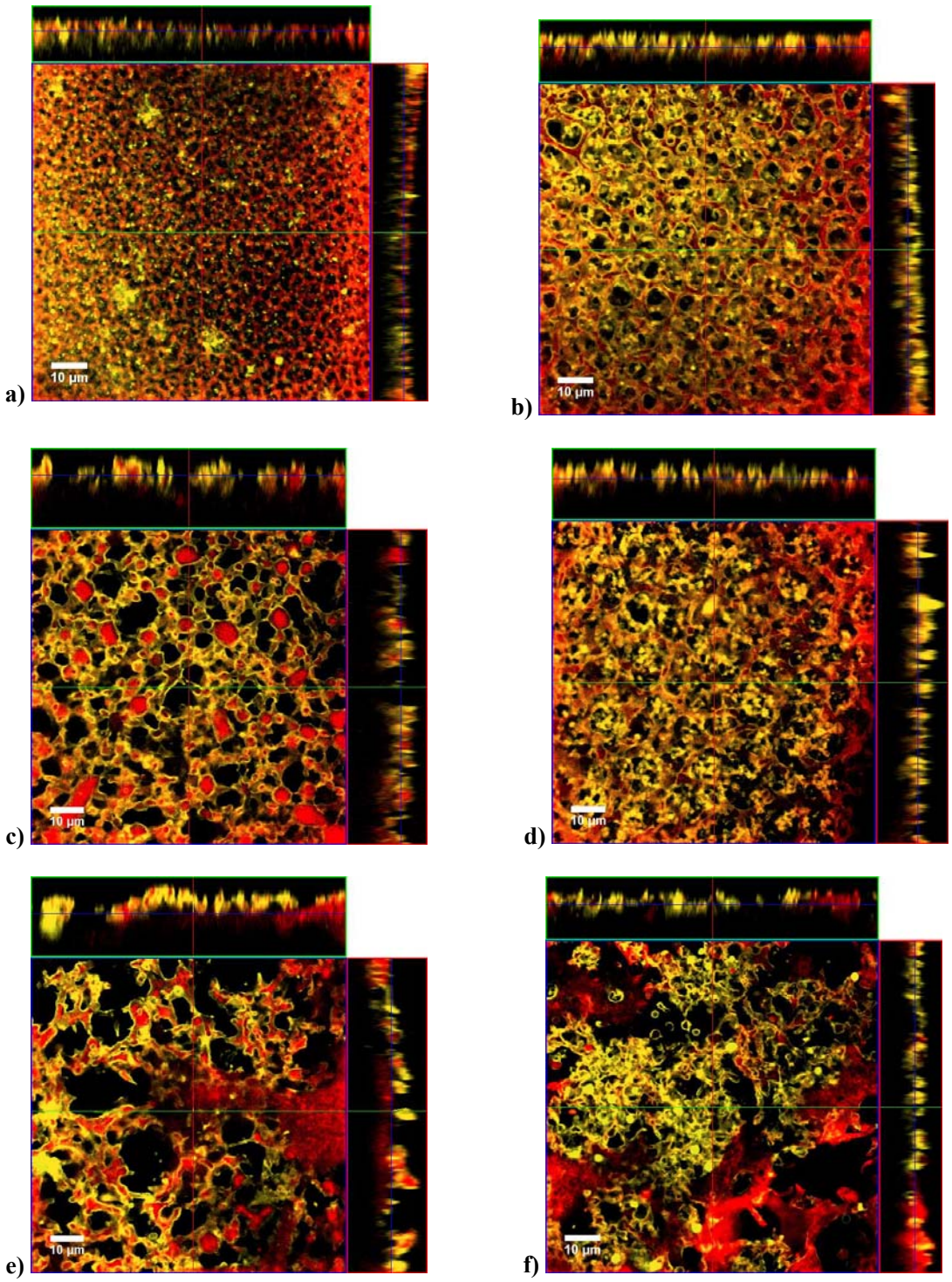


**Figure 8-4.** Overlapped CLSM images of labeled protein binding (633 nm) to stained membrane (488 nm) for crAAAm membranes. a) 0.45_crAAAm, bottom side, 9 µm depth; b) 0.45_crAAAm, bottom side, 9 µm depth; c) 1~2_crAAAm, bottom side, 10 µm depth; d) 1~2_crAAAm, top side, 10 µm depth; e) 3~5_crAAAm, bottom side, 12 µm depth; f) 3~5_crAAAm, top side, 12 µm depth; Dimension of the images is 92.1* 92.1 $\mu m^2$.

## A. References


1. Roque, A. C. A., Lowe, C. R., and Taipa, M. A. (2004) Antibodies and genetically engineered related molecules: production and purification, *Biotechnol. Prog. 20*.

2. Zhou, J., Tressel, T., Gottschalk, U., Solamo, F., Pastor, A., Dermawan, S., Hong, T., Reif, O., Mora, J., Hutchison, F., and Murphy, M. (2006) New Q membrane scale-down model for process-scale antibody purification, *J. Chromatogr. A 1134*, 66.

3. Gottschalk, U. (2008) Bioseparation in antibody manufacturing: the good, the bad and the ugly, *Biotechnol. Prog. 24*, 496.

4. Roper, D. K., and Lightfoot, E. N. (1995) Separation of biomolecules using adsorptive membranes, *J. Chromatogr. A 702*, 3.

5. Charcosset, C. (1998) Purification of proteins by membrane chromatography, *J.Chem. Technol. Biotechnol. 71*, 95.

6. Klein, E. (2000) Affinity membranes: a 10-year review, *J. Membr. Sci. 179*, 1.

7. Phillips, M., Cormier, J., Ferrence, J., Dowd, C., Kiss, R., Öutz, H., and Carter, J. (2005) Performance of a membrane adsorber for trace impurity removal in biotechnology manufacturing, *J. Chromatogr. A 1078*, 74.

8. Demmer, W., and Nussbaumer, D. (1999) large-scale membrane adsorbers, *J. Chromatogr. A 852*, 73.

9. Knudsen, H. L., Fahrner, R. L., Xu, Y., Norling, L. A., and Blank, G. S. (2001) Membrane ion-exchange chromatography for process-scale antibody purification, *J. Chromatogr. A 907*, 145.

10. Ulbricht, M. (2006) Advanced functional polymer membranes, *Polymer 47*, 2217.

11. Kawai, T., Saito, K., and Lee, W. (2003) Protein binding to polymer brush, based on ion-exchange, hydrophobic, and affinity interactions, *J. Chromatogr. B 790*, 131.

12. Zeng, X. F., and Ruckenstein, E. (1999) Membrane chromatography: preparation and applications to protein separation, *Biotech. Prog. 15*, 1003.

13. Tennikova, M. B., Belenkii, B. G., and Svec, F. (1990) High-Performance Membrane Chromatography. A Novel Method of Protein Separation *J. Liq. Chromatogr. 13*, 63.

14. Molinari, R., Torres, A. S., Kipatrick, P. K., and Carbonell, R. G. (1990) Simultaneous ultrafiltration and affinity sorptive separation of proteins in a hollow fiber membrane module, *Biotech. Bioeng. 36*.

15. Shiosaki, A., Goto, M., and Hirose, T. (1994) Separation of Water/Ethanol Vapor Mixtures through Chitosan and Crosslinked Chitosan Membranes *J. Chromatogr. A 679*, 1.

16. Suen, S. Y., Caracotsios, M., and Etzel, M. R. (1993) Sorption kinetics and axial diffusion in binary solute affinity membrane bioseparations, *Chem. Eng. Sci. 48*, 1801.

17. Zhang, L., Menkhaus, T. J., and Fong, H. (2008) Fabrication and bioseparation studies of adsorptive membranes/felts made from electrospinn celloluse acetate nanofibers, *J. Membr. Sci. 319*, 176.

18. Tennikov, M. B., Gazdina, N. V., Tennikova, T. B., and Svec, F. (1998) Effect of porous structure of macroporous polymer supports on resolution in high-performance memrbane chromatography of proteins, *J. Chromatogr. A 798*, 55.

19. Avramescu, M. E., Borneman, Z., and Wessling, M. (2008) Particle-loaded hollow-fiber membrane adsorbers for lysozyme separation, *J. Membr. Sci. 322*, 306.

20. He, D. M., and Ulbricht, M. (2008) Preparation and characterization of porous anion-exchange membrane adsorbers with high protein-binding capacity, *J. Membr. Sci. 315*, 155.

21. Saiful, Z. B., and Wessling, M. (2006) Enzyme capture and concentration with mixed matrix membrane adsorbers, *J. Membr. Sci. 280*, 406.

22. Sun, L., Dai, J., Baker, G. L., and Bruening, M. L. (2006) High-capacity, protein-binding membranes based on polymer brushes grown in porous substrates, *Chem. Mater. 18*, 4033.

23. Ulbricht, M., and Yang, H. (2005) Porous polypropylene membranes with different carboxyl polymer brush layers for reversible protein binding via surface initiated graft-copolymerization, *Chem. Mater. 17*, 2622.

24. Tsuneda, S., Saito, K., Furusaki, S., and Sugo, T. (1995) High-throughput processing of proteins using a porous and tentacle anion-exchange membrane, *J. Chromatogr. A. 689*, 211.

25. Singh, N., Wang, J., Ulbricht, M., Wickramasinghe, S. R., and Husson, S. M. (2008) Surface-initiated atom transfer radical polymerization. A new method of preparation of polymeric membrane adsorber, *J. Membr. Sci. 309*, 64.

26. Phillips, M. W. Method for determining an effective Pectlect number for a membrane adsorber device, Millipore Corporation, Billerica, MA, US patent, 281, 410 B2(2007).

27. Klein, E., Yeager, D., Seshadri, R., and Baurmeister, U. (1997) Affinity adsorption devices prepared from microporous poly(amide) hollow fibers and sheet membranes, *J. Membr. Sci. 129*, 31.

28. Ghosh, R., and Wong, T. (2006) Effect of module design on the efficiency of membrane chromatographic separation processes, *J. Membr. Sci. 281*, 532.

29. Cabanne, C., Raedts, M., Zavadzky, E., and Santarelli, X. (2007) Evaluation of radial chromatography verus axial chromatography, practical approach, *J. Chromatogr. B 845*, 191.

30. Zhou, J., and Tressel, T. (2006) Basic concepts in Q membrane chromatography for large-scale antibody production, *Biotechnol. Prog. 22*, 341.

31. Suen, S. Y., and Etzel, M. R. (1992) A mathematical analysis of affinity membrane bioseparations, *Chem. Eng. Sci. 47*, 1355.

32. Sarfert, F. T., and Etzel, M. R. (1997) Mass transfer limitations in protein separations using ion-exchange membranes, *J. Chromatogr. A 764*, 3.

33. Gebauer, K. H., Thömmes, J., and Kula, M. R. (1997) Breakthrough performance of high-capacity membrane adsorbers in protein chromatography, *Chem. Eng. Sci. 52*, 405.

34. Roper, D. K., and Lightfoot, E. N. (1995) Estimation plate heights in stacked-membrane chromatography by flow reversal, *J. Chromatogr. A 702*, 69.

35. Thömmes, J., and Kula, M. R. (1995) Membrane chromatography - An interactive concept in the downstream processing of proteins, *Biotechnol. Prog. 11*, 357.

36. Van Reis, R., and Zydney, A. (2007) Bioprocess membrane technology, *J. Mem. Sci. 297*, 16.

37. Abhinav, A. S., Etzel, M. R., and Gadam, S., (Eds.) (2007) *Process scale and optimization for the biopharmaceutical industry*, Taylor&Francis Group.

38. Tatárová, I., Fáber, R., Denoyel, R., and Polakovic, M. (2009) Characterization of pore structure of a strong anion-exchange membrane adsorbent under different buffer and salt concentration conditions, *J. Chromatogr. A 1216*, 941.

39. Teeters, M. A., Conrardy, S. E., Thomas, B. L., Root, T. W., and Lightfoot, E. N. (2003) Adsorptive membrane chromatography for purification of plasmid DNA, *J. Chromatogr. A 989*.

40. Endres, H. N., Johnson, J. A., Ross, C. A., Welp, J. K., and Etzel, M. R. (2003) Evaluation of an anion-exchange membrane for purification of plasmid DNA, *Biotechnol. Appl. Biochem. 37*, 259.

41. Vicente, T., Sousa, M. F. Q., Peixoto, C., Mota, J. P. B., Alves, P. M., and Carrondo, M. J. T. (2008) Anion-exchange membrane chromatography for purification of rotavirus-like particles, *J. Membr. Sci. 311*, 270.

42. Kemp, G., and O'Neil, P. (2004) *Large-scale production of therapeutic antibodies: consideration for optimizing product capture and purification*, Vol. 1, Plenum publishers, New York.

43. Darling, A. (2002) Validation of biopharmaceutical purification processes for virus clearance evaluation, *Mol. Biotechnol. 21*, 57.

44. Petsch, D., and Anspach, F. B. (2000) Endotoxin removal from protein solutions, *J. Biotechnol. 76*, 97.

45. Ghosh, R. (2002) Protein separation using membrane chromatography: opportunities and challenges, *J. Chromatogr. A 952*, 13.

46. Yusof, A. H. M., and Ulbricht, M. (2008) Polypropylene-based membrane adsorbers via photo-iniated graft copolymerization: optimizing separation performance by preparation conditions, *J. Membr. Sci. 311*, 294.

47. Pätzold, F. (2005) Membranadsorber mit variierter Porenstruktur und Funktional-

schicht, Diplomarbeit, in *Technische Chemie*, Universität Duisburg-Essen.

48. Lightfoot, E. N., and Moscariello, J. S. (2004) Bioseparation, *Biotechnol. Bioeng. 87*, 259.

49. Nelson, D. L., and Cox, M. M., (Eds.) (2004) *Lehninger principles of biochemistry*, WH Freeman and Company, New York

50. Ghosh, R. (2006) Principles of bioseparations engineering, World Scientific Publishing Co. Pte. Ltd.

51. Janson, J.-C., and Ryden, L., (Eds.) (1998) *Protein purification-principles, high-resolution methods and application*, John Wiley&Sons, Inc.

52. Rathore, A. S., and Velayudhan, A., (Eds.) (2003) *Scale-up and optimization in preparative chromatography-principles and biopharmaceutical applications*, Marcel Dekker, Inc., New York, Basel.

53. Harrison, R. G., Todd, P., Rudge, S. R., and Petridge, D. P., (Eds.) (2003) *Bio-separation science and engineering*, Oxford University Press.

54. Dephillips, P., and Lenhoff, A. M. (2001) Determination of protein retention characteristics on cation-exchange adsorbents, *J. Chromatogr. A 933*, 57.

55. Hallgren, E., Kalman, F., Farnan, D., Horvath, C., and Stahlberg, J. (2000) Protein retention in ion-exchange chromatography: effect of net charge and charge distribution, *J. Chromatogr. A 877*, 13.

56. Peinemann, K. V., and Nunes, S. P., (Eds.) (2008) *Membranes for the life science*, Wiley-VCH Verlag GmbH&Co. KGaA.

57. Teeters, M. A. (2004) Adsorption and desorption behavior of plasmid DNA on ion-exchange membranes: Effect of salt valence and compaction agents, *J. Chromatogr. A 1036*, 73.

58. http://www.sartorius-stedim.com/index.php?id=7089.

59. http://www.pall.com/biopharm_4354.asp.

60. Vlakh, E. G., and Tennikova, T. B. (2007) Preparation of methacrylate monoliths, *J. Sep. Sci. 30*, 2801-2813.

61. Xie, S., Allinqton, R. W., Frechet, J. M., and Svec, F. (2002) Porous polymer monoliths: an alternative to classical beads, *Adv. Biochem. Eng. Biotechnol. 76*, 87.

62. Schmidt-Traub, H. (2005) *preparative chromatography for fine chemicals and pharmaceutical agents*, Wiley-VCH.

63. Ludemann-Hombourger, O., Nicoud, R. M., and Bailly, M. (2000) The 'VARICOL' process: A new multicolumn continuous chromatographic process, *Separ. Sci. Technol. 35*, 1829.

64. Suen, S. Y., and Etzel, M. R. (1994) Sorption kinetics and breakthrough curves for

pepsin and chymosin using pepstatin A affinity membranes, *J. Chromatogr. A 686*, 179.

65. Goedecke, R., (Ed.) (2006) *Fluidverfahrenstechnik*, Wiley-VCH Verlag GmbH&Co. kGaA, Weinheim.

66. Kubota, N., Nakagawa, Y., and Eguchi, Y. (1996) Recovery of serum proteins using cellulosic affinity membrane modified by immobilization of $Cu^{2+}$ ion, *J. Appl. Polym. Sci. 62*, 1153.

67. Lightfoot, E. N., Coffman, J. L., Lode, F., Yuan, Q. S., Perkins, T. W., and Root, T. W. (1997) Refing the description of protein chromatography, *J. Chromatogr. A 760*, 139.

68. Geismann, C., and Ulbricht, M. (2005) Photoreactive functionalization of poly(ethylene terephthalate) track-etched pore surfaces with ‘‘smart’’ polymer systems, *Macromol. Chem. Phys. 206*, 268.

69. Thom, V., Jankova, K., Ulbricht, M., Kops, J., and Jonsson, G. (1998) Synthesis of photoreactive a-4-azidobenzoyl-methoxy-poly(ethylene glycol)s and their end-on photo-grafting onto polysulfone ultrafiltration membranes, *Macromol. Chem. Phys. 199*, 2723.

70. Kato, K., Uchida, E., Kang, E. T., Uyama, Y., and Ikada, Y. (2003) Polymer surface with graft chains, *Progr. Poly. Sci. 28*, 209.

71. Yang, W. T., and Ranby, B. (1999) Photoinitiation performance of some ketones in the LDPE-acrylic acid surface photografting system, *Eur. Polym. J. 35*, 1557.

72. Brandt, S., Goffe, R. A., Kessler, S., O'Connor, J. L., and Zale, S. E. (1988) Membrane-based affinity technology for commercial scale purifications, *Biotechnology 6*, 779.

73. Beeskow, T. C., Kusharyoto, W., Anspach, F. B., Kroner, K. H., and Deckwer, W. D. (1995) Surface modification of microporous polyamide membranes with hydroxylethyl cellulose and their application as affinity membrane, *J. Chromatogr. A 715*, 49.

74. Koguma, I., Sugita, K., Sugita, K., Saito, K., and Sugo, T. (2000) Multilayer binding of proteins to polymer chains grafted onto porous hollow-fiber membranes containing different anion-exchange groups, *Biotechnol. Prog. 16*, 456.

75. Sunaga, K., Kim, M., Saito, K., and Sugita, K. (1999) Characterization of porous anion-exchange membranes prepared by cografting of glycidyl methacrylate with divinylbenzene, *Chem. Mater.*, 1986.

76. Ulbricht, M., and Riedel, M. (1998) Ultrafiltration membrane surfaces with grafted polymer ‘tentacles’: preparation, characterization and application for covalent protein binding, *Biomaterials 19*, 1229.

77. Ulbricht, M., Matuschewski, H., Oechel, A., and Hicke, H.-G. (1996) Photo-induced graft polymerization surface modifications for the preparation of hydrophilic and low protein adsorbing ultrafiltration membranes, *J. Membr. Sci. 115*, 31.

78. Ulbricht, M., Oechel, A., Lehmann, C., Tomaschewski, G., and Hans-Georg, H. (1995)

Gas-phase photoinduced graft polymerization of acrylic acid onto polyacrylonitrile ultrafiltration, *J. Appl. Polym. Sci. 55*, 1707.

79. He, D. M., and Ulbricht, M. (2006) Surface-selective ühoto-grafting on porous polymer membranes via a synergist immobilization method, *J. Mater. Chem. 16*, 1860.

80. He, D. M., and Ulbricht, M. (2007) Synergist immobilization method for photo-grafting: factors affecting surface selectivity, *Macromol. Chem. Phys. 208*, 1582.

81. Borcherding, H., Hicke, D., Jorcke, D., and Ulbricht, M. (2003) Affinity membranes as a tool for life applications, *Ann. N. Y. Acad. Sci. 984*, 470.

82. Kochkodan, V., Weigel, W., and Ulbricht, M. (2001) Thin layer molecularly imprinted microfiltration membranes by photofunctionalization using a coated α-cleavage photoinitiator, *Analyst 126*, 803.

83. Schneider, F., Piletsky, S., Piletska, E., Guerreiro, A., and Ulbricht, M. (2005) Comparison of thin-layer and bulk MIPs synthesized by photoinitiated in situ crosslinking polymerization from the same reaction mixtures, *J. Appl. Polym. Sci. 98*, 362.

84. Schirmer, E. B., and Carta, G. (2007) Protein adsorption in charged agarose gels studied by light microscopy, *AIChE Journal 53*, 1472.

85. Wang, J., Thom, V., Hollas, M., and Johannesmann, D. (2008) Dye deposition patterns obtained in line printing on macroporous membranes: Improvement of line sharpness by liquid redistribution, *J. Membr. Sci. 318*, 280.

86. Thiel, B. L., and Donald, A. M. (1999) The study of water in heterogeneous media using environmental scanning electron microscopy, *J. Mol. Liq. 80*, 207.

87. Jenkins, L. M., and Donald, A. M. (1997) Use of the environmental scanning electron microscope for the observation of the swelling behaviour of cellulose fibers, *Scanning 19*, 92.

88. Parra, R. E. d. l. (1993) A method to detect variations in the wetting properties of microporous polymer membranes, *Microsc. Res. Tech. 25*, 362.

89. Donald, A. M. (2003) The use of environmental scanning electron microscopy for imaging wet and insulating materials, *Nature Materials 2*, 511.

90. Pawley, J. (1995) *Handbook of biological confocal microscoy*, Pleum Press, New York.

91. Ljunglöf, A., and Thommes, J. (1998) Visualising intraparticle protein transport in porous adsorbents by confocal microscopy, *J. Chromatogr. A 813*, 387.

92. Ljunglöf, A., and Hjorth, R. (1996) Confocal microscopy as a tool for studing protein adsorption to chromatographic matrics, *J. Chromatogr. A 743*, 75.

93. Linden, T., Ljunglöf, A., Hagen, L., Kula, M., and Thommes, J. (2002) Visualizing patterns of protein uptake to porous media using confocal scanning laser microscopy, *Sep. Sci. Technol. 37*, 1.

94. Schroeder, M., Von Lieres, E., and Hubbuch, J. (2006) Direct quantification of intraparticle protein diffusion in chromatographic media, *J. Phys. Chem. B 110*, 1429.

95. Kasche, V., De Boer, M., Lazo, C., and Gad, M. (2003) Direct observation of intraparticle equilibration and the rate-limiting step in adsorption of proteins in chromatographic adsorbents with confocal laser scanning microscopy, *J. Chromatogr. B 790*, 115.

96. Hubbuch, J., Linden, T., Knieps, E., Ljunglöf, A., Thömmes, J., and Kula, M.-R. (2003) Mechanism and kinetics of protein transport in chromatographic media studied by confocal laser scanning microscopy: Part I. The interplay of sorbent structure and fluid phase conditions, *J. Chromatogr. A 1021*, 93.

97. Charcosset, C., Cherfi, A., and Bernengo, J. C. (2000) Characterization of micro-porous membrane morphology using confocal scanning laser microscopy, *J. Chem. Eng. Sci. 55*, 5351.

98. Reichert, U., Linden, T., Belfort, G., Kula, M.-R., and Thömmes, J. (2002) Visualising protein adsorption to ion-exchange membranes by confocal microscopy, *J. Membr. Sci. 199*, 161.

99. Wickramasinghe, S. R., Han, B., Carlson, J. O., Teske, C., Hubbuch, J., and Ulbricht, M. (2006) Characterizing solute binding to macroporous ion exchange membrane adsorbers using confocal laser scanning microscopy, *J. Membr. Sci. 281*, 609.

100. Wang, J., Dismer, F., Hubbuch, J., and Ulbricht, M. (2008) Detailed ananlysis of membrane adsorber pore strcture and protein binding by advanced microscopy, *J. Membr. Sci. 320*, 456.

101. Friebe, A., and Ulbricht, M. (2007) Controlled pore functionalization of poly(ethylene terephthalate) track-etched membranes via surface-initiated atom transfer radical polymerization, *Langmuir 23*, 10316.

102. Strange, J. H., Rahman, M., and Smith, E. G. (1993) Characterization of porous solids by NMR, *Physical Review Letters 71*, 3589.

103. Gane, P. A. C., Ridgway, C. J., Lehtinen, E., Valiullin, R., Furó, I., Schoelkopf, J., Paulapuro, H., and Daicic, J. (2004) Comparison of NMR cryoporometry, mercury intrusion porosimetry, and DSC thermoporosimetry in characterizing pore size distributions of compressed finely ground calcium carbonate structures, *Ind. Eng. Chem. Res. 43*, 7920.

104. Hagel, L., Östberg, M., and Andersson, T. (1996) Apparent pore size distributions of chromatography media, *J. Chromatogr. A 743*, 33.

105. DePhillips, P., and Lenhoff, A. M. (2000) Pore size distributions of cation-exchange adsorbents determined by inverse size-exclusion chromatography, *J. Chromatogr. A 883*, 39.

106. Ousalem, M., Zhu, X. X., and Hradil, J. (2000) Evaluation of the porous structures of new polymer packing materials by inverse size-exclusion chromatography, *J. Chromatogr. A 903*, 13.

107. Susanto, H., and Ulbricht, M. (2007) Photografted thin polymer hydrogel layers on PES ultrafiltration membranes: characterization, stability, and influence on separation performance, *Langmuir 23*, 7818.

108. (1996) Product manual of Coulter SA 3100 series surface area and pore size analysers.

109. Tugeu, N., Roush, D. J., and Göklen, K. E. (2008) Maximizing productivity of chromatography steps for purification of monoclonal antibodies, *Biotechnol. Bioeng. 99*, 599.

110. Staby, A., Jensen, R. H., Bensch, M., Hubbuch, J., Dünweber, D. L., Krarup, J., Nielsen, J., Lund, M., Kidal, S., Hansen, T. B., and Jensen, I. H. (2007) Comparison of chromatographic ion-exchange resins. VI. Weak anion-exchange resins, *J. Chromtogr. A 1164*, 82.

111. Gadam, S., Jayaraman, G., and Cramer, S. M. (1993) Charaterization of non-linear adsorption properties of dextran-based polyelectrolyte displacers in ion-exchange systems, *J. Chromatogr. 630*, 37.

112. Lendero, N., Vidic, J., Brne, P., and Podgornik, A. (2005) Simple method for determining the amount of ion-exchange groups on chromatographic supports, *J. Chromatogr. A 1065*.

113. Podgornik, A., J. Vidic, J. J., Lendero, N., Frankovic, V., and Strancar, A. (2005) Noninvasive methods for characterization of large-volume monolithic chromatographic columns, *Chem. Eng. Techn. 28*, 1435.

114. Venkatesh, N., and Cramer, S. (2000) A methodology for the characterization of ion-exchange resins, *Sep. Sci. Technol. 35*, 1719.

115. Yang, W., Bitzer, M., and Etzel, M. R. (1999) Analysis of protein purification using ion-exchange membranes, *Ind. Eng. Chem. Res. 38*, 4044.

116. Boi, C., Dimartino, S., and Sarti, G. C. (2007) Modelling and simulation of affinity membrane adsorption, *J. Chromatogr. A 1162*, 24.

117. Montesinos, R. M., Olivas, J. V., Ortega, J., Roberto, G., and Etejeda-Mansir, A. (2007) Breakthrough performance of plasmid DNA on ion-exchange memrbane columns, *Biotechnol. Prog. 23*, 881.

118. von Lieres, E., Wang, J., and Ulbricht, M. (2009 ) Model based quantification of internal flow distributions from breakthrough curves of coin-shaped membrane chromatography modules, *Ind. Eng. Chem. Res. submitted*.

119. von Lieres, E., Wang, J., Ulbricht, M., Francis, P., and Haynes, C. (2009) A zonal rate model for stacked membrane chromatography, *Desalination, submitted*.

120. Etzel, M. R., and Riordan, W. T. (2007) Membrane chromatography: Analysis of breakthrough curves and viral clearance, in *Process scale and optimization for the biopharmaceutical industry* (Abhinav, A. S., Etzel, M. R., and Gadam, S., Eds.), Taylor & Francis Group.

121. Yang, H., Viera, C., Fischer, J., and Etzel, M. R. (2002) Purification of a large protein

ion-exchange membranes, *Ind. Eng. Chem. Res. 41*, 1597.

122. Kochan, J. E., Wu, Y.-J., and Etzel, M. R. (1996) Purification of Bovine Immunoglobulin G via Protein G Affinity Membranes, *Ind. Eng. Chem. Res. 35*, 1150.

123. Boi, C. (2007) Membrane adsorbers as purification tools for monoclonal antibody purification, *J. Chromatogr. B 848*, 19.

124. Jungbauer, A. (1996) Insights into the chromatograpy of proteins provided by mathematical modeling, *Curr. Opin. in Biotechnol. 7*, 210.

125. Yang, H., and Etzel, M. R. (2003) Evaluation of three kinetic equations in models of protein purification using ion-exchange membranes, *Ind. Eng. Chem. Res. 42*, 890.

126. Wang, G., and Carbonell, R. G. (2005) Characterization of a peptide affinity support that binds selectively to staphylococcal enterotoxin B, *J. Chromatogr. A 1078*, 98.

127. Brooks, C. A., and Cramer, S. M. (1992) Steric mass-action ion exchange: displacement profiles and induced salt gradients, *AIChE Journal 38*, 1969.

128. Iyer, H., Tapper, S., Lester, P., Wolk, B., and van Reis, R. (1999) Use of steric mass action model in ion-exchange chromatographic develoment, *J. Chromatogr. A 832*, 1.

129. Frerick, C., Krei, P., Gorak, A., Tappe, A., and Melzner, D. (2008) Simulation of a human serum albumin downstream process in corporating ion-exchange membrane adsorbers, *Chem. Eng. Process: Process Intensification 47*, 1128.

130. Teske, C., Schroeder, M., Simon, R., and Hubbuch, J. (2005) Protein-labelling effects in confocal laser scanning microscopy *J. Phys. Chem. B 109*, 13811.

131. Cameron, R. E., and Donald, A. M. (1994) Minimizing sample evaporation in the environmental scanning electron microscope, *J. Micros. 173*, 227.

132. Dismer, F., and Hubbuch, J. (2007) A novel approach to characterize the binding orientation of lysozyme on ion-exchange resins, *J. Chromatogr. A 1149*, 312.

133. Mulder, M. (1996) *Basic principles of membrane technology*, Kluwer Academic Publisher, Dordrecht.

134. Nevell, T. P., and Zeronian, S. H. (1985) *Cellulose chemistry and its application*, Ellis Horwood Limited, West Sussex, England.

135. Kawai, T., Sugita, K., Saito, K., and Sugo, T. (2000) Extension and shrinkage of polymer brush grafted onto porous membrane induced by protein binding, *Macromolecules 33*, 1306.

136. Li, N., Liu, Z. Z., and Xu, S. G. (2001) A review of studies of the preparation processes of regenerated cellulose separation membranes, *Membrane Sci.&Technol. 21*, 27.

137. Pearsall, S. K., Green, M. M., and Morawetz, H. (2004) Titration of poly(carboxalic acid)s in methanol solution. Polymer chain extension, ionizaiton equilibria, and conformational mobility, *Macromolecules 37*, 8773.

138. Staby, A., Jensen, R. H., Bensch, M., Hubbuch, J., Dünweber, D. L., Krarup, J., Nielsen, J., Lund, M., Kidal, S., Hansen, T. B., and Jensen, I. H. (2007) Comparison of chromatographic ion-exchange resins. VI. Weak anion-exchange resins, *J. Chromto. A 1164*, 82.

139. Wang, J., Faber, R., and Ulbricht, M. (2009) Influence of pore structure and architecture of photo-grafted functional layers on separation performance of cellulose-based macroporous membrane adsorbers, *J. Chromatogr. A, under reversion*.

140. Kuehner, D. E., Engmann, J., Fergg, F., Wernick, M., Blanch, H. W., and Prausnitz, J. M. (1999) Lysozyme net charge and ion binding in concentrated aqueous electrolyte solutions, *J. Phys. Chem. B 103*, 1368.

141. http://www.azom.com/Details.asp?ArticleID=1556.

142. Osborn, J. (2002) A review of the suitability of CyDye fluors for use in high throughput drug screening applications, http://www4.gelifesciences.com/APTRIX/upp01077.nsf/Content/lsn_online_article_300602_j?OpenDocument&hometitle=lsn_online.

143. Susanto, A., Herrmann, T., and Hubbuch, J. (2006) Short-cut method of the correction of light attenuation influences in the experimental data obtained from confocal laser scanning microscopy, *J. Chromatogr. A 1136*, 29.

144. Tallarek, U., Rapp, E., Sann, H., Reichl, U., and Seidel-Morgenstern, A. (2003) Quantitative study of electrokinetic transport in porous media by Cofocal Laser Scanning Microscopy, *Langmuir 19*, 4527.

145. Čapek, M., Janăček, J., and KubÍnovă, L. (2006) Methods for compensation of the light attenuation with depth images captured by a confocal microscope, *Microsc. Res. Tech. 69*, 624.

146. Linden, T. (2001) Untersuchungen zum inneren Transport bei der Proteinadsorption an poröse Medien mittels konfokaler Laser-Raster-Mikroskopie: Adsorption von BSA und IgG an der porösen Kationaustaucher SP-Sepharose FF, Dissertation, in *Heinrich-Heine-Univeristät Düsseldorf*, Düsseldorf.

147. Malmsten, M., Xing, K., and Ljunglöf, A. (1999) Transport of poly-l-lysine into oppositely charged poly(acrylic acid) microgels and its effect on gel deswelling, *J. Colloid Interface Sci.*, 436.

148. Dziennik, S., Belcher, E., Barker, G., and Lenhoff, A. (2005) Effects of inonic strength on lysozyme uptake rates in cation exchangers. I: Uptake in SP sepharose FF., *Biotechnol. Bioeng. 91*, 139.

149. Heinemann, M., Wagner, T., Doumeche, B., Ansorge-Schumacher, M., and Büchs, J. (2002) A new approach for the spatially resolved qualitative analysis of the protein distribution in hydrogel beads based on confocal laser scanning microscopy, *Biotechol. Lett. 24*, 845.

150. Ulbricht, M., Schuster, O., Ansorge, W., Ruetering, M., and Steiger, P. (2007) Influence of strongly anisotropic cross-section morphology of a novel polyethersulfone microfiltration membranes onto filtration performance, *Separ. Purif.*

*Techn. 57*, 63.

151. Manning, G. S. (1969) Limiting laws and counterion condensation in polyelectrolyte solutions I. colligation properties, *J. Chem. Phys. 51*, 924.

152. Khokhlov, A. R., and Kramarenko, E. Y. (1996) Weakly charged polyelectrolytes: collapse induced by extra ionization, *Macromolecules 29*, 681.

153. Kontturi, K., Mafe, S., Manzanares, J. A., Svarfvar, B. L., and Viinikka, P. (1996) Modeling of the salt and pH effects on the permeability of grafted porous membranes, *Macromolecules 29*, 5740.

154. Haber, C., Skupsky, J., Lee, A., and Lander, R. (2004) Membrane chromatography of DNA: conformation-induced capacity and selectivity *Biotech. Bioeng. 88*, 26.

155. Tugeu, N., Roush, D. J., and Göklen, K. F. (2000) Maximizing productivity of chromatography steps for purification of monoclonal antibodies, *Biotech. Bioeng. 99*, 599.

156. Harinarayan, C., Mueller, J., LJunglöf, A., Fahrner, R., and Reis, R. v. (2006) An exclusion mechanism in ion exchange chromatography, *Biotech. Bioeng. 95*, 775.

157. Ventura, A. M., Lahore, H. M. F., Smolko, E. E., and Grasselli, M. (2008) High-speed protein purification by adsorptive cation-exchange hollow-fiber cartridges, *J.Membr. Sci. 321*, 350.

158. Guo, W., and Ruckenstein, E. (2003) Modified glass fiber membrane and its application to membrane affinity chromatography *J. Membr. Sci. 215*, 141.

159. Kubota, N., Konno, Y., Saito, K., Sugita, K., Watanabe, K., and Sugo, T. (1997) Module performance of anion-exchange porous hollow-fiber membranes for high-speed protein recovery, *J. Chromatogr. A 782*, 159.

160. Castillho, L. R., Deckwer, W. D., and Anspach, F. B. (2000) Influence of matrix activation and polymer coating on the purification of human IgG with protein A affinity membranes, *J. Membr. Sci. 172*, 269.

161. Kumar, V., Bhardwaj, Y. K., Jamdar, S. N., Goel, N. K., and Sabharwal, S. (2006) Preparation of an anion-exchange adsorbent by the radiation-induced grafting of vinylbenzyltrimethylammonium chloride onto cotton cellulose and its application for protein adsorption, *J. Appl. Polym. Sci. 102*.

162. Tejeda, A., Ortega, J., Magana, I., and Guzman, R. (1999) Optimal design of affinity membrnae chromatographic columns, *J. Chromatogr. A 830*, 293.

163. Etzel, M. R. (2003) Monolithics materials: layered stacks, (Svec, F., Tennikova, T. B., and Deyl, Z., Eds.), Journal of Chromatography Library.

164. Rånby, B., Gao, Z. M., Hult, A., and Zhang, P. Y. (1986) Modification of polymer surfaces by graft copolymerization, *Polymer Preprints 27*, 38.

165. Yu, S.-H. (2008) Optimierung der Herstellung von Membranadsorbern durch photo-initiierte heterogene Pfropfcopolymerisation, Diplomarbeit, in *Technische Chemie*,

Universität Duisburg-Essen.

## B. List of abbreviations

| abbreviation | name |
|---|---|
| AA | Acrylic acid |
| AAm | Acrylamide |
| BP | Benzophenone |
| DBC | Dynamic binding capacity |
| DEA | Diethylamino |
| crAA | Poly(AA-co-MBAA) |
| crAAAm | Poly(AA-co-AAm-co-MBAA) |
| DEAE | Diethylaminoethyl |
| DEGMA | Diethyleneglycol dimethacrylate |
| EA | Ethanolamino |
| EVAL | Copolymer of ethylene and vinyl |
| GMA | Glycidyl methacrylate |
| IgG | γ-globulin from bovine blood |
| Lys | Lysozyme |
| 10% DBC | 10% dynamic binding capacity |
| max. DBC | Maximum dynamic binding capacity |
| MBAA | Methylene bisacrylamide |
| METMAC | Poly(2-(methacryloyloxy)ethyl)-trimethylammonium chloride) |
| PET | Polyethylenterephthalat |
| PHEMA | Poly(2-hydroxylethyl methacrylate) |
| PVBT | Poly(vinylbenzyltrimethylammonium chloride) |
| PAA | Poly(AA) |
| SCell module | Sartorius cell |

## C. List of publications and conferences

### Publications

1. von Lieres, E., Wang, J., Ulbricht, M. *Model based quantification of internal flow distributions from breakthrough curves of coin-shaped membrane chromatography modules*, Ind. Eng. Chem. Res., 2009, submitted.

2. Wang, J., Faber, R., Ulbricht, M. *Influence of pore structure and architecture of photo-grafted functional layers on separation performance of cellulose-based macroporous membrane adsorbers*, J. Chromatogr. A, 2009, under reversion.

3. Wang, J., Dismer, F., Hubbuch, J., Ulbricht, M. *Detailed analysis of membrane adsorber pore structure and protein binding by advanced microscopy*, J. Membr. Sci., 320 (2008) 456-467.

4. von Lieres, E., Wang, J., Ulbricht, M., Francis, P., and Haynes, C., *A zonal rate model for stacked membrane chromatography*, Desalination 2009, submitted.

5. Singh, N., Wang, J., Ulbricht, M., Wickramasinghe, S. R., Husson, S. M. *Surface-initiated atom transfer radical polymerization. A new method of preparation of polymeric membrane adsorber*, J.Membr. Sci., 309 (2008) 64-72.

6. Wang, J., Thom, V., Hollas, M., Johannesmann, D. *Dye deposition patterns obtained in line printing on macroporous membranes: Improvement of line sharpness by liquid redistribution*, J. Membr. Sci., 318 (2008) 280-287.

7. Wang, J., Johannesmann, D., Hollas, M., Thom, V. *Visualization of capture line protein binding in nitrocellulose diagnostic membranes,* Desalination, 199 (2006) 232-233.

## Conference proceedings

1. Wang, J., von Lieres, E., Faber, R., Ulbricht, M. *Investigation and model based quantification of the influence of membrane modules on protein separation performance with porous membrane adsorbers*, Permea 2009, Prague, Czech Republic, June 07-11, 2009, special lecture.

2. Wang, J., Dismer, F., Hubbuch, J., Ulbricht, M. *Influence of membrane structure and process conditions on separation performance of macroporous membrane adsorbers,* Engineering with membranes 2008, Portugal, May 25-28, 2008, special lecture.

3. Wang, J., Dismer, F., Hubbuch, J., Ulbricht, M. *Macroporous membrane adsorebrs – correlations between structure and separations performance*, 4. Doktrandenseminar - Präparative Chromatographie, Hamburg, September 12-18, 2007, oral presentation.

4. Wang, J., Dismer, F., Hubbuch, J., Ulbricht, M. *Macroporous membrane adsorbers-correlations between structure and separations performance*, Permea 2007, Siófok, Hungary, September 02-06, 2007, oral presentation.

5. Wang, J., Dismer, F., Hubbuch, J., Ulbricht, M. *Visualization of morphology of macroporous membrane adsorbers and protein binding by means of confocal laser scanning microscopy*, 11$^{th}$ Aachener Membrane Kolloquium, Germany, March 28-29, 2007, poster.

## D. Curriculum Vitae

### Personal Data

| | |
|---|---|
| Name | Wang, Jun |
| Date of birth | 01.August 1968 |
| Nationality | P. R. China |
| Personal Standing | Married |

### Educations

| | |
|---|---|
| Since 05/2006 | Doctoral work at the Lehrstuhl für Technische Chemie II, Universität Duisburg-Essen, Germany<br>Supervisor: Prof. Mathias Ulbricht |
| 10/2000 – 01/2006 | Study at the Technische Universität Clausthal, Clausthal-Zellerfeld, Germany<br>Major: Chemical engineering<br>Graduate degree: Dipl.-Ing. |
| 10/1986 – 07/1989 | Study at the East China University of Science and Technology,<br>Shanghai, China<br>Major: Fine chemical engineering |

### Work Experiences

| | |
|---|---|
| Since 02/2006 | Employed as Scientific assistant at the Lehrstuhl für Technische Chemie II, Universität Duisburg-Essen, Germany |
| 05/2005 – 01/2006 | Internship and Diplomarbeit at the Sartorius Stedim Biotech GmbH,<br>R & D - Membrane Division, Göttingen, Germany |
| 09/1989 – 09/1999 | Employed at the Yasing Chemical Group, China<br>Development & Strategy Department, Engineering Office, for chemical project engineering |